POLYAMORPHISM IN SEMICONDUCTORS

A dissertation presented to

the faculty of

the College of Arts and Sciences of Ohio University

In partial fulfillment

of the requirements for the degree

Doctor of Philosophy

Murat Durandurdu

November 2002

© 2002
Murat Durandurdu
All Rights Reserved

This dissertation entitled

POLYAMORPHISM IN SEMICONDUCTORS

BY

MURAT DURANDURDU

has been approved for

the Department of Physics and Astronomy

and the College of Arts and Sciences by

David A. Drabold

Professor of Physics

Leslie A. Flemming

Dean, College of Arts and Sciences

Durandurdu, Murat Ph.D. November 2002. Physics.

Polyamorphism in Semiconductors. (218 pp.)

Director of Dissertation: David A. Drabold

A pressure-induced polyamorphic phase transition was reported in some amorphous semiconductors about thirty years ago. Investigation of this transition is hindered by difficulties of probing thin films, and hence it is little explored and understood, especially on the basis of theory work. In this dissertation, we perform constant volume and pressure simulations to reveal pressure-induced phase transitions in certain amorphous semiconductors. We find that amorphous Si and Ge exhibit a first order amorphous to amorphous phase transition while amorphous $GeSe_2$ undergoes a gradual phase change from a low-density amorphous phase to a high density amorphous phase. The transition in amorphous Si, Ge and $GeSe_2$ agrees with the available experiments. A crystalline grain in paracrystalline Si transforms from diamond phase to a high density amorphous phase with the application of pressure, which is consistent with the experimental investigation of porous silicon. Gibbs free energy calculations predict a pressure-induced amorphization of crystalline Si, in agreement with pressure-temperature phase diagram, and a pressure-induced high-density crystallization of amorphous and paracrystalline Si. We argue that the crystallization of these amorphous semiconductors is kinetically hindered at low-temperatures in the simulations.

In this work, we give the detailed analysis of the structural modification of these amorphous networks, and the pressure-induced changes in electronic and vibrational properties. We find several common features. The high density amorphous phase of amorphous Si, Ge, and paracrystalline Si resembles the metallic topology found in their liquid phase. The optical gap of amorphous Si, Ge and paracrystalline silicon increases, reaches a maximum and then decreases with the application of pressure while that of their crystalline form decreases smoothly. On the other hand, the gap of amorphous $GeSe_2$ closes gradually under pressure. The localized electronic and vibrational states become extended with increasing pressure. Softening of low-frequency modes is observed in amorphous Si and Ge but those of $GeSe_2$ shift to higher frequencies. Metallization is sharp in elemental amorphous semiconductors whereas it is gradual in binary amorphous compounds, which are consistent with experiments. We propose that this continuous phase change is due to chemical disorder which allows different bonding with distinct physical properties and metastable limits in the binary amorphous compounds.

We also study crystal to crystal phase transition in Si and Ge and calculate some physical properties of their high pressure phase. Finally we clear the some doubts about the identify of the high pressure phases of GaAs and explain transition paths between the phases.

Approved: David A. Drabold

Professor of Physics

Acknowledgments

I would like to thank Professor David A. Drabold, my advisor, for his guidance, constructive comments patience, and friendship. It is pleasure to work under his supervision and I am truly indebted to him.

I am grateful to my wife and my parents for their support, encouragement and patience.

Dr. Normand Mousseau and Dr. Jianjun Dong were of great contribution for this work. Their help, comments, and kindness were greatly appreciated.

I would like to thank the faculty, staff, and students in the Physics Department at Ohio University for their support, kindness, and contribution for this work.

I also wish to thank the Turkish Ministry of Education and the Turkish Physics Foundation for their partial support during my academic career.

This work is supported by the National Science Foundation.

Contents

Abstract 4

Acknowledgments 6

List of Tables 13

List of Figures 16

1 Background 23

1.1 Introduction 23

1.2 Pressure 26

1.3 The diamond-anvil cell 27

1.4 Phase transitions 29

1.5 Pressure response for crystalline semiconductors 31

1.6 Phase transitions in disordered materials 32

1.6.1 Pressure-induced crystallization 33

1.6.2 Polyamorphism 34

1.6.3 Anderson transition 36

1.7 Pressure-induced amorphization 37

1.8 Difficulties in study of amorphous materials 39
1.9 Total energy calculations 41
1.10 Thermodynamics 42
1.11 Equation of state 42
1.12 Objectives 43

2 Theoretical Foundation 45

2.1 Density Functional Theory 45
2.1.1 Hohenberg-Kohn theory 46
2.1.2 The Kohn-Sham Ansatz 48
2.1.3 The Local Density Approximation 49
2.2 Method 50
2.3 Classical Molecular Dynamics 51
2.4 Ab Initio Molecular Dynamics 53
2.5 Pressure Control 55
2.5.1 Andersen Method 56
2.5.2 Parrinello and Rahman Method 56
2.6 Modeling Amorphous Structures 59
2.6.1 Continuous Random Network 60
2.6.2 Wooten Winer and Weaire Method for tetrahedral amorphous materials 60
2.6.3 Quenching From Melt 62
2.6.4 Activation Relaxation Technique 63

3 *Ab initio* calculation of electronic structure of amorphous silicon 64

3.1 Introduction 64

3.2 Theoretical Consideration 66

3.3 Results and Discussions 68

3.4 Conclusions 75

4 First order amorphous to amorphous phase transition of silicon 77

4.1 Introduction 77

4.2 Computational technique 79

4.3 Results and Discussions 82

4.3.1 Structural Properties of c-Si Under Pressure 82

4.3.2 Structural properties of a-Si under pressure 82

4.3.3 The Pressure Dependence of Band Gap Energy 92

4.3.4 Localized states in a-Si and response to pressure 94

4.3.5 Vibrational density of states 94

4.4 Conclusions 96

5 A theoretical investigation of amorphization and crystallization in silicon phases 98

5.1 Introduction 98

5.2 Methodology 100

5.3 Results and Discussion 101

5.4 Conclusions 107

6 *Ab initio* simulation of pressure-induced low-energy excitations in

amorphous silicon **108**

6.1 Introduction 108

6.2 Methodology 110

6.3 Results and Discussion 111

6.3.1 Vibrational density of states 111

6.3.2 Imaginary frequencies 112

6.3.3 Phase quotient 114

6.3.4 Stretching character 115

6.3.5 Localized states and response to pressure 117

6.4 Conclusions 122

7 Pressure-induced structural phase transition of paracrystalline silicon **123**

7.1 Introduction 123

7.2 Methodology 126

7.3 Results and Discussions 127

7.3.1 Structural properties 127

7.3.2 Gibbs free energy calculation 134

7.3.3 Electronic structure 137

7.4 Conclusions 138

8 First-order pressure-induced polyamorphism in germanium **142**

8.1 Introduction 142

8.2 Methodology 144

8.3 Result and Discussion 145

9 Simulation of pressure-induced polyamorphism in a chalcogenide glass $GeSe_2$ 155

9.1 Introduction 155

9.2 Methodology 157

9.3 Structural Properties Under Pressure 159

9.3.1 Pressure Dependence of Volume 159

9.3.2 Structural Correlation 161

9.3.3 Topology and Bonding Under Pressure 166

9.3.4 Discussion 170

9.4 Electronic Structure 172

9.5 Vibrational Density of States 174

9.6 Conclusions 180

10 *Ab initio* simulation of high-pressure phases of GaAs 181

10.1 Introduction 181

10.2 Methodology 183

10.3 Results and Discussion 184

10.3.1 Parrinello-Rahman simulation 184

10.3.2 Phase transitions from Gibbs free energy 191

10.4 Conclusions 193

11 Concluding Remarks and Further Considerations 196

11.1 Summary 196

11.2 Further Considerations 199

Bibliography **201**

Appendix: Publication list **217**

List of Tables

3.1 Total energy per atom, their energy difference with *c*-Si, and the density of the models. 68

3.2 The optical gap of the models. 69

3.3 The measure of localization(four chosen valence states from a localized state (ls), to less extended states (lexs) and, to an extended state (exs) of the models. 75

4.1 Structural properties of *c*-Si under pressure: average bond length (ABL), average bond angle (ABA), bond angle distribution (BAD), and average coordination number (ACN). 84

4.2 Structural properties of *a*-Si under pressure. Same nomenclature as Table 4.1 90

4.3 Structural properties of the obtained zero-pressure phases on decompression. Same nomenclature as Table 4.1 91

5.1 The minimum energies E_{min}, the relative energy difference $\Delta E(= E^i - E^{diamond})$, the corresponding minimum volume per atom V_{min} and its ratio $V^r_{min} = V^i_{min}/V^{diamond}_{min}$, where i is diamond, β-Sn, a-Si and HDA phase. 102

7.1 Structural properties of *para*-Si under pressure: average bond length (ABL), average bond angle (ABA), width bond angle distribution (WBAD), and average coordination number (ACN). 132

7.2 The minimum energies E_{min}, the relative energy difference $\Delta E(= E^i - E^{diamond})$, the corresponding minimum volume per atom V_{min} and its ratio $V^r_{min} = V^i_{min}/V^{diamond}_{min}$, where i is diamond, β-Sn, and *para*-Si phase. 134

8.1 Structural properties of a-Ge on compression: average bond length (ABL), average bond angle (ABA), width of bond angle distribution (WBAD), and average coordination number (ACN). 149

8.2 Structural properties of a-Ge on decompression. Same nomenclature as Table 8.1. 150

9.1 Structural properties of a-$GeSe_2$ under pressure: average nearest neighbor distance (ANND), average bond angle (ABA), and average coordination number (ACN) which is calculated from the first minimum of the PDF (R_c=2.70-2.80 $\AA$). 168

10.1 Structural properties of GaAs under pressure; average bond length (ABL), average bond angle (ABA), width of bond angle distribution (WBAD), and average coordination number (ACN). 187

10.2 Structural parameters at zero temperature for ZB. Equilibrium volume per molecule $V_\circ$, bulk modules K, and pressure derivative of bulk modules K'. 192

List of Figures

1.1 Schematic representation of phase transition. 25

1.2 Phase transitions in crystalline and amorphous materials. Right and left arrow indicates compression and decompression, respectively. . . . 28

3.1 (a)Total electronic density of states (EDOS). (b) Electronic density of state in the band gap region.(c) (d) The exponential fit of K2 and mSW2 model respectively. 70

3.2 Electronic eigenstates in the band gap region. The position of vertical bars represents the eigenvalues of the electronic eigenstates and height of the bars is the spatial localization. 72

3.3 Spatial character of the local-to-extended transition in mSW1. For a given eigenstates, the electron charge density depicted according to the four level gray scale. See Ref. 94 for detailed information about the figure. 74

4.1 (a) The normalized volume of a-Si to the zero-pressure measured volume. At 16.25 GPa, the volume drops suddenly, indicating pressure-induced phase transition. (b) Gibbs free energy of amorphous and high pressure phase cross near 9GPa implying a transition. 83

4.2 (a) a-Si model at zero-pressure (b) The disordered high pressure phase at 16.25 GPa. 86

4.3 The pressure dependence of the total energy per atom for a-Si and the high pressure phase. 87

4.4 (a) The behavior of the pair distribution function (PDF) of and (b) The bond angle distribution function (BADF) of a-Si on compression and slow decompression. 89

4.5 Pressure dependence of the normalized optical gap to zero-pressure optical gap for c-Si (dashed line with triangle) for a-Si (dotted line with circle) and the normalized average Inverse Participation Ratio (solid line with star). 93

4.6 Electronic eigenstates in the band gap region. The position of vertical bars represents the eigenvalues of the electronic eigenstates and height of the bars is the spatial localization ($Q_2(E)$). The Fermi level lies in the middle of the band gap. Note the abrupt delocalization of tail states at 16.25 GPa. 95

4.7 Vibrational DOS of a-Si at 16 GPa and the high pressure phase at 16.25 GPa and c-Si at 10 GPa and 17 GPa. 97

5.1 The calculated Gibbs free energy for diamond, β-Sn, a-Si and the HDA phase. 103

5.2 The pressure dependence of the volume per atom. 105

6.1 The behavior of the VDOS under pressure. 113

6.2 The phase quotient. The PQ is close to +1 for acoustic-like modes and it is around -1 for optic-like modes. 116

6.3 Stretching character of the vibrational modes. 118

6.4 The inverse participation ratio of the a-Si modes under pressure. Note that the low-energy states are completely extended and the high-energy modes are localized at zero pressure. 120

6.5 The black, gray, and white atoms correspond to $\geq$ 10%,$\geq$ 5% and $\leq$ 5% of the total excitation, respectively. (a) $\omega = 37.63$ cm^{-1} at 8 GPa. (b) $\omega = 31.47$ cm^{-1} at 12 GPa, (c) $i\omega = -23.0$ cm^{-1} at 14 GPa, (d) $\omega = 26.57$ cm^{-1} at 14 GPa, (e) $i\omega = -49.26$ cm^{-1} at 15 GPa, and (f) $i\omega = -32.22$ cm^{-1} at 15 GPa. These modes with high IPR's at the low-energy regime are extended since the excitation is rather uniformly distributed. 121

7.1 The normalized volume of *para*-Si and a-Si as a function of pressure. 128

7.2 Nucleation centers define in the model at (a) 15 GPa, (b) 15.5 GPa and (c) 16 GPa (an intermediate step). 130

7.3 The real space pair distribution function g(r) of *para*-Si under pressure. g(r) of a-Si is also given at the transition pressure (16.25 GPa). 131

7.4 The bond angle distribution function (BADF) of *para*-Si and *a*-Si at transition pressure. 133

7.5 Gibbs free energy curve of *c*-Si, β-Sn and *para*-Si. 135

7.6 Pressure dependence of the normalized optical gap for *para*-Si, *c*-Si and *a*-Si. 139

7.7 The localized states near the band gap. 140

8.1 (a) The pressure dependence of the normalized volume of *a*-Ge. (b) The Gibbs free energy of the amorphous and the HDA phase. 147

8.2 (a) The real space pair distribution function. (b) The bond angle distribution function on compression and decompression. 148

8.3 The pressure dependence of the optical gap. **Inset:** Electronic eigenstates in the band gap region. The position of the vertical bars represent the eigenvalues of the electronic eigenstates, and the height of the bars is the spatial localization ($Q_2(E)$). The Fermi level lies in the middle of the band gap. Note the abrupt delocalization of the tail states at 12.75 GPa. 152

8.4 Vibrational DOS at 0, 12.5 and 12.75 GPa. 154

9.1 The normalized volume of *a*-$GeSe_2$ changes smoothly with up to 12 GPa. After this pressure and several others, it shows slope changes. Upon pressure release from 75 GPa, the path is reversed up to 30 GPa, and thereafter hysteresis is seen. 160

9.2 The behavior of the total structure factor $S(Q)$ and Fiber-Ziman structure factors. The FSDP is suppressed and its position shifts toward higher Q with increasing pressure. A new peak emerges at about 2 Å^{-1} which is mostly due to Ge-Ge correlation. 163

9.3 The total and partial real space pair distribution functions of a-$GeSe_2$. 164

9.4 Atomic configuration at 65 GPa. Ge (top) and Se (bottom) atoms are shown separately. Note the chain-like cluster of Se atoms. 165

9.5 (a) The bond angle distribution function (BADF). (b) The information entropy of the bond angle distribution function. 167

9.6 Pressure dependence of structural properties of a-$GeSe_2$: (a) the average coordination (AC), the average coordination of Ge (AC-Ge), the average coordination of Se (AC-Se), the average coordination of Ge with wrong bond(s) (AC-Ge with WB), and the average coordination of Se with wrong bond(s) (AC-Se with WB). (b) The average bond length (ABL), the average Ge-Se separation (A-Ge-Se),the average Ge-Ge distance (A-Ge-Ge), and the average Se-Se separation (A-Se-Se). (c) The percentage of the total wrong bond (P-WB), the percentage of Ge atoms with wrong bond(s) (P-Ge with WB), and the percentage of Se atoms with wrong bond (P-Se with WB). 169

9.7 Pressure dependence of the optical gap. 173

9.8 Electronic eigenstates of a-$GeSe_2$ at several pressure. The position of the vertical bar represents the eigenvalues of the electronic eigenstates, and the height of the bars is the spatial localization ($Q_2(E)$). Note the gradual delocalization of the states. 175

9.9 Vibrational density of states on compression and decompression from 16 GPa. 177

9.10 Vibrational inverse participation patio (IPR) of a-$GeSe_2$ under pressure. The highly localized modes at zero-pressure are extended with application of pressure. 179

10.1 (a) The normalized volume to the zero-pressure measured volume.(b) The energy E in eV per molecule versus the volume per molecule for ZB and the *Cmcm* and *Imm2* phase.(c) The Gibbs free energy of ZB and *Cmcm* and *Imm2* structures. 186

10.2 The bond angle distribution function (BADF) is calculated using a Gaussian representation and the width of broadening is $\sim 2°$. 189

10.3 The upper-left panel is ZB at 0 GPa, the upper-right panel is distorted structure at 39 GPa, the middle-left panel is *Cmcm* structure at 54 GPa and the middle-right panel is *Imm2* at 57 GPa. In the upper and middle panels, the dark atoms are Ga and white ones are As. The lower-left panel is *Cmcm* and the right one is *Imm2* and in these panels Ga and As is not identified. The lower-panels are correspond to the simple picture of transition path. 190

10.4 Electronic density of states (EDOS) of *Cmcm* at 54 GPa, and *Imm2* at 57 GPa. 194

10.5 VDOS of ZB structure at zero-pressure, *Cmcm* at 54 GPa, and *Imm2* at 57 GPa. 195

Chapter 1

Background

1.1 Introduction

Some disordered (amorphous, glassy) materials have useful semiconducting properties and are employed in a wide range of applications. For example, hydrogenated amorphous silicon(a-Si:H) is of great technological importance for solar cell and display applications, especially lightweight flexible substrates and large area devices. Virtually all computer laptop displays are controlled by a-Si:H thin film transistors.

Experimental and theoretical studies have successfully explained some properties of disordered materials. Yet there is a fascinating range of phenomena still poorly understood in these systems. The investigations of high pressure phases have reported that the materials, especially glasses, have shown a unique response to pressure. One of the most remarkable phenomena occurs in H_2O; it undergoes a first order phase transition from a low density amorphous (LDA) phase to a high density amorphous (HDA) phase with the application of pressure at 77 K [1, 2]. This unusual phase change in H_2O is named "polyamorphic" phase transition and provides evidence that there exists a *second* critical point of H_2O in its meta-stable supercooled region

beside to the normal-liquid vapor critical point [3, 4].

Numerous experimental and theoretical studies have been performed to investigate pressure-induced phase transitions in other disordered substances such as glassy SiO_2 and GeO_2, partly because of structural similarities between these glasses and H_2O. However, the investigations [5, 6] have shown that the amorphous to amorphous transition proceeds gradually in these materials. Recently a first order amorphous to amorphous phase transition similar to H_2O was discovered in SiO_2 near the glass transition temperature [7, 8].

It is sometimes stated that the concept of pressure-induced polyamorphism began with the discovery of the first amorphous to amorphous phase transition in H_2O in 1985. However, about thirty years ago, Shimomura *et al.*[9] reported that amorphous silicon (a-Si) and amorphous germanium (a-Ge) transformed to a metallic amorphous phase with a sharp drop in resistivity and the optical gap at room temperature. They argued that the transitions emerged from structural modification and were first order. They also proposed that the metallic behavior could be due to a more highly coordinated structure with a consequent destruction of localization. However a clear picture of the transitions could not be provided because the experimental data could not give detailed information about the pressure-dependence of the volume and the nature of the structural modification. Later, Minomura [10] reported the reconstruction of a disordered β-Sn structure in a-Si and a-Ge. Indeed before the discovery of polyamorphism in H_2O, amorphous to amorphous phase transitions were observed in tetrahedrally bonded semiconductors but have not got enough attention in condensed matter community. Recently pressure-induced amorphization

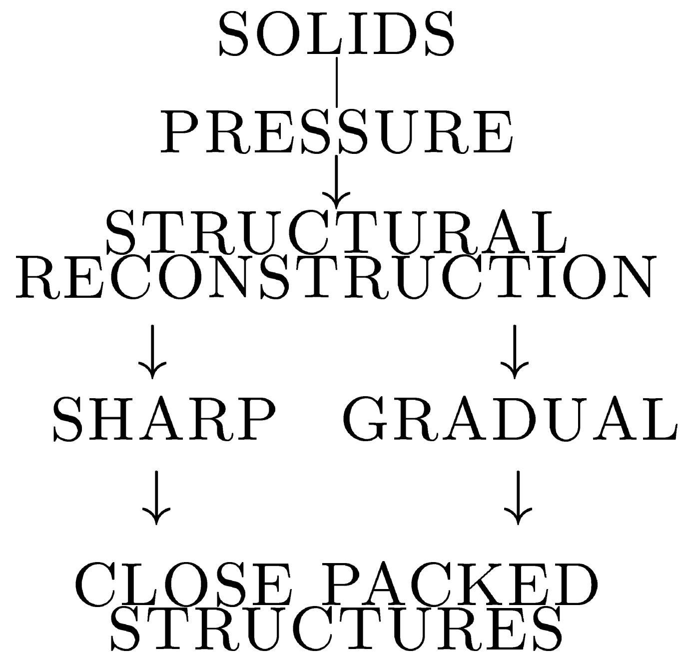

Figure 1.1: Schematic representation of phase transition.

and amorphous to amorphous phase transition have been reported in densified porous silicon [11], and it is argued that this amorphous to amorphous transition is similar to that found in H_2O.

Indeed experimental and theoretical studies of high pressure phases of disordered materials bring out more questions than answers. Nevertheless all these studies encourage the search for the possibility of polyamorphism in other disordered materials and clarification of fundamental aspect of the transition.

1.2 Pressure

In addition to temperature, pressure is a common thermodynamic variable which plays an important role in probing condensed matter. However, these variables affect materials in different ways. Temperature changes the kinetic energy and hence entropy of the vibrating atoms. Pressure yields a reduction of interatomic distances which gives rise to change in various properties including to the entropy. The most dramatic change may be pressure-induced phase transitions. Pressure yields both gradual and sharp first order phase transitions to more close packed structures (Figure 1.1), and hence it serves as a powerful probe for synthesizing dense phases, which is important in a geophysics. The pressure at the center of Earth is more than 300 GPa and the largest planets, Saturn and Jupiter are estimated to have core pressure of ~2-10 TPa.

The observed transitions in crystalline and amorphous structures are summarized in Figure 1.2. Upon compression, an open crystalline structure can transform to a high density crystalline structure (polymorphism) or an amorphous phase (pressure-induced amorphization). On the pressure release, the high density crystalline phase can transform back to the original crystalline structure (reversible transformation) or another crystalline structure (irreversible transformation). It is also possible that the high density crystalline phase can transform into an amorphous phase on decompression (pressure-induced amorphization). Under pressure an amorphous structure can undergo a transformation to a crystalline phase(pressure-induced crystallization) but this transition strongly dependence on temperature, sample properties, and loading

condition. When the crystallization of the amorphous network is kinetically hindered, an amorphous to amorphous phase transition (polyamorphism) is observed.

1.3 The diamond-anvil cell

The diamond anvil cell is the most useful experimental tool in high-pressure research. The diamond anvil cell holds the sample inside a pressure medium and between two diamonds. Some fluid such as argon and helium are used as a pressure transmitting medium. The two diamonds are brought together to apply force to the medium, and hence indirectly on the sample. Pressure is defined as the force applied to a given area. Thus, to increase pressure one can either increase the force being applied, or one can decrease the area. High pressures are generated in the diamond-anvil cell by taking a small force applied to a large area and transferring that same force to a small area.

Diamond is used as the anvil materials because it is very strong and hard, and hence does not deform under the very high forces involved in a pressure cell. Diamond is also transparent to electromagnetic radiation. Therefore it enables to study direct effect of pressure by many kind of experimental techniques such as X-ray diffraction and Raman spectroscopy.

$$\text{CRYSTAL} \underset{\text{(POLYMORPHISM)}}{\longleftrightarrow} \text{CRYSTAL}$$

$$\text{CRYSTAL} \underset{\text{(PRESSURE-INDUCED AMORPHIZATION)}}{\longrightarrow} \text{AMORPHOUS}$$

$$\text{AMORPHOUS} \underset{\text{(PRESSURE-INDUCED AMORPHIZATION)}}{\longleftarrow} \text{CRYSTAL}$$

$$\text{AMORPHOUS} \underset{\text{(PRESSURE-INDUCED CRYSTALLIZATION)}}{\longrightarrow} \text{CRYSTAL}$$

$$\text{AMORPHOUS} \underset{\text{(POLYAMORPHISM)}}{\longleftrightarrow} \text{AMORPHOUS}$$

Figure 1.2: Phase transitions in crystalline and amorphous materials. Right and left arrow indicates compression and decompression, respectively.

1.4 Phase transitions

Materials, disordered or crystal, exhibit different behavior under pressure depending on their topology and chemistry and hence phase transitions can be classified in different ways based upon thermodynamics, kinetics, thermochemical and structural consideration [12].

Thermodynamic analysis is a powerful tool, as it relates materials properties to macroscopic variables such as pressure, temperature, stress and composition. Thermodynamic classification of phase transitions was first proposed by Ehrenfest and is known as the Ehrenfest classification. Free energy (G) remains continuous during phase transitions while thermodynamic quantities such as volume (V), entropy, (S), heat capacity (C_P), compressibility (κ) and thermal expansion (α) exhibit discontinuity. The thermodynamic quantities and their relation with G are given as follows

$$V = \left(\frac{\partial G}{\partial P}\right)_T \tag{1.1}$$

$$-S = \left(\frac{\partial G}{\partial T}\right)_P \tag{1.2}$$

$$-V\kappa = \left(\frac{\partial V}{\partial P}\right)_T = \left(\frac{\partial^2 G}{\partial P^2}\right)_T \tag{1.3}$$

$$V\alpha = \left(\frac{\partial V}{\partial T}\right)_P = \left(\frac{\partial^2 G}{\partial P \partial T}\right) \tag{1.4}$$

$$-\frac{C_P}{T} = -\left(\frac{\partial S}{\partial T}\right)_P = \left(\frac{\partial^2 G}{\partial T^2}\right)_P \tag{1.5}$$

Ehrenfest classified phase transitions as functions of thermodynamic quantities which show a discontinuity. The order of a transition is the same than order of derivative G required to obtain a discontinuity. When the quantities in equations 1.1 and 1.2 exhibit a discontinuity, then the transition is first order. On the other hand, when the quantities in equations 1.3, 1.4 and 1.5 present a discontinuity, then the transition is second order.

For kinetic aspects, transitions can be characterized in two categories: (i) displacive and (ii) reconstructive. In the former case, the activation energies between phases are low and transformations are rapid. Most polymorphic phase transitions fall into this category. Displacive transitions proceed through the small distortion of bonds. For the reconstructive case, activation energy barriers are high and hence transformations are sluggish. These transitions involve heteregenous nucleation and are often diffusion limited. Reconstructive transitions proceed through the breaking of the primary or the secondary bonds.

In the thermochemical view, phase transitions are classified by the changes in entropy and enthalpy. However, data on changes of entropy and enthalpy are often not available. The classification is limited and also does not identify fundamental difference between phases [12].

The classification, however, does not provide a geometrical picture of structural change. Symmetry between phases sometimes appears to be important for revealing the mechanism of phase transitions. Transformations may involve simple distortions. For instance, a phase transformation diamond to β-Sn in silicon is a result of a tetragonal distortion along to the c-axis with no covalent bond breaking or large

atomic rearrangements even though the transition is first order with $\sim 20\%$ of volume drop. Therefore, the symmetry classification can be used to relate phases and paths of transitions. The symmetry systematics of pressure-induced phase transitions is categorized in four groups: iso-symmetric, group-subgroup, intersection group, and order-disorder [12, 13].

1.5 Pressure response for crystalline semiconductors

Most of the important semiconductors form in diamond/zinc blende structure with tetrahedral bonding. The elemental group IV semiconductors Si and Ge as well as III-V and II-IV compounds (GaAs, GaSb, InSb, etc.) belong to this family.

High pressure phases of these crystalline semiconductors have been extensively investigated because new phases may have application in electronics if they have desirable novel properties. Most of the high pressure phases of semiconductors are determined successfully, and hence the fundamental aspect of crystal to crystal (polymorphic) phase transitions of semiconductors are well understood empirically. However, there exists some doubts about the identity of a few high pressure phases.

Pressure yields broadening of bands and hence reduces the band gap energy. In many cases, the phase transition corresponds to abrupt closing of the band gap and the metallization of samples with a coordination change from four-fold to six-fold. In the sense of electronic application, the results are disappointing that the phases obtained on compression are semimetals or metals.

One of the important features is that some semiconductors transform to complex metastable phases on decompression [49]: BC8 (body centered cubic with an 8 atom basis), R8 (rhombohedral with an 8 atom basis), ST12 (simple tetragonal with a 12 atom basis) and SC12 (simple cubic with a 12 atom basis). These phases are characterized by varying degrees of distortion from the tetrahedral bonding, which are similar to those found in amorphous semiconductors. Therefore these metastable structures provide computationally trackable models for how an amorphous structure develops from a crystalline state and give insight into the physics of amorphous semiconductors. However, in order to achieve amorphization from an ordered structure, first it is necessary to understand the behavior of disordered systems under pressure.

1.6 Phase transitions in disordered materials

Pressure-induced phase transitions of amorphous semiconductors proceed through the structural modification. The transition can be gradual or abrupt (first order), and disordered networks transform into a high density crystalline or amorphous phase depending on temperature, sample preparation and loading history.

One puzzle is that in contrast to elemental amorphous semiconductors like Si and Ge [9, 10], most binary amorphous compounds [10] such as GaAs and GaSb undergo a gradual transition to a metallic phase at room temperature while their crystalline state exhibits a first order transition. No clear picture has emerged why a gradual transition occurs in amorphous compounds and a first order transition in elemental ones.

1.6.1 Pressure-induced crystallization

Disordered materials are thermodynamically unstable. Upon thermal annealing and pressurizing, they can be crystallized into stable or metastable phases. It appears that the pressure-induced crystallization is sensitive to sample properties as well as temperature and pressurizing conditions such as loading rate.

Disordered materials have excess free volume, i.e., their density is usually less than that of corresponding crystalline state. The free volume is released during the crystallization, and the system acquires a stable equilibrium state. The increase in density was suggested as a driving force for pressure-induced crystallization [15]. Yet this cannot be the sole reason for the crystallization because in polyamorphic phase transitions, density also dramatically increases. Polsky *et al.*[16] pointed out that underlying free energy surface of the liquid controls the high pressure behavior of these materials. However the nature of the crystallization procedure in disordered materials is not well-known yet.

At room temperature the crystallization of *a*-Ge[17, 18], *a*-Se[18], *a*-As[18], *a*-Si [19], *a*-GaAs[10] and *a*-GaSb [20] was reported in experiments. In *a*-Ge thin film, the crystalline portion of the network transforms to a high-density crystalline phase whereas amorphous parts remain amorphous after the transition [17, 18]. Therefore, the crystallization of *a*-Ge is referred as a partial structural transition. *a*-Si and *a*-GaSb samples obtained using pressure-induced amorphization technique undergo a phase transition into a crystalline phase. However, these transitions are questionable because the samples exhibit some anomalous physical properties, which are not seen in thin films.

Experimental studies have shown that temperature plays a very important role in pressure-induced crystallization. In a-$GeSe_2$ and a-GeS_2 the crystallization below a certain temperature is inhibited and a high-pressure modification of amorphous structures is formed [21]. Vitreous $ZnCl_2$ transforms to a crystalline phase at room temperature but, at low-temperature it undergoes a phase transition into a HDA phase [16]. This type of crystallization occurs below the melting point and is due to an annealing effect. At high temperatures, the energy barrier between phases is activated and systems find an easy path way for transforming to a crystalline state.

Information about pressure-temperature phase diagram of amorphous semiconductors is incomplete, and such a phase diagram would be very useful for determining high-pressure phases and understanding fundamental aspect of phase transitions in amorphous materials.

1.6.2 Polyamorphism

A system can have two liquid or amorphous states having the same chemical composition but different densities and degree of structural disorder, which are separated by a first order phase transition. The existence of such multiple liquid or amorphous phases is termed "polyamorphism". The occurrence of polyamorphism induced by pressure has been reported in several materials including H_2O[1, 2] and SiO_2 [7, 8]. Liquid-liquid transition has also been found in I, S, and Se[22, 23, 24]. In quenched Y_2O_3-Al_2O_3 systems, the existence of a first order transition between liquid phases has been reported[25].

Such a system with a different topology and density has distinct local minimums, which are separated at low temperature by a density gap in which there is no low energy states available for the system. Therefore, the system has an energy barrier and has to overcome the barrier by nucleating and growing induced by pressure.

The concept of pressure-induced polyamorphism began with H_2O in which a first order phase transition occurs between a low density amorphous phase and a high density amorphous phase. The transition is characterized by a sharp change in specific volume and enthalpy, which are reproducible and reversible except for hysteresis due to long relaxation time for glasses. It has been suggested that H_2O may have two coexisting structures and a second critical point at low temperatures [3, 4, 26, 27]. The second critical point traces the termination of a line of coexistence structures with isochemical composition but thermodynamically distinct densities which exist in supercooled region. Two amorphous states can be brought metastably across the coexistence boundary. The metastable region of each phase is bounded by its spinodal lines[4, 26]. At the spinodal line, no thermodynamic barrier for the phase transformation exists and the density fluctuations become infinite because of a restoring force. Then the stable phase nucleates.

Polyamorphism has been discussed for SiO_2 and GeO_2 since they are structurally somewhat similar to H_2O. However, the transition between polyamorphic phases in these glasses is gradual and hence the transformation is fundamentally different from that of H_2O. These glasses undergo a continuous increase in the average cation atom (Si and Ge) coordination from four-fold to six fold and simultaneously in the average anion (O) atom coordination from two-fold to three-fold [6, 7, 28, 29]. The

pressure-induced amorphous to amorphous phase transition is irreversible and the structures obtained upon decompression are about 20% denser than the precompressed structures. On the other hand, simulations of liquid and amorphous SiO_2 at high pressures [26] suggest that SiO_2 may also have a second critical point in the supercooled regime and a first order amorphous to amorphous phase transition below the glass transition temperature.

In a recent theoretical investigation based on Gibbs free energy calculation [7] a first order amorphous to amorphous phase transition in SiO_2 was proposed with a discontinuous volume drop of 16%, similar to that found in H_2O. It was argued that polyamorphic phase transition is kinetically hindered at low temperatures, and it is expected to be seen at high temperatures. Based on the theoretical prediction, an experiment was performed near glass transition temperature and a first order amorphous to amorphous transition in SiO_2 was confirmed around 1000 K[8].

The existence of polyamorphic phase transition was reported in some tetrahedrally bonded amorphous semiconductors [9, 10] before H_2O. However, the transitions have been little explored, and hence the nature of amorphous to amorphous phase transformation of these semiconductors needs experimental and theoretical investigations to clarify the concept of polyamorphism in the materials.

1.6.3 Anderson transition

Qualitative understanding of the electronic structure of disordered systems is based upon the Anderson model, which explains disorder induces localization of electron states. Consider a disordered potential field so that the energies of atomic orbitals

vary randomly from site to site. Atoms can form delocalized orbitals by their overlap when they have some neighbors at similar energies. When the atoms do not have neighbors at similar energies their orbitals will be isolated, and hence some eigenstates will decay exponentially away from the binding sites. States whose amplitude decay exponentially away from a center are called localized states.

There may be a boundary between localized and delocalized (extended) states, the so-called mobility edge. Existence of a mobility edge can give rise to a metal-insulator transition known as Anderson transition. The Fermi level may be in the mobility gap, in this case the electrons at the Fermi level are localized and cannot conduct current through a solid. With sufficient doping, the Fermi level may cross the mobility edge so that the carriers are in extended states and the metallic conduction is possible.

Recently Dong and Drabold [31] have presented a clear picture of Anderson transition in *a*-Si and proposed that this phenomena could be explained by resonant tunneling between clusters with similar electronic energies.

1.7 Pressure-induced amorphization

Rapid quenching from melts at high temperatures is a well-known method to produce amorphous materials. However, high pressure experiments have shown that high temperature is not always required, and pressure can serve as a powerful tool to obtain bulk amorphous samples through so-called pressure-induced amorphization. The different pressure-induced amorphizations are reported under compression

in H_2O[1], SiO_2 [32], $GeSe_2$[33], BAs [34], SiC[35] and some other materials, on decompression in H_2O [36], Si[37], Ge[37] and GaAs[187] and upon heating in GaSb [20]. These transformations have two common features; metastability of the initial crystal before the onset of disordering and a similarity between the amorphous phase obtained under pressure and the crystalline modification, which is stable at the amorphization conditions [38].

The amorphization in some materials cannot be achieved at room temperature but at sufficiently low temperatures that a system cannot transform to its equilibrium high-pressure crystalline phase. For instance, during relatively rapid pressure release when temperature decreases, the high-pressure modification of Si and Ge can undergo a transition from β-Sn to an amorphous structure rather than BC-8 [37]. The amorphization takes place without the involvement of melting.

Pressure-induced amorphization is due to the kinetic hindrance of either an equilibrium phase transition or equilibrium decomposition. It was suggested that crystal to amorphous phase transitions were fundamentally a thermodynamic melting transition, which is termed "cold melting" [1]. In this method, pressure-induced amorphization is assumed to be the low temperature analog of a melting process occurring on the melting curve extrapolated to low-temperatures. This method has been used to explain amorphization in metasable quartz [32] but the extrapolation does not seem to be valid for others [39, 40, 41].

It is also proposed that amorphization occurs as a result of mechanical instability [42, 43, 44], termed "mechanical melting". In this model the amorphization is considered as a result of phonon or elastic constants softening in the vicinity of phase

transition. It was proposed that not only pressure-induced amorphization but also amorphous to amorphous phase transition arises from phonon softening and mechanical instability of crystalline and amorphous structures [45]. However, simulations on SiO_2 [46] have shown that the bands shift into higher frequencies without mode softening with an increase of the density. Therefore, the puzzle remains unsolved.

Although the physical properties of low density bulk amorphous samples achieved under pressure are often similar to those of the corresponding thin films and samples obtained by direct quenching from melt, there are some distinctions [20], which are interpreted in the frame work of the "memory" effects from the initial crystal structure before the amorphization [38].

1.8 Difficulties in study of amorphous materials

The experimental study of pressure-induced phase transition of amorphous semiconductors has been hindered by difficulties in probing thin films. Thin films can be prepared in various ways, which yield structures with different physical properties. This means that amorphous structures are not unique in contrast to crystalline structures. It appears that depending on structural properties, different type of phases can form under pressure [9, 10, 17, 18].

The pressure-induced amorphization technique made it possible to achieve bulk samples of amorphous materials. However, the sample obtained with this technique have different physical properties than thin films. These distinctions may play an important role in determining the nature of phase transitions. For example, the pressure formed bulk amorphous sample of $GeSe_2$ does not show Ge-Ge bonding

in Raman-spectrum even though the melt-quenched glass does. We show below that homopolar bonding may determine the type of transition. The GaSb samples achieved using high pressure exhibit superconducting properties, which are, however, not presented in amorphous thin films. The samples obtained in this technique consist of high pressure states as well as large fraction of crystalline grains.

Perhaps stranger yet, pressure formed amorphous samples always show a pressure-induced crystallization. This transition is reversible because the initial bulk samples are prepared by depressurizing high pressure phases of their crystalline states [20]. However, the transition of thin films are not always reversible and the crystallization strongly depends on the properties of samples, temperature and loading condition. Although the exact reason of the crystallization of pressure formed bulk amorphous samples is not well-known, the large fraction of crystalline portion and the presence of high density disorder phase in the samples seem to be responsible for crystallization.

It is difficult experimentally to study amorphous structures in the same detail as crystalline structures. No experimental probes can yield a uniquely defined structure: only statistical averages of the structures via neutron scattering and x-ray measurements exist. The best method is to the use the structure factor from neutron scattering but it contains very little information. For a high pressure study, the method cannot be applied to small samples produced in high-pressure experiments using diamond anvil cells or thin films. Therefore reliable computer simulations are needed to study disordered materials in the wide range of temperature and pressure to provide detailed information about transition mechanism between two amorphous states and pressure-induced crystallization as well as their structural, electronic and

vibrational properties for each applied pressure. However, from a modeling perspective for amorphous semiconductors, there are two difficulties: the first one is the challenge of constructing large and realistic models. The second is lack of good empirical potentials. Thus understanding an amorphous structure requires extensive first principles calculations especially under pressure.

1.9 Total energy calculations

The pressure-induced phase transitions have been successfully explained from first principles calculations. These methods are mostly concerned with energy volume calculations and the thermodynamic criterion of Gibbs free energies. Most calculations are extremely precise and accurately distinguish the relative stability of phases. However, the methods can be only applied to "known structures". Recently, molecular dynamics (MD) simulations have made it possible to observe directly the dynamical aspect of solid-solid phase transitions with an increase of pressure. The equations of motions for MD under isobaric conditions were formulated by Andersen [47] and by Parrinello and Rahman [48]. The constant pressure MD of the Andersen method allows only for isotropic changes in the volume of the simulation box, and hence can not account for anisotropies in the internal stress. The generalization of Andersen's method taking this anisotropy into account is due to Parrinello and Rahman. In the Parrinello and Rahman method, not only the volume of a simulation cell but also its shape are dynamical variables.

1.10 Thermodynamics

Transition pressures can be calculated from the thermodynamic theorem that when a phase transformation occurs, the Gibbs free energy

$$G = E_{tot} + PV - ST \tag{1.6}$$

becomes equal between two phases. Here E_{tot} is the total internal energy, P is pressure, V is volume, T is temperature and S is the entropy. At zero temperature, the Gibbs free energy becomes the lattice enthalpy which is considered in the first principles calculations. Transformation occurs along the common tangent line between the total energy curves of the two phases. The negative slope of the tangent line gives the transition pressure.

From the Gibbs free energy it can be seen that a lower volume becomes favored as pressure increases and it is also evidence that temperature is less effective in proceeding solid-solid phase transitions since the entropy contribution to the solid to solid phase transition is the same in all crystals[49].

1.11 Equation of state

In high pressure investigations, an equation of state (EOS) is useful tool for transforming thermodynamical properties obtained at low pressures to condition at high-pressures. An EOS revealing volume as a function of pressure or temperature allows a reliable calculation of not only Gibbs free energy but also thermodynamic properties from Gibbs free energy. There are many proposed EOSs available in literature. The widely used EOS in high pressure study, the third-order Birch-Murnaghan EOS

[116] based on finite-strain theory, is given as a function of volume as follows

$$P(V) = \frac{3}{2}K\Big\{(V_\circ/V)^{7/3} - (V_\circ/V)^{5/3}\Big\}\Big\{1 - 3\Big(\frac{K'-4}{4}\Big)\Big[\Big(\frac{V_\circ}{V}\Big)^{2/3} - 1\Big]\Big\} \quad (1.7)$$

where $V_\circ$ is the equilibrium volume and K and K' are the bulk modules and its pressure derivative at zero temperature and pressure. Using the quantity $P = -dE/dV$, the equation can be rewritten as

$$E(V) = E_\circ + \frac{9}{8}KV_\circ[(V_\circ/V)^{2/3} - 1]^2\Big\{1 + \Big(\frac{4-K'}{2}\Big)\Big[1 - \Big(\frac{V_\circ}{V}\Big)^{2/3}\Big]\Big\}. \quad (1.8)$$

This equation is mostly used in total energy calculations in which internal energy of the system as a function of volume can be determined accurately. Fitting energy-volume data to the EOS yields Gibbs free energy and bulk modules and its pressure derivative at the equilibrium.

1.12 Objectives

Extensive theoretical and experimental investigations have been performed to study amorphous to amorphous phase transition in oxide glasses, which is due the fact that it is easy to achieve experimentally and theoretically glass forming networks. In contrast, knowledge of pressure-induced phase transition, especially amorphous to amorphous, in tetrahedraly bonded amorphous semiconductors is far from complete. The nature of polyamorphic transition, structural modification of amorphous networks, pressure dependence of volume, evolution of first neighbor shell, elastic properties and modification of electronic structure are not available. In this dissertation, the major task is to determine the high pressure phases of amorphous materials, and

particularly to develop *atomistic level* understanding of the pressure-induced amorphous to amorphous phase transition. We then proceed to study pressure-induced changes in electronic structure and vibrational spectrum. This includes *a*-Si, *a*-Ge, *a*-$GeSe_2$, and paracrystalline Si.

We also explore polymorphic phase transition in Si and Ge to calculate some physical properties of their high pressure phase and in GaAs to identify its high pressure phases which are subject to many speculations.

Chapter 2

Theoretical Foundation

2.1 Density Functional Theory

The ability to treat solids properties at a fundamental quantum level has improved tremendously since the advance of computer power has allowed to actually solve nonlinear coupled integrodifferential equations. Today it is possible to calculate and indeed *predict* many properties of materials using first principles method with few percent accuracy.

Density functional theory (DFT) provides a comparatively simple and computationally efficient approach for dealing with the quantum many body system in which the ground state many body problem is recast into the form of a singe-particle problem. DFT is based upon that the ground state energy is uniquely determined by the ground state electron density $n(\mathbf{r})$. The exact form of the density functional is unknown although excellent approximate forms do exist. Extensions of this scheme to spin-dependent, relativistic or time-dependent systems are also available. The main areas for applications of DFT are condensed matter and cluster physics as well as quantum chemistry.

Walter Kohn was awarded the 1998 Nobel Prize in Chemistry for his development of the DFT. W. Kohn's theoretical work has formed the basis for simplifying the mathematics in descriptions of the bonding of atoms, a prerequisite for many of today's calculations

2.1.1 Hohenberg-Kohn theory

In the Hartree-Fock theory the approach to the problem is to calculate the wave function from the Schrödinger equation using the variational principle of quantum mechanics and a single Slater determinant. Another approach is the DFT where the electron density $n(\mathbf{r})$ plays the central role. Hohenberg and Kohn 1964 [50] first formulated the fundamental theoretical basis of DFT. The theorem states that for any electronic systems in an external potential $V_{ext}(r)$, the Hamiltonian is fully determined by the ground state density. In other words, the electron density of the ground state can be used to represent completely and uniquely the interacting electrons system. This means that, in the ground state, if the electron density is known, it is possible to calculate all properties of the system. In particular it provides us the full Hamiltonian and all physical properties which can be obtained from it.

Since the electron density uniquely determines the ground state energy, it is possible in principle to express the functional dependence of E on $n(\mathbf{r})$ as $E[n]$. In $E[n]$, it is possible to extract the energy term that describes the external potential so the total energy can be expressed as

$$E[n] = F[n] + \int V_{ext}(\mathbf{r}) n(\mathbf{r}) d\mathbf{r} \tag{2.1}$$

here $V_{ext}(\mathbf{r})$ is the external potential that includes the potential from the nuclei:

$$V_{ext}(\mathbf{r}) = -\sum_{\alpha} \frac{Z_\alpha}{|\mathbf{r}-\mathbf{r}_\alpha|} + \frac{1}{2N}\sum_{\alpha\beta} \frac{Z_\alpha Z_\beta}{|\mathbf{r}_\alpha - \mathbf{r}_\beta|}. \tag{2.2}$$

in which the electron move, which contains the Coulomb interactions between electron and nuclei and internuclear Coulomb interactions.

$F[n]$ is a unique and universal functional of density, and hence it does not depend on $V_{ext}(\mathbf{r})$. $F[n]$ contains the kinetic energy and the electron-electron interaction energy:

$$F[n] =< \psi|T + V_{ee}|\psi > \tag{2.3}$$

where ψ is the unknown many electron wave function. The explicit form of $F[n]$ is not known. If we knew the functional form of $F[n]$, we would be able to easily obtain the ground state solution by minimizing $E[n]$ with respect to variations of the electron density of system. $F[n]$ may be separated into three terms.

$$F[n] = T[n] + e^2 \int \frac{n(\mathbf{r})n(\mathbf{r}')}{|\mathbf{r}-\mathbf{r}'|}\, d\mathbf{r}'d\mathbf{r} + E_{xc}[n]. \tag{2.4}$$

Here $T[n]$ is the kinetic energy of a non interacting electron gas with the same density as in the problem considered, the second term is the ordinary Coulomb term (the Hartree energy) and the third term is the exchange and correlation term. $E_{xc}[n]$ contains all quantum effects like Pauli exclusion principle effects and kinetic energy contributions that are not taken into account in the idealized term $T[n]$.

2.1.2 The Kohn-Sham Ansatz

Further progress on the practical use of the Hohenberg-Kohn theorems was made by Kohn and Sham[51]. In order to compute the kinetic energy of the interacting system, Kohn and Sham introduced a set of orthonormal orbitals as a basis for the charge density:

$$n(\mathbf{r}) = 2\sum_{i=1}^{N} |\psi_i(\mathbf{r})|^2 \tag{2.5}$$

where $\psi_i(\mathbf{r})$ is the Kohn-Sham orbital. The kinetic energy of non-interacting system then can be computed as

$$T_s[n] = \sum_{i=1}^{N} < \psi_i| - \frac{\hbar}{2m}\nabla^2|\psi_i > . \tag{2.6}$$

Using this definition we can rewrite the energy functional as:

$$E[n] = T_s[n] + E_H[n] + E_{xc}[n] + \int V_{ext}(\mathbf{r})n(\mathbf{r})\ d\mathbf{r}. \tag{2.7}$$

Once the energy functional has been expressed in the form of equation 2.7 and the electron density as its form in the non-interacting electronic system, the equations can be developed further by imposing the variational nature of the ground state solution. Kohn and Sham showed that, minimizing the total energy with respect to the non-interacting electronic state $\psi_i(\mathbf{r})$, and imposing them to be orthogonal, it is possible to rewrite the Schrödinger equation and obtain the so called Kohn-Sham equation which takes the form of a single particle Schrödinger equation

$$\hat{H}_{eff}\psi_i(\mathbf{r}) = [-\frac{\hbar}{2m}\nabla^2 + V_{eff}(\mathbf{r})] = \epsilon_i\psi_i(\mathbf{r}) \tag{2.8}$$

where $V_{eff}(\mathbf{r})$ is the complicated effective potential that the non interacting particles move in. The expression for $V_{eff}(\mathbf{r})$ is

$$V_{eff}(\mathbf{r}) = V_{ext}(\mathbf{r}) + V_{xc}(\mathbf{r}) + e\int \frac{2n(\mathbf{r})}{|\mathbf{r}-\mathbf{r}'|}\, d\mathbf{r}. \tag{2.9}$$

Both the Hartree and Exchange correlation potential are non-local functionals of the charge density and hence the effective potential at each point depends on the electronic charge in the all points of space. The exchange-correlation potential functional derivative of the exchange-correlation energy;

$$V_{xc}(\mathbf{r}) = \frac{\delta E_{xc}[n]}{\delta n(\mathbf{r})}. \tag{2.10}$$

The Kohn-Sham equations must be solved self-consistently because the effective potential is a functional of the charge density which is determined by the effective potential.

2.1.3 The Local Density Approximation

The local density approximation (LDA) is the simplest but surprisingly useful approximation to the exchange-correlation functional. It is based on the assumption that, for regions of a material where the charge density is slowly varying, the exchange correlation energy at that point can be considered the same as that for a locally uniform electron gas of the same charge density. It was first proposed by Kohn and Sham [51], and E_{xc} could be approximated as

$$E_{xc} = \int n(\mathbf{r})\varepsilon_{xc}[n(\mathbf{r})]d\mathbf{r} \tag{2.11}$$

where ϵ_{xc} is the exchange correlation energy density of a uniform electron gas of density $n(\mathbf{r})$. This approximation is extremely simple but, it is surprisingly accurate,

and forms the core of most modern DFT codes. It even works reasonably well in systems where the charge density is rapidly varying.

2.2 Method

One of the important and computationally less extensive implementation to DFT was proposed by Sankey, Niklewski and Drabold [52]. This method is ideal for large and complex systems. The first major approximations are the use of the Kohn and Sham local density approximation and pseudopotential approximation. The local exchange-correlation functional of Cerpeley and Alder [53] as parametrized by Perdew and Zunger[54] and the nonconserving Hamann-Shlüter-Chiang[55] type are used. In order to avoid the difficulties associated with iteration to self-consistency, the Harris functional [56] is adopted. The sum of neutral-atom spherical charge densities are considered as a first order approximation to the self-consistent density and only the first order changes from this density in the energy functional is kept. The self-consistent electron density can be written as

$$n(\mathbf{r}) = n_\circ(\mathbf{r}) + \delta n(\mathbf{r}) \tag{2.12}$$

where $n_\circ(\mathbf{r}) = \sum_\alpha n_{atom}(\mathbf{r} - \mathbf{r}_\alpha)$ which is used as a input density in the Khon-Sham eigenvalue equation to generate wave functions and hence approximate $\delta n(\mathbf{r})$. The wave functions yield an approximate density

$$\tilde{n}(\mathbf{r}) = 2 \sum_{i\ occ} |\tilde{\psi}_i(\mathbf{r})|^2 = n_\circ(\mathbf{r}) + \delta\tilde{n}(\mathbf{r}). \tag{2.13}$$

The density change $\delta\tilde{n}(\mathbf{r})$ reflects the formation of bonds and is the first order approximation to the self-consistent bond forming given by $\delta n(\mathbf{r})$.

The Kohn-Sham wave functions are expanded a linear combination of pseudo-atomic atobitals(PAO's):

$$|\psi_i(\mathbf{r})\rangle = \sum_{\mu\alpha} a_i(\mu,\alpha)|\varphi_\mu^{PAO}(\mathbf{r}-\mathbf{r}_\alpha)\rangle. \tag{2.14}$$

The pseudoatom contains only the valence electrons and hence the orbital types μ are s, p_x, p_y and p_z. In order to reduce the range of interaction between atomic orbitals, and hence greatly reduce the number of neighbors each atoms interacts with, the boundary condition is imposed that the atomic orbitals vanish outside and at a predetermined radius r_c:

$$\varphi^{PAO}(\mathbf{r})|_{r=r_c} = 0. \tag{2.15}$$

The limit of $r_c \rightarrow \infty$ gives the exponentially decaying true pseudo atomic orbitals. This boundary condition has the physical effect of mixing in slight amounts of excited orbitals of the atom inside r_c. This can be seen by adding a small amount of the $2S$ wave function to the hydrogen-atom $1S$ ground state.

2.3 Classical Molecular Dynamics

Molecular dynamics is a powerful computational method to study dynamical and structural properties of materials at atomistic level. The equations of motion of atoms in a simulation box are solved using an interatomic potential. The potential contains a number of adjustable parameters which can be obtained by fitting to physical quantities like cohesive energy, lattice constants, structural parameters, etc., given by experiments or *ab initio* MD simulations.

Use of periodic boundary conditions is customary to simulate infinite systems. Thermodynamic variables such as pressure and temperature can be defined (even if they will fluctuate a bit because the number of particles is finite), and the technique can be used to study a large number of phenomena including phase transitions, liquid structures, defects in solids (vacancies, dislocations, grain boundaries, etc), amorphous materials, surfaces, clusters.

Classical MD simulations have been employed to investigate solid to solid and liquid to liquid phase transitions using various algorithms which allow both volume and shape of simulation cells to change in response to external pressure and stress. These simulations are very useful for understanding of phase transitions at a microscopic level, determining the transition paths, and electronic and vibrational properties at each applied pressure.

Classical MD simulations have been applied to study crystal to crystal phase transition in SiO_2 and GeO_2 , pressure-induced amorphization in SiO_2 [43, 44] and amorphous to amorphous phase transformation of SiO_2[7]. Depending on empirical potentials employed and simulation procedures, high-pressure phases with different local structure were reported in simulations.

Several empirical potentials generated by fitting parameters to experimental data are available for silicon, and they are employed to study structural properties and phonon spectra. The results obtained from these empirical potentials appear to be in quantative agreement with experiments. Tersoff[57] and EDIP[58] potential were applied to study high-pressure phase transitions in crystalline and amorphous silicon[59, 60, 61]. Diamond to β-Sn phase transition was predicted successfully at 64

GPa[59] and 60 GPa[60]. Even though the transition pressure predicted in both simulations larger than experiment(8-15 GPa), the transformation mechanisms between these phases were clearly explained. In the case of amorphous Si and Ge, a continuous amorphous to amorphous phase transformations was obtained using Tersoff and EDIP potential, but in the same study, the Gibbs free energy calculations suggested a first order polyamorphic phase transitions in a-Si and a-Ge [61]. The zero-pressure amorphous models used in these simulations were generated by quenching from the melt. However it is well-known that this technique does not work well for a-Si and a-Ge[62]. Therefore it is not clear whether the contradictory transitions (gradual or first order) are due to the empirical potentials or the zero-pressure amorphous models.

An empirical potential was used to investigate pressure induced phase transition in GaAs[63] and nanocrystalline GaAs[64]. In both studies, a transition from zincblende to a rocksalt structure were reported. On the other hand, experiments showed that GaAs-II phase is *Cmcm* which is slightly disordered rocksalt structure.

2.4 Ab Initio Molecular Dynamics

The ab initio molecular dynamics (MD) method allows to simulate the motion of the individual atoms based on forces which are calculated quantum mechanically. In mid eighties Roberto Car and Michele Parrinello [65] initiated this method and combined Density Functional Theory with classical mechanics (Newton's law for the nuclei) in a joint set of equation of motion. CP simulation refers to a molecular dynamics calculation using a plane wave basis and an iterative minimization scheme

to solve the electronic structure problem (the self consistent LDA equations). More properly, CP refers only to a method for coupling the approximation of stationary states of giant basis eigenvalue problems with associated ionic dynamics.

This work, and subsequent work by Sankey, Niklewski and Drabold with a local basis representation for the density functional orbitals, has enabled the theorist to study the dynamics of a system (a crystalline solid, a liquid or one to several molecules) at finite temperatures. Due to the explicit treatment of the electronic structure and the resulting forces acting on the atoms, forming and breaking of bonds can be studied in contrast to conventional MD calculations done in the past. Nevertheless there are severe limitations on the size of systems which may be addressed, the length of simulations possible, and the local density approximation (LDA) itself.

Recently the combination of CP technique with Parrinello and Rahman method was used to study of pressure-phase transition in several materials[66, 67, 68, 69, 70]. However, the calculations were mostly performed to investigate crystal to crystal phase transitions in small size of cells (64 atom or less) and cluster. Some of these simulations gave the detailed description of transformation mechanism, transition paths, structural and electronic properties of compressed phases. As seen in classical MD simulations, the predicted transition pressures in these calculations are also larger than experimental results. It appears that critical pressures predicted in *ab initio* method is not as high as those of classical MD method.

2.5 Pressure Control

Constant pressure simulations with variable supercell geometry are desirable to investigate a solid to solid phase transition with a change of symmetry. Andersen [47] first introduced a constant pressure MD, in which isotopic fluctuations in volume of simulation cells is allowed and hence the size of the cells is considered as a dynamical variable. A powerful extension of the Andersen method was introduced by Parrinello and Rahman [48]. This method also allows for changes of the shape of simulation supercells because of external stress or pressure.

In the Parrinello-Rahman method, nucleation for solid to solid phase transitions are suppressed because of the finite size of the simulation cells with periodic boundary conditions and the short time scale of simulations and hence the method overestimates transition pressures. The large value of the metasable transition pressure can be attributed to an intrinsic activation barrier and hence the simulation cell superpressurized. Nevertheless, it is widely used technique in high-pressure investigations.

In order to overcome difficulties due to the use of periodic boundary conditions and to perform more realistic calculations, new simulation techniques have been developed. One popular technique is that pressure is applied via a liquid state to simulation clusters without using periodic boundary conditions[64]. In this method, a large cluster is embedded in a hydrostatic medium for which a liquid (mostly Lennard Jones liquid) is chosen. The interaction between the atoms in the liquid and the atoms in the cluster is chosen to be repulsive in order to prevent the liquid atoms from entering the cluster. In this technique, a large number of atoms of liquid state and cluster are required and hence it is only applied in classical MD simulations.

2.5.1 Andersen Method

In this method, the volume of simulation cell is treated as a dynamical variable and hence the simulation cell is allowed to change its volume but not shape. A constant shape also makes the dynamics analysis easier. However, this method is not very useful for studying materials under nonisotropic stress or phase transitions,

2.5.2 Parrinello and Rahman Method

The Parrinello-Rahman method[48] is invented to allow for isotropic fluctuation in the volume of simulation cells. The method enables simulation cells to change shape and volume and hence the internal stress of the system can match the externally applied stress. For a simulation cell with lattice vectors $\mathbf{a}, \mathbf{b}$ and $\mathbf{c}$, a 3x3 matrix $\mathbf{h}$ formed by $\{\mathbf{a}, \mathbf{b}, \mathbf{c}\}$, can be defined such that the volume of simulation cell is given by $\Omega = det\mathbf{h} = \mathbf{a}.\mathbf{bxc}$. The position of particles i then can be written in terms of scaled coordinates $\mathbf{S}$: $r_i = \zeta_i\mathbf{a} + \eta_i\mathbf{b} + \xi_i\mathbf{c} = \mathbf{h}\mathbf{S}_i$ where $\mathbf{S}_i$ has components (ζ_i, η_i, ξ_i) each going from 0 to 1. The Lagrangian can be written by

$$L = \frac{1}{2}\sum m_i\dot{\mathbf{S}}_{i'}\mathbf{G}\dot{\mathbf{S}}_i - \sum_i\sum_{i>j}\varphi(\mathbf{r}_{ij}) + \frac{1}{2}WTr(\dot{\mathbf{h}}^{\mathbf{t}}\dot{\mathbf{h}}) - P_{ext}\Omega. \tag{2.16}$$

Here $\mathbf{G} = \mathbf{h}^{\mathbf{t}}\mathbf{h}$ is a metric tensor which converts distances measured in scaled coordinates to distances in original coordinates, $\varphi(r)$ is a pair potential, P_{ext} is the external hydrostatic pressure, $\mathbf{h}^{\mathbf{t}}$ is transpose of $\mathbf{h}$ matrix and W is the fictitious mass or inertia parameters controlling the time scale of motion of the cell $\mathbf{h}$. The

equation of motion can be defined as

$$\ddot{\mathbf{S}} = m_i^{-1} \sum_{i \neq j} \chi(\mathbf{r}_{ij})(\mathbf{S}_i - \mathbf{S}_j) - \mathbf{G}^{-1}\dot{\mathbf{G}}\dot{\mathbf{S}}_i, \tag{2.17}$$

$$\ddot{\mathbf{h}} = W^{-1}(\pi - P_{ext})\sigma \tag{2.18}$$

where $\chi(r)$ is $-d\varphi/rdr$. The matrix σ has elements $\sigma_{ij} = \delta\Omega/\delta\mathbf{h}_{ij}$, and the matrix π is given in dyadic tensor notation by

$$\Omega\pi = \sum_i m_i \mathbf{v}_i.\mathbf{v}_i + \sum_i \sum_{j>i} \chi(\mathbf{r}_{ij})(\mathbf{r}_i - \mathbf{r}_j)(\mathbf{r}_i - \mathbf{r}_j) \tag{2.19}$$

here $\mathbf{v}_i = \mathbf{h}\dot{\mathbf{S}}_i$. Equation 2.17 and 2.18 govern the dynamic of a simulation box with N particles under periodic boundary conditions. Equation 2.18 gives the relation between the variation of $\mathbf{h}$, the microscopic tensor π and the external pressure.

In the density functional theory, the Kohn-Sham wave functions $\psi_i(\mathbf{r})$ are normalized on cell $\mathbf{h}$ and they are not independent fields because $\mathbf{h}$ are Lagrangians degree of freedom. The wave function have to be expressed in the scaled coordinates $\mathbf{s} = \mathbf{h}^{-1}\mathbf{r}$. The orbital $\psi_i(\mathbf{r})$ as defined in unscaled cell $\mathbf{h}$ are transformed according to

$$\psi_i(\mathbf{r}) = \frac{1}{\sqrt{\Omega}}\psi(\mathbf{h}^{-1}\mathbf{r}) = \frac{1}{\sqrt{\Omega}}\psi(\mathbf{s}). \tag{2.20}$$

The resulting charge density in the unit cell is given by

$$n(\mathbf{r}) = \frac{1}{\Omega}n(\mathbf{s}). \tag{2.21}$$

The scaled fields $\psi(\mathbf{s})$ and charge density $n(\mathbf{s})$ do not depend on the dynamical variables associated with to the cell degrees of freedom. However original $\psi(\mathbf{r})$ depends on the cell variables $\mathbf{h}$ by the normalization of the cell volume Ω=det$\mathbf{h}$.

The Lagrangian for *ab initio* molecular dynamics with pressure control can be generalized as follows[67]

$$L = \mu \sum_i \int d\mathbf{s}|\psi_i(\mathbf{s})|^2 + \frac{1}{2}\sum_j M_j(\dot{\mathbf{S}}_j^i G \dot{\mathbf{S}}_j) - E[\{\psi_i\},\{\mathbf{hS}_j\}] +$$
$$+ \sum_{il} \Lambda_{il}\Big(\int d\mathbf{s}\psi_i^*(\mathbf{s})\psi_l(\mathbf{s}) - \delta_{ij}\Big) + \frac{1}{2}WTr(\dot{\mathbf{h}}^{\mathbf{t}}\dot{\mathbf{h}}) - P_{ext}\Omega, \tag{2.22}$$

with additional nine dynamical degrees of freedom that are associated to the lattice vectors of simulation cell $\mathbf{h}$. Note that the integrals are taken on the scaled simulation box. $E[\{\psi_i\},\{\mathbf{hS}_j\}]$ is the DFT-LDA energy functional and δ is the identity matrix. The fourth term is the orthonormality constraint on the ψ_i and Λ_{il}, which are Langrangian multipliers. W is the same as in the classical PR and μ is inertia parameters that control the time scale of electronic motion. M_j are the mass of nuclei. The Lagrangian enables for symmetry breaking fluctuations which is necessary to drive a solid to solid phase transformation. The equations of motion in DFT-LDA scheme are

$$\mu\ddot{\psi}_i(\mathbf{s}) = -\frac{\delta E}{\delta\psi_i^t(\mathbf{s})} + \sum_l \Lambda_{il}\psi_i(\mathbf{s}) \tag{2.23}$$

$$\ddot{\mathbf{S}}_j^\alpha = -\frac{1}{M_j}\frac{\partial E}{\partial \mathbf{S}_j^\beta}\mathbf{G}_{\alpha\beta}^{-1} - \mathbf{G}_{\alpha\beta}^{-1}\dot{\mathbf{G}}_{\beta\gamma}\dot{\mathbf{S}}_j^\gamma \tag{2.24}$$

$$\ddot{\mathbf{h}}_{\alpha\beta} = \frac{1}{W}(\pi_{\alpha\gamma} - P_{ext}\delta_{\alpha\gamma})\Omega(\mathbf{h}^t)_{\gamma\beta}^{-1} \tag{2.25}$$

where $\pi_{\alpha\gamma}$ is

$$\pi_{\alpha\gamma} = \frac{1}{\Omega}\Big(\sum_j M_j\dot{\mathbf{S}}_j^t\mathbf{G}\dot{\mathbf{S}}_j)_{\alpha\gamma} - \frac{\partial E}{\partial h_{\alpha\beta}}\mathbf{h}_{\delta\gamma}^t\Big) \tag{2.26}$$

Here the equation 2.23 is the same as the original CP Lagrangian because of the normalization choice of $\psi(s)$ and the equations 2.24 and 2.25 are the same as in classical PR method such that quantum mechanical expressions are replaced for the classical forces on ions and the internal stress.

2.6 Modeling Amorphous Structures

The major hurdle for getting the right electronic picture of amorphous structures is the limited availability of high quality structural models. The atomistic models in agreement with experimental measurements are likely to lead to useful new insights. The usual shortcoming of structural models is an unphysical concentration of defects The presence of a large number of defects in close proximity in energy and real space (inevitable in a small supercell model) implies delocalization of the defect wave functions. This unphysical delocalization then impacts any calculation of transport or photo-structural change. It is not even obvious that structural and dynamical characteristics of such a model are reliable. This is because some of the artificially extended defect states may be *occupied*. The generation of defect-free models is therefore fundamental to the understanding of the role of realistic defects and nature of the band tails in amorphous semiconductors.

Different techniques are needed to construct realistic models of amorphous materials depending on the specific chemistry and order of materials.

2.6.1 Continuous Random Network

The atomic structure of covalently bonded disordered materials is generically well represented by the continuous random network (CRN) first introduced by Zachariasen [71]. In this picture, the material is assumed to consist of building blocks of tetrahedra similar to those in crystalline states but randomly oriented and connected. The interest of this model lies in its simplicity: the requirement of the model is that each atom should satisfy fully its bonding needs, that is, all atoms should be ideally coordinated. The quality of a CRN is generally determined by the amount of strain, as measured by the local deviations from crystalline environment. The first CRN model was constructed by Polk[72], and the model provided a satisfactory description of the topology of elemental amorphous semiconductors.

2.6.2 Wooten Winer and Weaire Method for tetrahedral amorphous materials

The bond switching method of Wooten, Winer and Weaire (WWW)[73] involves following steps: (1)Atoms are packed a perfect crystalline structure. (2) Close to the melting temperature, the crystalline structure is randomized by large number of WWW bond switching. The WWW switchings are accepted with the Metropolis acceptance probability

$$P = Min[1, exp(E_i - E_f)/k_b T] \tag{2.27}$$

here k_b is Boltzmann constant, T is temperature, E_i is the total energy of system before the proposed bond transposition and E_f is the total energy of the system

after bond transposition. In this procedure the memory effect can be eliminated and the system cannot return to the crystalline structure. (3) While temperature decreases slowly and the equilibrium configuration is obtained at each temperature, the network subjected to bond switching method.

Although this method enables us to construct a realistic model, it has several disadvantages. Mousseau and Barkema [74] have introduced an improvement version of WWW method. In this method, atoms are first packed randomly in a box, at crystalline density. A connectivity table is then constructed by constructing a loop that passes exactly twice through each atom. The network is then relaxed, using the fixed list of neighbors and a Keating potential. These steps ensure that the initial state has no trace of crystallinity. The models are then relaxed in a series of WWW moves and additional massaging, using the accelerated algorithm. The flexibility of such static methods allows the creation of high quality amorphous network with relatively little computational effort.

There is no doubt that the best *a*-Si models are generated from the WWW and the improved version of the WWW method. Models agree remarkablely well with structural, vibrational and optical measurements[62]. Barkema and Mousseau have shown that the WWW bond switching appear to actually happen frequently in the long time dynamics of *a*-Si using the Activation Relaxation Technique (ART)[75] which is capable of tracking some of these dynamics.

2.6.3 Quenching From Melt

The WWW method and the modified version of the WWW is limited to the case of elemental amorphous tetrahedral materials and cannot be employed to construct binary amorphous compound since it introduce wrong bonds. This limitation of the WWW algorithm and absence of alternative method have hindered the study amorphous compounds. An alternative scheme for constructing an amorphous structure is the quenching from melt.

MD simulation mimics the experimental procedure of constructing of an amorphous structure from its liquid phase. The initial crystal structure is melted at high temperatures so that the structure transforms to a liquid phase. Then a simulated annealing procedure is performed to the system to relax to a local the minimum energy state. The major limitation of MD simulations is the short time scale.

When a binary compound is cooled from its liquid phase the time scale for chemical ordering depends strongly on the ionicity of materials. Therefore, the method can be successfully applied on the systems which compel strong chemical order such as SiO_2 and GeO_2. In contrast, simulations on slightly ionic materials such as GaAs have not given clear indication of chemical order. On the other hand, *ab initio* time scale appears to be long enough to generate models with correct chemistry and topology in a-$GeSe_2$[76] and a-As_2Se_3 [77] whose bonding structure of liquid phase is similar to their solid phase. However this method has never worked well for a-Si and a-Ge because the bonding structure of solid germanium and silicon is different from that of melt. Therefore, the method tends to produce a model containing some liquid phase fragment and large numbers of unphysical defects.

2.6.4 Activation Relaxation Technique

Barkema and Mousseau [74] have introduced the activation relaxation technique (ART). This technique can be applied to investigate the long time dynamics of amorphous networks and to construct realistic models at global minimum.

ART can be defined a way to move a configuration on a continuous energy surface from one local minimum to another, going through an adjacent saddle point. The first step is to bring a configuration from a local minimum to a near saddle point (activation). The second step is to relax the configuration to a new minimum (relaxation). The method has been successfully applied to a-Si and a-GaAs models which are used in the present study.

Unfortunately ART has been used for only empirical potentials, which limits the study of compound amorphous structures, especially chalcogenide glasses, because no good empirical potentials are available.

Chapter 3

Ab initio calculation of electronic structure of amorphous silicon

3.1 Introduction

Amorphous silicon is an important material because of its applications in electronic and photoelectronic industry and its role as the archetype of disordered system. Applications of the material depend strongly on the nature of electron states near the Fermi level. Therefore there have been very large number of studies of electron states of a-Si [31, 78, 79, 80].

The major hurdle for getting the right electronic picture of a-Si is the limited availability of high quality structural models. Models generated with molecular dynamics (MD) generally show an unrealistic defect concentration and barely exhibit an optical gap. The presence of a large number of defects in close proximity in energy and real space (inevitable in a small supercell model) implies delocalization of the defect wave functions. This unphysical delocalization then impacts any calculation of transport or photo-structural change. It is not even obvious that structural and

dynamical characteristics of such a model are reliable. This is because some of the artificially extended defect states are *occupied*. The generation of defect-free models is therefore fundamental to the understanding of the role of realistic defects and nature of the band tails in amorphous semiconductors.

In this study, we compute electron eigenstates of 2 large 1000-atom realistic models of *a*-Si using an approximate *ab initio* scheme. This is close to the maximum size that can be treated with *ab-initio* MD at present. These models were prepared using an improved version of the Wooten-Winer-Weaire (WWW) algorithm[74] and were each relaxed with both a Keating [81] and a modified Stillinger-Weber potential [82], for a total of 4 different configurations. All the configurations are perfectly four-fold coordinated with a narrow bond-angle distribution, almost 2 degrees below the next best available numerical models and on a par with experimental values [83]. Because of the low density of strain in the network, the electronic density of states (EDOS) of these models also show a clean gap, with no state extending beyond the Urbach tails. To our knowledge, these are the first models of *a*-Si to show a perfect wide gap. Analyzing the states in the band tails, we find that one of the models has only very weakly localized electronic states, leading to extended 1D string-like structures while the 3 others show a significant degree of localization near the band edge. The results obtained generally confirm a recent study of *a*-Si[31].

3.2 Theoretical Consideration

The models used here were generated by Barkema and Mousseau [74] using a significantly improved version of the WWW algorithm [73]. The details of the preparation are reported in [74] and we just give a brief review here. Two independently generated 1000-atom models of a-Si were created.

Atoms are first packed randomly in a box, at crystalline density, with the single constraint that no two atoms be closer than 2.3 Å. A connectivity table is then constructed by constructing a loop that passes exactly twice through each atom. The network is then relaxed, using the fixed list of neighbors and a Keating potential. These steps ensures that the initial state has no trace of crystallinity. The models are then relaxed in a series of WWW moves and additional massaging, using the accelerated algorithm discussed in [74]. The flexibility of such static methods allows the creation of high quality amorphous network with relatively little computational effort.

The two independent models were finally relaxed, at zero pressure, with both a Keating and a modified Stillinger-Weber potential, leading to 4 different configurations: K1 and mSW1, and K2 and mSW2. Both K1 and mSW1 share a common topology but present slight differences regarding structural and electronic properties, including density and strain. The same applies, of course, to K2 and mSW2. All supercells have perfect four-fold coordinations with a narrow bond angle distribution $\Delta\theta = 9.21, 9.20, 9.70, 9.77$ for K1, K2, mSW1 and mSW2 supercells respectively.

The use of two potentials is made necessary because it is not numerically reasonable to relax a 1000-atom cell *ab initio*. In order to assess the error generated by studying the electronic properties of models structurally optimized for empirical potential, we tested the total energy per atom with a 216- atom model of a-Si. The model was relaxed with both the modified Stillinger-Weber potential and the FIREBALL96 program of Demkov, Sankey, Ortega and Grumbach [84], which generalizes the non-self consistent minimal basis Harris functional local density approximation scheme of Sankey and Niklewski [52]. This program has been successfully applied in a wide range of amorphous systems a- Si [78], a -GaN [85], a -C [86] and $GeSe_2$ [76].

In order to characterize the localized electronic states, we define the Mulliken charge [87], $Q(n,E)$, for atom n associated with the eigenvalue E. This charge can then be used as a measure of the localization of a given state

$$Q_2(E) = N \sum_{n=1}^{N} Q(n,E)^2 \tag{3.1}$$

where N is the number of atoms in a supercell. For a uniformly extended state, $Q_2(E)$ is 1, while it is N for a state perfectly localized on a single atom.

In amorphous and glassy substances, $Q_2(E)$ cannot be unity since the weight of even the most delocalized electronic states will fluctuate from site to site. This does not mean that the states are localized in the sense of charge falling off exponentially in an infinite model; it merely reflects the disordered nature of the model. In any finite sample, moreover, it is virtually impossible to define exactly where the band tail ends.

Table 3.1: Total energy per atom, their energy difference with c-Si, and the density of the models.

Model	K1	K2	mSW1	mSW2
E^a_{tot} /atom (eV)	-107.765	-107.698	-107.810	-107.827
(E^a_{tot}/atom -E^c_{tot} /atom) (eV)	0.229	0.296	0.1841	0.167
ρ(gr.cm^{-3})	2.335	2.436	2.200	2.196

3.3 Results and Discussions

The total energy per atom, E^a_{tot}/atom, the density of the models and their energy difference with c-Si (E^c_{tot}/atom=-107.994 eV) are given in Table 3.1. The energy difference of mSW1 and mSW2 supercells is good agreement with a study of nonorthogonal tight-binding model [59]. However, the difference is a factor of two higher than an experimental result 0.0977 eV, as extrapolated to 0 K from the measurement at 960 K using the specific heat listed in that work [89].

The configurational energy of the K1 and K2 models is significantly higher than that of mSW1 and mSW2. This is due to the fact that the optimal density of amorphous models relaxed with Keating potential is slightly higher than that of the crystal (ρ = 2.243 g/cm^3) while the modified Stillinger-Weber potential favors a density slightly lower, in agreement with experiment.

The EDOS of the 4 supercells is given in Figure 3.1(a). The energy bands are rather broad with band tails going into the gap. The disordered nature of a-Si is responsible for the band tails, especially valence tail and the conduction tails

Table 3.2: The optical gap of the models.

Model	K1	K2	mSW1	mSW2
Gap (eV)	1.15	1.35	0.85	0.8

are dominated by thermal rather than structural disorder [90].The region around the electronic gap is shown in more detail in Figure 3.1(b). The absorption edge, extending into the gap, is called an Urbach edge and should show an exponential decay. Fig3.1(c) and (d) present a fit of this function, $\rho(E) \propto exp(-E/E_0)$, for K1 and mSW2. In both cases, the fit is reasonable with a similar fitting parameter, $E_0 = 0.185$ eV and $E_0 = 0.205$ eV, respectively. This is in agreement with previous calculations [31].

The optical gap of the cells is summarized in Table 3.2. Comparing to the gap of the crystalline model, 1.55 eV, all models exhibit a rather wide and perfectly clean optical gap between 0.8 and 1.35 eV. Unexpectedly, the two best configurations from an energetic point of view, mSW1 and mSW2, show a narrower gap. This phenomenon appears to be directly related to the density of the cells. The modified Stillinger-Weber potential leads to a density slightly lower than that of *c*-Si, creating a small gap with a higher density of localized states on the edges. For a unique topology, density and the details of relaxation can therefore play a major role in determining the electronic properties around the gap.

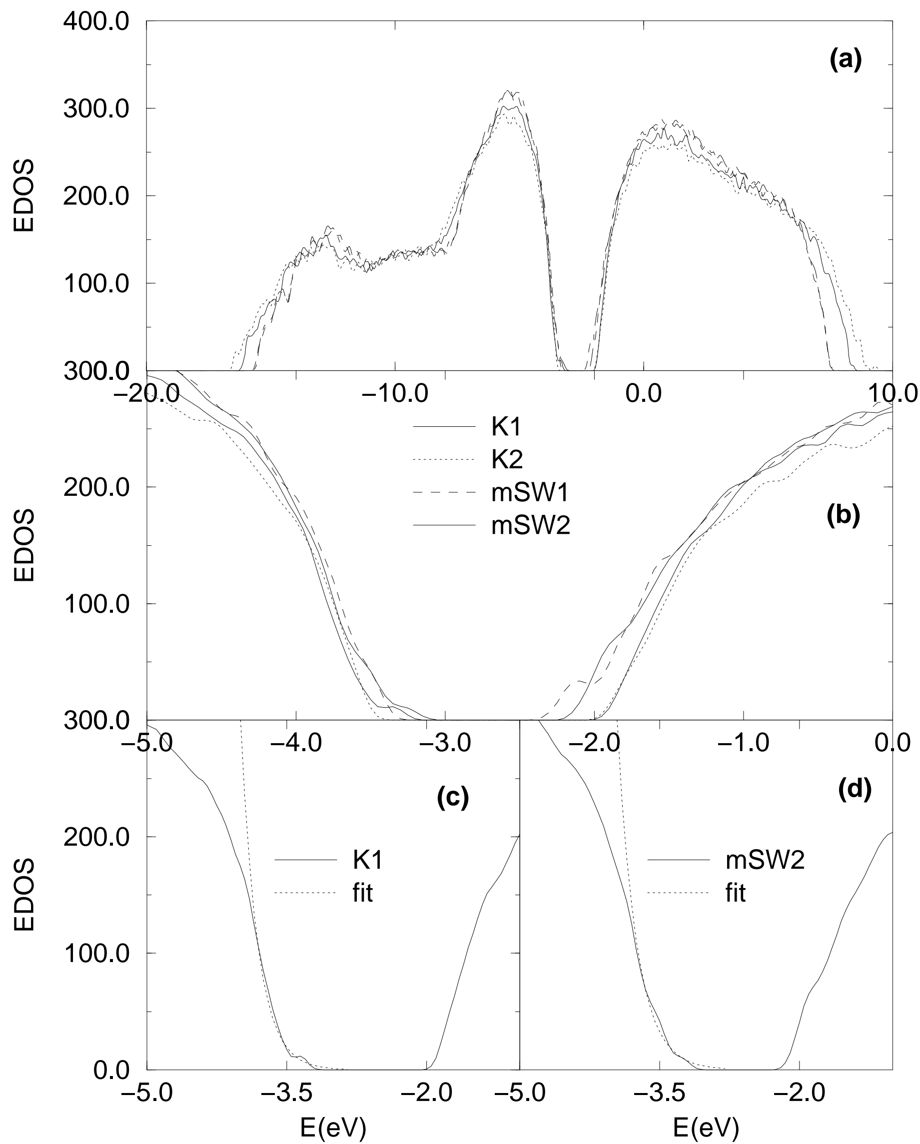

Figure 3.1: (a)Total electronic density of states (EDOS). (b) Electronic density of state in the band gap region.(c) (d) The exponential fit of K2 and mSW2 model respectively.

The rms static charge deviation of the models ranges between $0.042e - 0.051e$. These values are less than the experimental value of $0.11e$ [91] and another first principles calculation result of $0.14e$ [92]. The smaller deviations can be attributed to both ambiguity associated with the basis sets, and differences between the models analyzed. It is perhaps unsurprising that these defect-free models show less fluctuation.

The localization of the electronic states, $Q_2(E)$, defined in Equation 1, for the four models is shown in Figure 3.2. Each spike represents a single electronic eigenvalue. The larger $Q_2(E)$ for a state, the more spatially localized it is. As expected, the more localized states are on the edge of the band, where mixing is minimum. They extend within a range of about 0.3 to 0.6 eV on each side of the gap into the valence and conduction tail. Depending on the model, the $Q_2(E)$ peaks between 0.012 N and 0.064 N. These values of localization are small compare to Bethe lattice calculations which show a $Q_2(E)$ of up to 0.70 N [93]. Nevertheless, all these states cannot be considered totally delocalized.

Comparing with previous work [78], we would say that a $Q_2(E)$ greater than tenth or so of N is localized. Using this definition, we would say that K1, SW1 and SW2 show some degree of localization in either the valence or the conduction bands or both. The exact reason for the nature of the localization is not clear at the moment. Surprisingly, there is essentially no trace of localization in the EDOS of K2. Based on the width of the optical gap, this result was to be expected. However, K2 is also the most energetic of the four configurations considered. Localized states could therefore help reduce the overall configurational energy of a structure

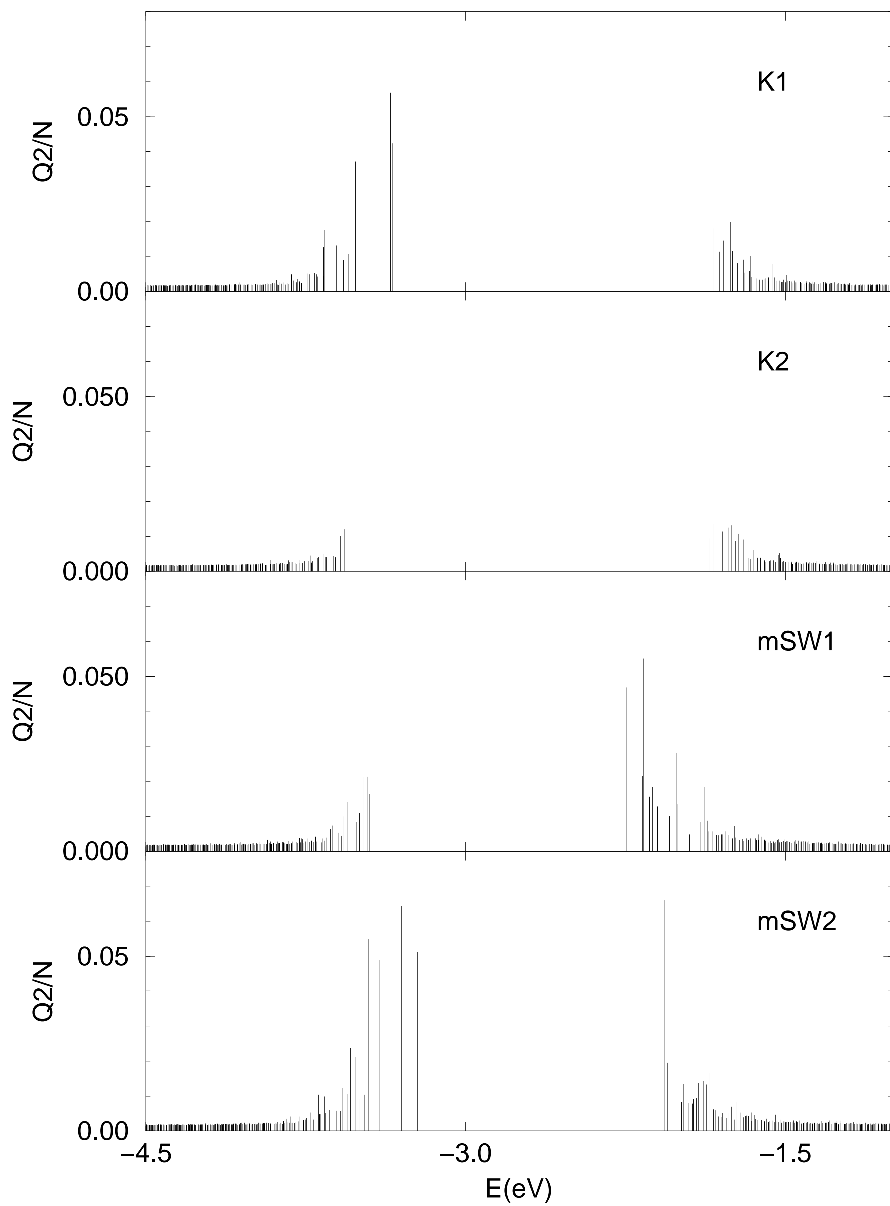

Figure 3.2: Electronic eigenstates in the band gap region. The position of vertical bars represents the eigenvalues of the electronic eigenstates and height of the bars is the spatial localization.

by concentrating the strain on a few atoms only. This remarkable result also raises an important question: *Can* a-*Si exist with no localized state whatsoever?* Although we lack experimental and theoretical support, based on the current work, we believe that it is possible to generate a model of *a*-Si with no coordination defect, a narrow bond-angle distribution and absolutely no localized state representing the *ideal a*-Si model.

To examine the spatial structure of an electronic eigenstate, we visualize the states in two steps:(i) the electron charge associated with each atom site is calculated for a given electronic eigenstate, (ii) each atom is then drawn in one of the four levels of the gray scale according to amount of charge associated with it. Very dark atoms are strongly localized sites that contribute more than 10% of total charge each, less dark atoms are sites that contribute more than 5%, light atoms are sites that contribute more than 1% each and white atoms contribute the rest in Figure 3.3. For clarity, the atoms which contribute the least charge for the given eigenstates are omitted in the figure.

The localization four chosen valence states is given in Table 3.3. The states evolve from a localized (midgap) state to an extended valence state. We visualize these chosen valence states for SW2 in Figure 3.3. The reason for selecting this model is that SW2 shows more localization than the others. The charge is confined to a cluster or clusters of atoms near to a recognizable structural distortion (small band angle deviation or stretched bonds) as in the midgap states as shown in the upper left panel of Figure 3.3. The clusters have extended 1-D string-like character for certain eigenstates in the band tails. As the energy is turned from the localized states

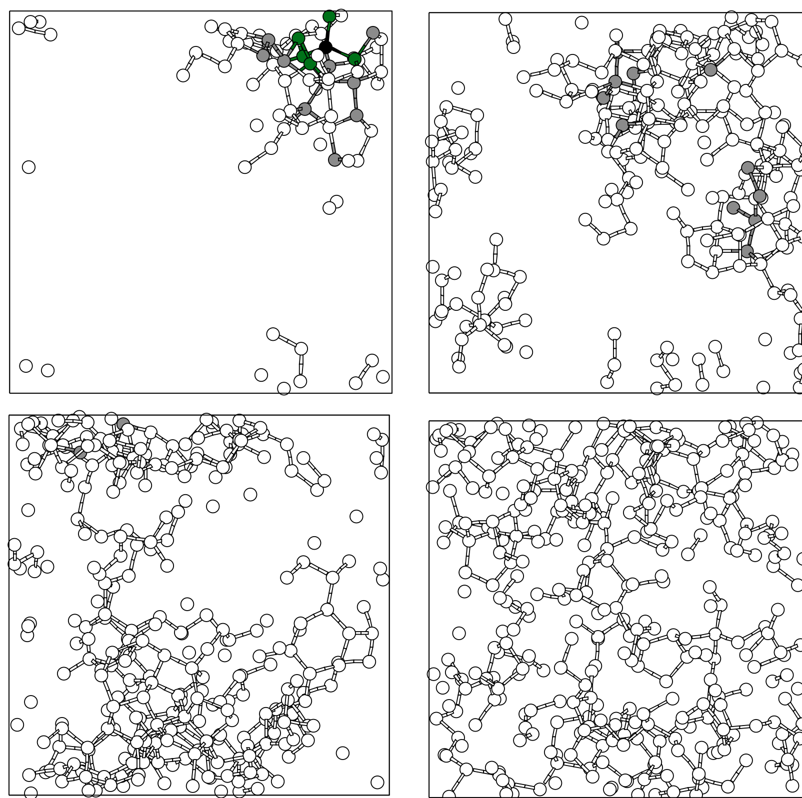

Figure 3.3: Spatial character of the local-to-extended transition in mSW1. For a given eigenstates, the electron charge density depicted according to the four level gray scale. See Ref. 94 for detailed information about the figure.

Table 3.3: The measure of localization(four chosen valence states from a localized state (ls), to less extended states (lexs) and, to an extended state (exs) of the models.

Model	$Q_2(E)$(ls)	$Q_2(E)$(lexs)	$Q_2(E)$(lexs)	$Q_2(E)$(exs)
K1	0.0422N	0.00489N	0.0024N	0.0018N
K2	0.0119N	0.0028N	0.002N	0.0016N
mSW1	0.016N	0.0062N	0.0024N	0.0018N
mSW2	0.051N	0.005N	0.0027N	0.0018N

to the valence states, the cluster size increases smoothly. The meaning is that the spatial character of these eigenstates goes through a so-called Anderson [30](localized to extended) transition. Such a behavior in a-Si was recently obtained by Dong and Drabold [31], and they proposed that this phenomenon could be explained by the resonant tunneling between cluster with similar electronic energies. Although the extended states are important in deciding the optical properties of amorphous semiconductors, hopping transport mainly occurs between midgap states.

3.4 Conclusions

Electronic properties of four 1000-atom models of a-Si generated using the modified version of the WWW algorithm have been analyzed using approximate *ab initio* technique. All models exhibit a wide totally clean gap without states and exponential band tails. The models show a relatively weak localization near both the valence

and the conduction band edges. The midgap states are slightly Anderson localized and the states are extended as we move into the valence or conduction band tails. It appears that an *ideal* model of *a*-Si would show no localized state at all along with a narrow bond angle distribution and a perfectly four-fold coordination. Although the modified Stillinger-Weber potential is more realistic interaction potential which does not required pre-set list of neighbors, the results show that the Keating potential is electronically better than the modified Stillinger-Weber potential. This feature remains to be investigated.

Chapter 4

First order amorphous to amorphous phase transition of silicon

4.1 Introduction

Many questions persist about pressure-induced phase transitions in materials. An energetic experimental and theoretical effort has been directed to these questions, and much progress has been made. An exception is the case of pressure-induced phase transition in disordered materials, a case for which there is some experimental information, but very little theory. In the specific context of the classic amorphous semiconductor amorphous silicon (a-Si), we use current first principles techniques to address the following questions: 1) In a system which has native topological disorder, how does the system topology change under pressure?; 2) Is the transition first or second order?; 3) How does the insulator-metal (electronic) transition proceed in the high-pressure amorphous phase?

For the crystal, the diamond $\rightarrow$ β-Sn$\rightarrow$ *Imma* $\rightarrow$ simple hexagonal (SH)$\rightarrow$ Si(VI) $\rightarrow$ HCP transitions have been observed experimentally [95, 96, 97, 98] and successfully explained from the first principles calculations [99, 100]. Recently, molecular dynamics (MD) simulations have made it possible to observe directly the dynamical character of the solid-solid pressure-induced phase transition. Focher *et al.* [66] and Morishita *et al.* [101] performed a first principle constant pressure MD for the crystalline silicon(c-Si) using Parrinello-Rahman (PR) method [48]which enables the simulation cell to change volume and shape and found that the diamond structure of c-Si transforms into the SH phase at 30 GPa and 26 GPa respectively.

There are also some studies on high-pressure phase transformation of the silicon clathrate Si_{136}. Dong *et al.* have shown recently a transformation from Si_{136} to β-Sn at about 3-4 GPa and diamond to Si_{136} near -4 GPa using a first principle calculation [102, 103].

Where a-Si is concerned, the pressure-induced phase transition is less clearly understood than in c-Si. Although thin films of a-Si and a-Ge exhibit an amorphous to crystalline phase transition at room temperature [9, 10, 17, 18], experiments have shown that an amorphous tetrahedral structure can form in a dense structure depending on the temperature[37].

In this chapter, we present an *ab initio* constant pressure MD study of semiconductor to metal transition in c-Si and a-Si. To our knowledge, this is the first direct MD simulation to study on the pressure-induced phase transition in a-Si. c-Si initially arranged the diamond structure undergoes a first order phase transition in the SH structure at 29.5 GPa, and a-Si presents a discontinuous transition to an

amorphous metallic phase at 16.25 GPa. The obtained transformation is in excellent agreement with the experimental observation that the semiconductor-metal transition in the amorphous materials (Si and Ge) arise from structural modification which remains amorphous [9, 10]. The energy-volume calculation predicts that the transition pressure of *a*-Si is about 9 GPa which is consistent with the experimental value of 10 GPa [9, 10]. The behavior of *c*-Si and *a*-Si under pressure is quite different. In a contrast to *c*-Si, *a*-Si network suffers the gradual change of the coordination number because of its non-uniform environment. The optical gap of *c*-Si decreases gradually under pressure, whereas that of *a*-Si first increases smoothly, it then reaches a maximum and decreases with pressure. The modification of the covalent bond lengths, of the bond angles and of the coordination number under pressure is responsible for the behavior of the optical gap in *a*-Si. It is also found that the highly localized conduction tail states of *a*-Si become delocalized with increase of pressure.

4.2 Computational technique

The simulations reported here are carried out in a 216-atom model of *c*-Si and *a*-Si. The *a*-Si is due to Djordjevic *et al.* and is in uniform agreement with structural, vibrational and optical measurement [104]. At zero-pressure, the amorphous cell is equilibrated and relaxed with a local orbital first principles quantum MD method, FIREBALL96 [84], designed for application to large complex system. The method employs density functional theory within the local density approximation and hard norm-conserving pseudopotentials. The method is implemented entirely real space.

The short-range nonorthogonal single-ζ (1s+3p per site) local orbital basis of compact slightly excited *fireball* orbitals of Sankey and Niklewski offers an accurate description of the chemistry with a significant computational advantage [52], ideal for the complex system. This method has been successfully applied in c-Si including high pressure phases [52], expanded volume phases of silicon ("zeolites without oxygen")[105], silicon clusters [106, 107], a-Si [78, 108] and in a wide range of other amorphous systems, a-GaN [85], a-C [86], and $GeSe_2$ [76, 109]. Slow dynamical quenching starting at 800 K under constant pressure is performed to fully relax the systems to zero-temperature. The number of steps required to optimize the structures depends on the pressure, and near the transition required about 10,000 time steps. The number of steps was selected to ensure that the system was completely relaxed (according to the criterion that the maximum force was smaller in magnitude than 0.01 eV/Å. Naturally, more steps were required near the transition when dramatic structural rearrangements were observed. All the calculations used solely the Γ point to sample the Brillouin zone, which is reasonable for a cubic cell with 216 atoms. A fictitious cell mass of 6×10^3 amu was found to be suitable for these simulations.

With a candidate high pressure phase in hand, the transition pressure can be calculated from the well-known thermodynamics theorem that the phase transformation occurs when the Gibbs free energy

$$G = E_{tot} + PV - TS \tag{4.1}$$

becomes equal between the two phases.

In order to characterize the localization of electronic states through the transition, we define the Mulliken charge [87],$Q(n, E)$, for atom n associated with the eigenvalue E. This charge can then be used as a measure of the localization (Inverse Participation Ratio) of a given state

$$Q_2(E) = N \sum_{n=1}^{N} Q(n, E)^2 \tag{4.2}$$

where N is the number of atoms in a supercell. For a uniformly extended state,$Q_2(E)$ is 1, while it is N for a state perfectly localized on a single atom.

Like all calculations of the type we report here, there are limitations associated with the size of the cell, the duration of the MD run, and approximations in the Hamiltonian employed. Probably the most serious limitation is the accessible time of the MD run (and implicitly an imperfect sampling of possible conformations). It is never possible to completely rule out "missing a phase" in the kind of simulation reported here, though we think that it is very unlikely to be relevant here because of the consistency of our work with experiments and comparisons of our high pressure simulations on c-Si, and other published work on c-Si. The cell size for this paper is large by the standards of *ab initio* MD, and adequate to induce only small biasing from size artifacts. The Hamiltonian we use has been extensively tested on a wide variety of Si systems and consistently does very well, despite a minimal basis.

4.3 Results and Discussions

4.3.1 Structural Properties of *c*-Si Under Pressure

As a preliminary, we repeated the high pressure computations of others for c-Si. We find that the diamond structure remains essentially intact until about 17 GPa with a small bond angle distortion. After the system is fully relaxed, we study structural relaxation as a function of pressure. At 29.5 GPa a dramatic structural change is observed: the diamond structure transforms to SH in agreement with the previous constant pressure MD calculations [66, 101]. However, the SH structure contains defects. The structural properties of *c*-Si under pressure is summarized in Table 4.1. The average bond length increases to 2.479Å which is close to the experimental result of $a = 2.463$ Å for a SH structure at 36 GPa [110] but, less than $a = 2.667$ Å and $c = 2.547$ Å for a perfect SH at equilibrium volume [111]. It is found that the normalized volume to measured zero-pressure volume ($V^{SH}/V^{diamond}$)is 0.62 which is slightly lower than the previous first principle calculations 0.672-0.69 [100].

4.3.2 Structural properties of *a*-Si under pressure

For a more reliable estimate of the transition pressure, we first plot the pressure-volume curve in Figure 4.1. The volume changes smoothly up to 16.25 GPa. At this pressure, an abrupt decline of the volume is seen indicating a first-order pressure-induced phase transition. The behavior of the normalized volume is in excellent agreement with the experiment, but the meta-stable transition pressure is higher than the experimental value of 10 GPa[9, 10] . In order to obtain an equilibrium

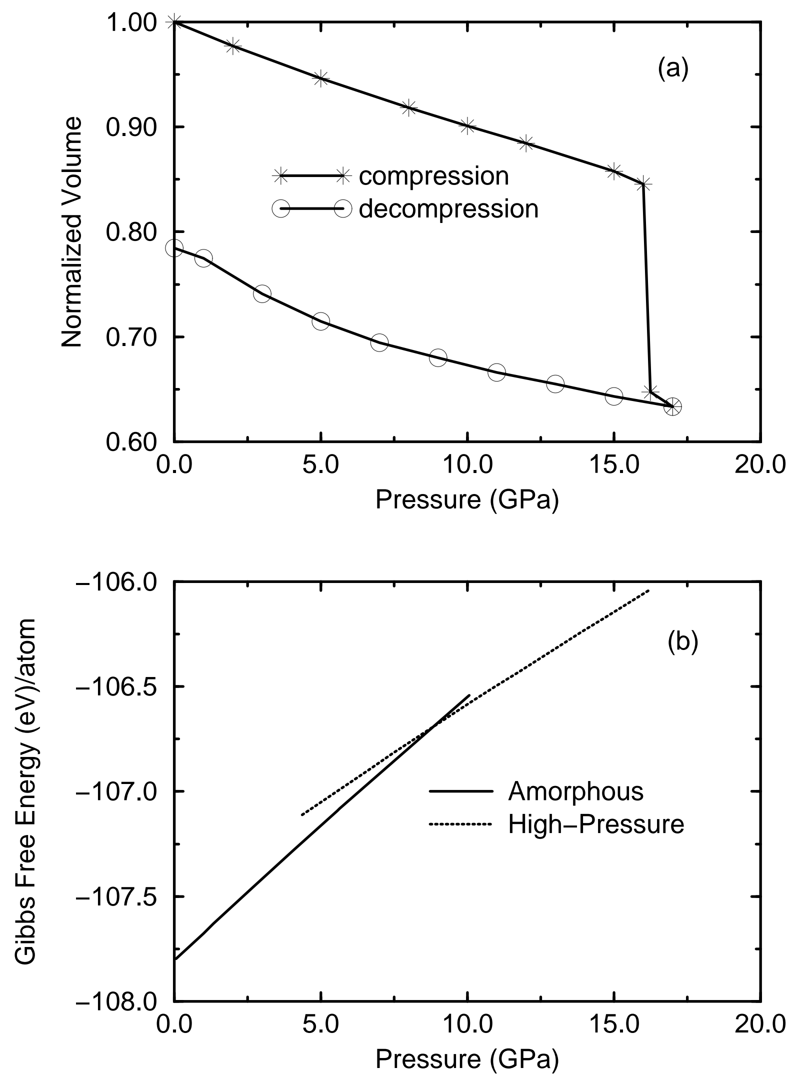

Figure 4.1: (a) The normalized volume of a-Si to the zero-pressure measured volume. At 16.25 GPa, the volume drops suddenly, indicating pressure-induced phase transition. (b) Gibbs free energy of amorphous and high pressure phase cross near 9GPa implying a transition.

Table 4.1: Structural properties of c-Si under pressure: average bond length (ABL), average bond angle (ABA), bond angle distribution (BAD), and average coordination number (ACN).

Pressure (GPa)	0	10	15	17	29.5
ABL (Å)	2.377	2.319	2.289	2.227	2.479
ABA	109.48°	109.47°	109.4°	109.4°	100.6°
BAD	0.018	0.033	2.24	2.72	34.49
ACN	4.0	4.0	4.0	4.0	8

critical transition pressure we calculate the Gibbs free energy of amorphous phase and the high pressure phase at zero-temperature. The Gibbs free energy curves (Figure 4.1) cross at about 9 GPa, indicating a transition, which is in good agreement with the experimental result of 10 GPa [9, 10]. The large value of the metastable (Parrinello-Rahman) transition pressure implies an intrinsic activation barrier for transforming one solid phase into another since the barrier should overcome in a global transformation [59, 60, 66]. The thermodynamic theorem, however, does not take into account the possible existence of such an activation barrier separating the two structural phases. The thermodynamic theorem gives that the density of the high pressure phase at transition is 3.2 g/cm^3 which is less than 3.42 g/cm^3 predicted from the MD. This implies that the cell is superpressured because of the activation energy, well above the transition pressure where two structure coexist, in analogy to isobaric superheating in MD simulations [60]. The pressure-volume curves from slow

pressure release at 17 GPa is given in Figure 4.1. The followed path is not reversed because of the strain-induced disappearance of the local minima of the potential energy surface [7]. Similar irreversible transitions have been observed in *a*-Ge [17], SiO_2[7, 112], GeO_2 [6] and H_2O [1] which shows a first order phase change from the low-density amorphous (LDA) to a high-density amorphous (HDA). The density difference between HDA and LDA phase of H_2O is almost 25%. The obtained phase from the slow pressure release is 27% denser than the amorphous phase. It also is found that the fast pressure release from 16.25 to 0 GPa and 17 to 0 GPa gives about 21.6% and 22.7% more dense structure. Nevertheless the decompression started from different final pressures gives a very similar structure albeit with small difference in density and coordination. In Figure 4.2, we illustrate the zero-pressure amorphous phase and metallic amorphous phase.

The pressure dependence of the total energy per atom of *a*-Si is given in Figure 4.3. The energy increases non-linearly with pressure. The energy of *a*-Si branch and the energy of the high pressure phase branch are separated by a gap which gives the energy barrier of transformation for the system. The energy gap between two branches is found to be about 0.25 eV.

The pair distribution function is given in Figure 4.4. The peak positions shifts to shorter distances, indicating tighter packing of the network, with pressure up to 16.25 GPa. The intensity of the peaks changes slightly until the transition pressure at which a huge coordination change is observed. At the transition pressure the intensity of the first peak drops suddenly with broad distribution and its position shifts into a larger distance, reflecting a much higher ($\approx$ 8-9 fold) coordination.

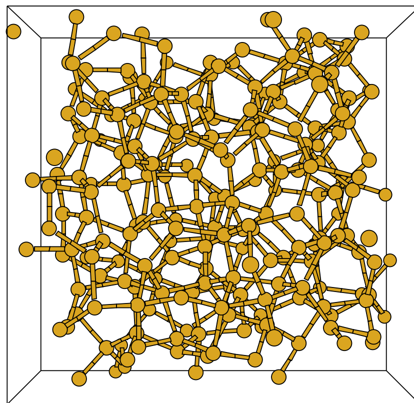

(a) Amorphous silicon at zero-pressure.

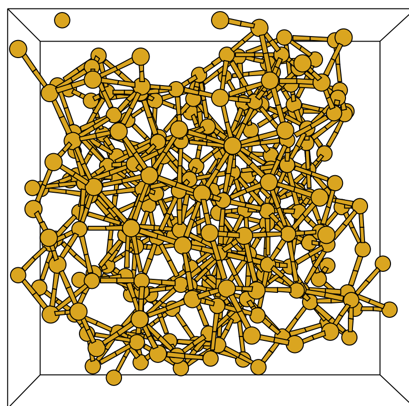

(b) The obtained high pressure phase at 16.25 GPa.

Figure 4.2: (a) *a*-Si model at zero-pressure (b) The disordered high pressure phase at 16.25 GPa.

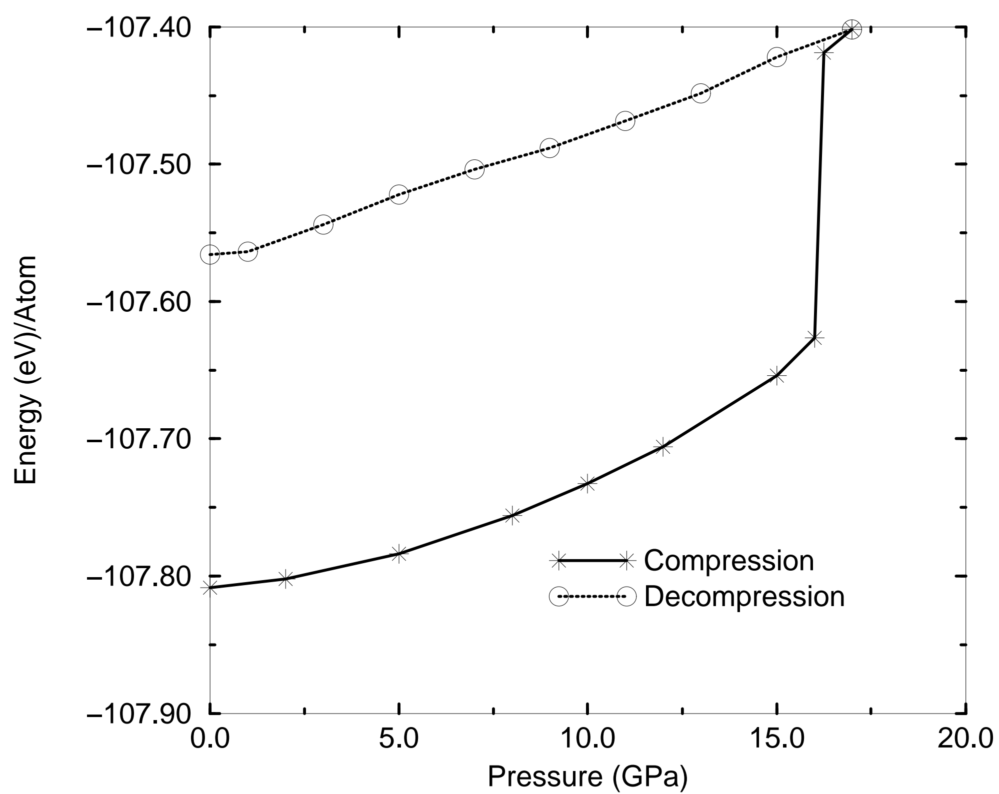

Figure 4.3: The pressure dependence of the total energy per atom for a-Si and the high pressure phase.

The intensity of the second peak exhibits a sharp decrease and shifts to a shorter distance. The result is consistent with x-ray diffraction of SiO_2 glass at high pressure, which reveals an increase of the first neighbor and a decrease of the second neighbor separation [5]. It is of interest to compare the pair distribution function of the zero-pressure phase from the slow pressure release with that of *a*-Si. The peaks shift to larger distances. The nearest-neighbor peak is narrowed, with slight decrease of the intensity. The dramatic changes are seen in the second and third shell: both show broad distribution with increase in the second shell intensity and decrease in the third shell intensity.

The bond angle distribution function of *a*-Si is given in Figure 4.4. The perfectly coordinated model at 0 GPa shows a smooth distribution with a single peak centered at the tetrahedral angle. The function exhibits several peaks under pressure as a result of the increase of the coordination. At 16.25 GPa, the function is rather broad with main peaks around 60°, 90° and 150°. Car-Parrinello (CP)[113] and Fabricius *et al.* in their respective *ab initio* MD [114] simulation report that the bond angle distribution function of liquid-Silicon (*l*-Si) has a prominent peak around 60° followed by a broad distribution with a single maximum containing a bump at near 150°. Although the general shape of both bond angle distribution functions is similar, there are two main differences between them: the bond angle distribution function of the our model induces a small peak near 150° rather than a shoulder and the intensity at 60° is rather larger because of the higher coordination. On the decompression we notice that the intensity at 60° and 90° present drastic change: the intensity at 60° decreases while that at 90° increases.

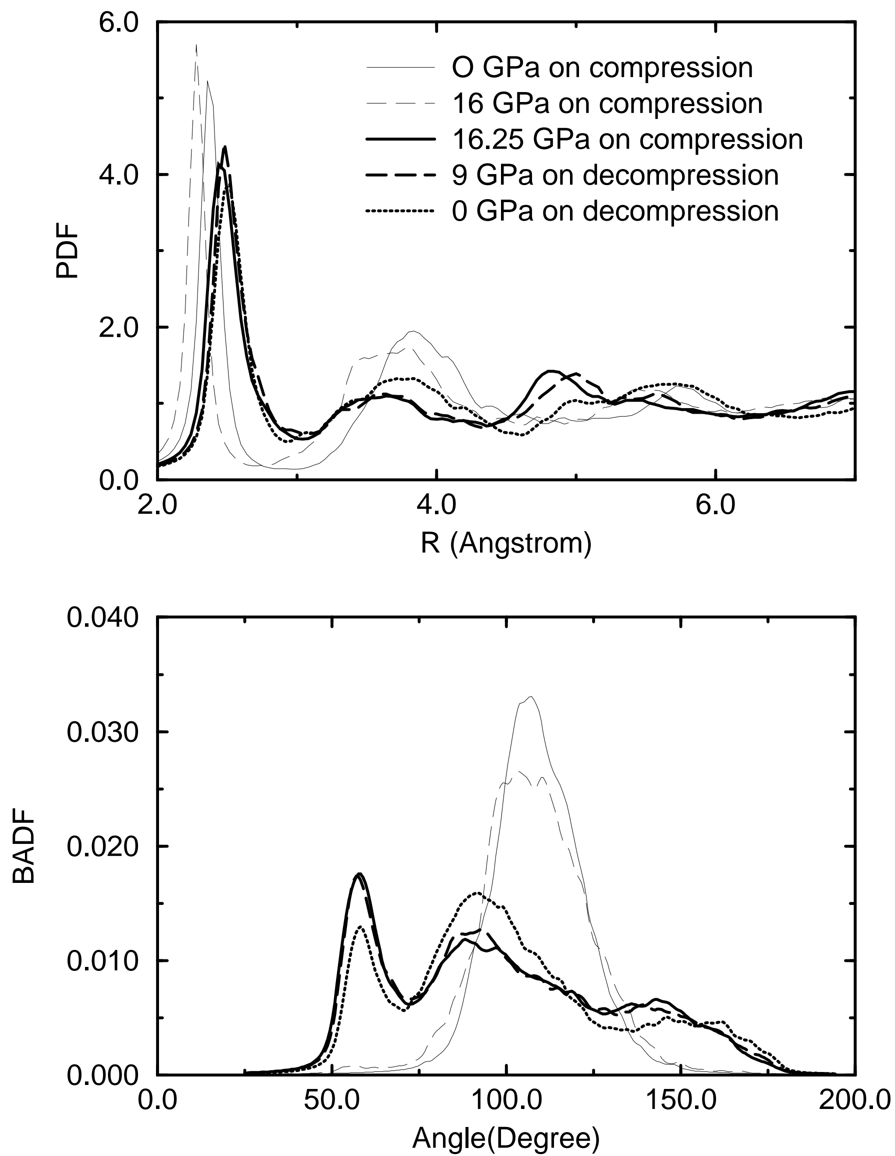

Figure 4.4: (a) The behavior of the pair distribution function (PDF) of and (b) The bond angle distribution function (BADF) of a-Si on compression and slow decompression.

Table 4.2: Structural properties of a-Si under pressure. Same nomenclature as Table 4.1

Pressure (GPa)	0	8	16	16.25	17
ABL (Å)	2.386	2.328	2.290	2.540	2.560
ABA	109.17°	108.93°	108.3°	98.23°	97.88°
BAD	11.1	12.1	14.2	32.9	33.0
ACN	4.0	4.0	4.1	8.6	9.2

Table 4.2 presents the structural properties of a-Si model under pressure. The initial compression causes the narrowing of tetrahedral angles, shortened bond lengths and small increased coordination. At 16.25 GPa, the average bond angle drops to 98.23° which is intermediate between the tetrahedral and octahedral values of 109.5° and 90° respectively. The average coordination from the pair distribution function (R_c = 3.02 Å) for the high pressure phase of a-Si is 8.6, which is larger than the experimental value of 6.4 [162] and CP simulation result of 6.5 [113] for l-Si. This is unsurprising since the density of the high pressure phase (3.42 g/cm^3) is larger than that of l-Si (2.59 g/cm^3) [113]. The structural properties of the zero-pressure phases on decompression are given in Table 4.3. The densified phases at zero-pressure present a small fluctuation in the average bond angle and average bond length, but $\sim 27 - 30\%$ decrease in the average coordination number.

The behavior of c-Si and a-Si network under pressure is rather different. In contrast to c-Si, a-Si network presents some local modification, gradual increase of the coordination. In spite of the small local modification, the transformation occurs

Table 4.3: Structural properties of the obtained zero-pressure phases on decompression. Same nomenclature as Table 4.1

Pressure (GPa)	17 to 0	16.25 to 0	17 to 0 Slowly
ABL (Å)	2.55	2.54	2.55
ABA	100.9°	101.6°	100.9°
BAD	30.9	30.4	31.2
ACN	5.98	5.72	6.25

globally in *a*-Si as it is observed in *c*-Si. In *a*-Si, we find that the increase of the coordination occurs first in the vicinity of defects with large bond angle deviations. The highly stressed part of the model has a tendency to transform to a more closed packed geometry under pressure since the angle distortions provide paths for the increases of the coordination.

The energies of the optimized structures at several volumes fit the Birch-Murnaghan equation of states [116]. The obtained bulk modulus of *c*-Si, 97.56 GPa, is consistent with the experimental value of 98 GPa. We find that the bulk modulus of *a*-Si, 82.5 GPa, is less than that of *c*-Si as expected. The calculated bulk modulus of the high pressure phase of *a*-Si, 77.15 GPa, is smaller than that of *a*-Si. The softening of the bulk modulus in the high pressure phase of *a*-Si can not be explained as a free-volume effect and it is due to the high coordination, which leads to additional restrictions to the bulk relaxation in the distorted networks [117].

4.3.3 The Pressure Dependence of Band Gap Energy

Atomistic simulation also allows us to directly study the electronic nature of the pressure-induced insulator-metal transition. It is found that both conduction and valence tail states shift into higher energies at low pressure range in *a*-Si. The shift of the conduction tail states is larger than the valence tail states, implying an increase of the optical gap. Under higher pressure, the conduction tail states move to lower energies while the valence tail states continue to shift to higher energies, yielding a decrease of the band gap energy. In *c*-Si network, the bonding and anti-bonding energy separation decreases with increase of overlap from pressure. Simultaneously the conduction and valence band both broaden. As the interatomic distances are decreased, the degree of overlap between the atomic orbitals on adjacent atoms increases. The greater number of overlapping orbitals causes a broadening of bands and a decrease in the band gap. The change to metallic structure takes place in a gradual way.

In tetrahedral materials, the effect of the pressure on optical absorption edges is small and pressure derivatives of the energy are nearly zero [17, 118, 119, 120]. These characteristics are ascribed to rigid there dimensional bonding structure. In amorphous tetrahedral materials including *a*-Si, the optical gap increases and the refraxtive index decreases with pressure (0-1GPa) [118]. The pressure coefficient of the fundamental absorption in *a*-Si is positive, +0.25 meV/kbar [118], whereas it is negative in *c*-Si, -1.5 meV/kbar[118] and in *a*-Si:H, -1meV/kbar [120, 121]. Figure 4.5 shows the pressure dependence of the optical gap in *c*-Si and *a*-Si. The gap of *c*-Si decreases smoothly with pressure. We find the pressure derivative of the gap for *c*-Si

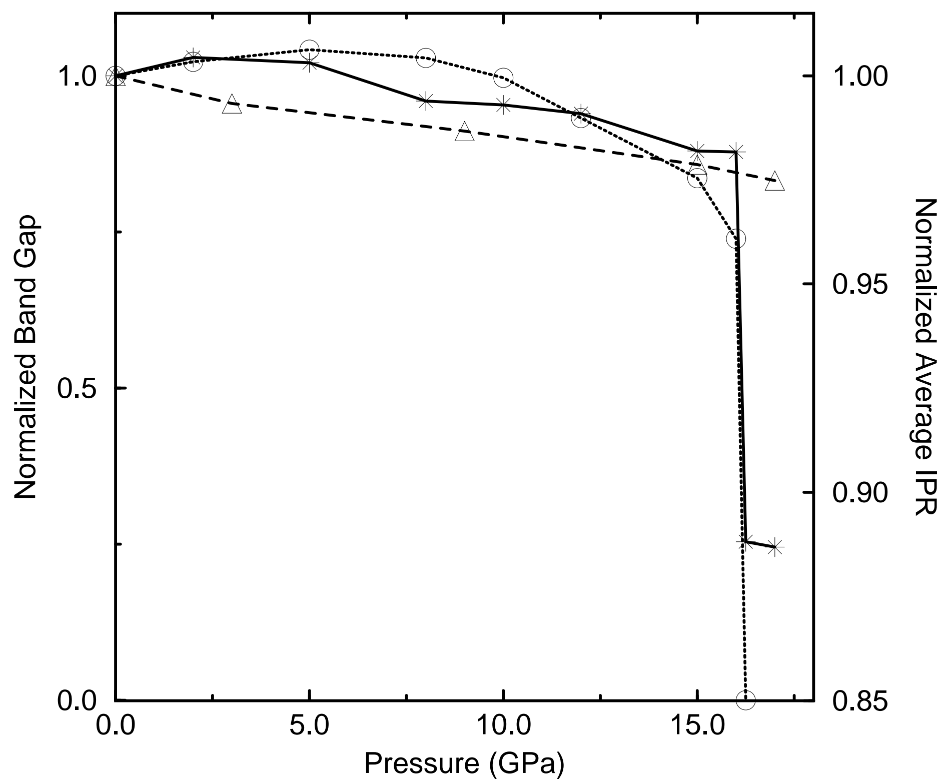

Figure 4.5: Pressure dependence of the normalized optical gap to zero-pressure optical gap for *c*-Si (dashed line with triangle) for *a*-Si (dotted line with circle) and the normalized average Inverse Participation Ratio (solid line with star).

is -1.73 meV/kbar in the pressure range 0-17 GPa. This value is the same in the sign, but slightly different in magnitude what is reported in Ref. [118]. The gap behavior of the optical gap width in *a*-Si under pressure is non-linear. For low pressures, it increases gradually and reaches a maximum at 5 GPa. Under further compression, the gap decreases because of structural change.

4.3.4 Localized states in *a*-Si and response to pressure

The measure of the localization of the states is shown in Figure 4.6. Each spike on the figure represents an energy eigenvalue. The larger $Q_2(E)$ for a state, the more spatially localized it is. As expected, the states near midgap are quite localized at zero-pressure. The states are very non-local away from the midgap since the states in the band tails are extended. The localization of the conduction tail states shows a gradual decrease with increase of the pressure up to 16.25 GPa, implying the pressure-induced delocalization of the states. The pressure dependence of average Inverse Participation Ratio is given in Figure 4.5 At 16.25 GPa, all states are completely extended. The tiny gap in Figure 4.6 (at 16.25 GPa) is a finite size and single-ζ (minimal basis) artifacts: the material is certainly conducting.

4.3.5 Vibrational density of states

It is valuable to predict the phonon modes for *a*-Si, the high pressure phase and *c*-Si. The physical origin of the phase transition can be understood by examining the pressure sensitive soft phonon modes. The vibrational density of states (VDOS) is given in Figure 4.7. With increase of pressure in*c*-Si, the acoustic modes are

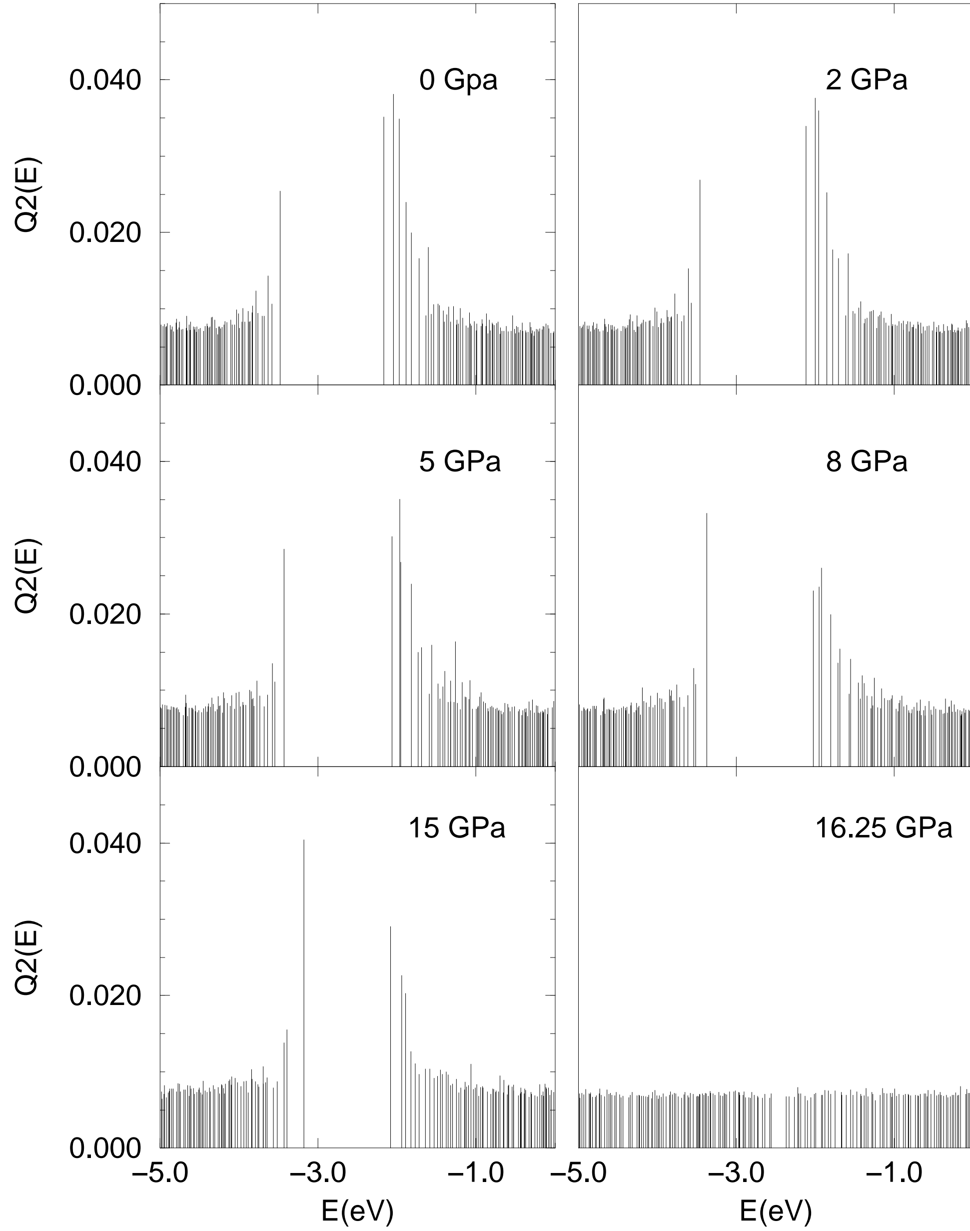

Figure 4.6: Electronic eigenstates in the band gap region. The position of vertical bars represents the eigenvalues of the electronic eigenstates and height of the bars is the spatial localization ($Q_2(E)$). The Fermi level lies in the middle of the band gap. Note the abrupt delocalization of tail states at 16.25 GPa.

softened, while optical modes shift to higher energy. The results are consistent with Raman scattering [122]. We notice large decrease of the energy of the optical band and a small increase of the energy of the acoustical band in *a*-Si. This can be in principle be compared indirectly to Raman measurement.

4.4 Conclusions

We have studied the pressure-induced phase transition in *c*-Si and *a*-Si with *ab initio* constant pressure MD technique. *a*-Si undergoes a first order phase transition into an amorphous metallic phase while *c*-Si transforms into the SH structure at 29.5 GPa. The obtained amorphous to amorphous phase transition is irreversible. The behavior of *a*-Si network under pressure is rather different from that of *c*-Si because of its environment. The defects in *a*-Si behave as nucleation centers for pressure-induced change. It is found that the localized conduction tail states are extended with pressure.

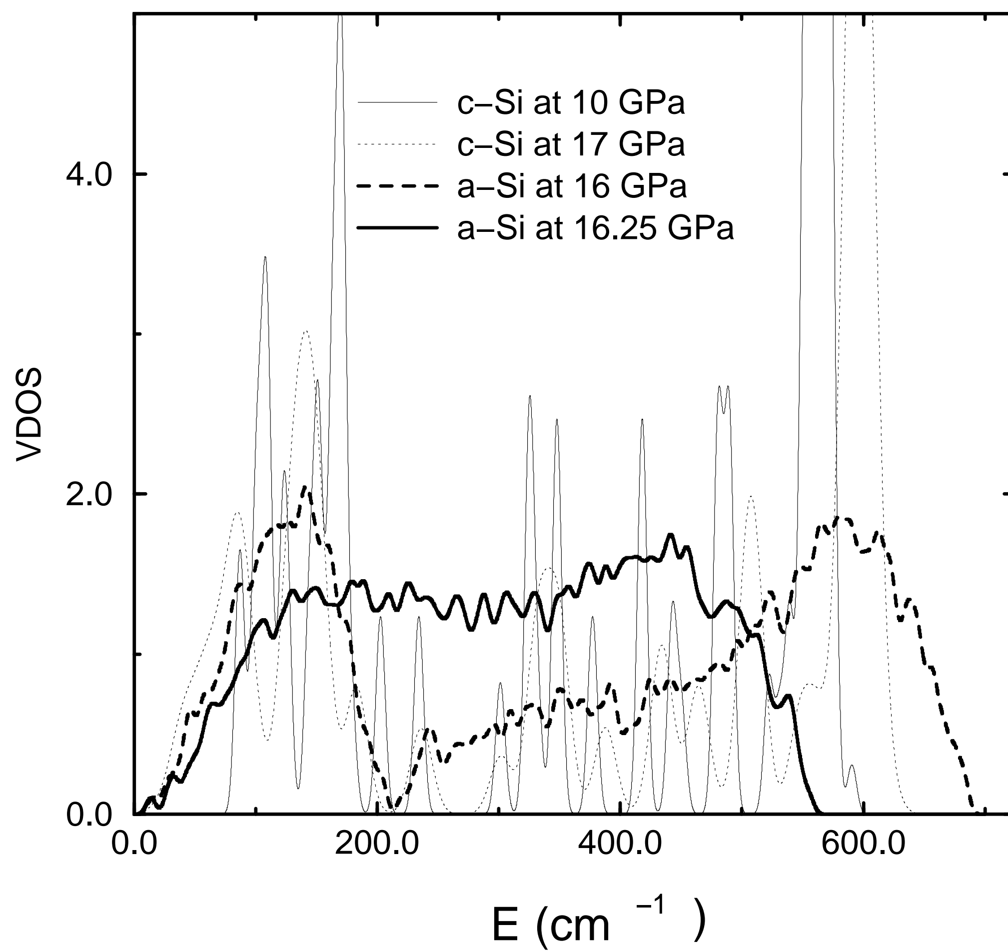

Figure 4.7: Vibrational DOS of a-Si at 16 GPa and the high pressure phase at 16.25 GPa and c-Si at 10 GPa and 17 GPa.

Chapter 5

A theoretical investigation of amorphization and crystallization in silicon phases

5.1 Introduction

Pressure-induced phase transitions have long been studied for ordered (crystalline) materials. A considerable understanding of the physics of these transformations has been obtained[123]. Where amorphous materials are concerned, the situation is far less clear. Only in the last few years has the concept of polyamorphism (the possibility of many distinct amorphous conformations for a given material) been considered [124, 125]. In analogy with pressure-induced polymorphism in crystals, we consider the effects of pressure on the structure of amorphous Si. We also discuss amorphization of crystalline Si, and an amorphous to crystalline (β-Sn) transformation.

Experiments [9] have reported that *a*-Si and *a*-Ge transform to an amorphous metallic phase with a sharp drop in the resistivity and optical gap around 10 GPa and 6 GPa respectively, and it appears that these transitions are first order. An amorphous to crystal phase transition in *a*-Si and *a*-Ge has been observed in other experiments [17, 19]. In porous silicon [11], a transition from the diamond phase to a High Density Amorphous (HDA) phase is reported while nanocrystalline silicon [126] undergoes a direct transition from diamond to a simple hexagonal structure. In both porous and nanocrystalline silicon, the samples transform to a low density amorphous structure upon decompression.

Current computational methods have successfully *predicted* high pressure phases of materials using total energy calculations with the thermodynamic criterion of equal free energies. One such prediction was a kinetically hindered first order amorphous to amorphous phase transition in SiO_2 [7]. Recently an experiment confirmed such a first order amorphous to amorphous phase transition[8]. Such calculations obviously require candidate structures which may be obtained from constant pressure simulations and sometimes experiments.

In earlier work, we found that *a*-Si exhibited a first order phase change from a low density amorphous phase to a high density amorphous (HDA) metallic phase using a constant pressure relaxation technique [127]. Kelires [61] confirmed an amorphous to amorphous phase transition in *a*-Si and *a*-Ge using Tersoff and EDIP potential. Although he finds that the transition in both structures proceeds gradually, the free energy calculation indicated a first order transition in *a*-Si at 9.8 (7.8) GPa for Tersoff (EDIP) potential[61].

In this chapter, we investigate the pressure-induced phase transitions in *a*-Si and in diamond silicon (*c*-Si) using *ab initio* calculations. We find that *c*-Si undergoes a first order phase transition into β-Sn structure at 9 GPa in agreement with theoretical and experimental studies. An amorphous to β-Sn transformation occurs at 2.5 GPa. Furthermore an amorphous to amorphous phase transition is predicted at 9 GPa consistent with experimental result of 10 GPa [9] . We also find that pressure-induced amorphization of crystalline diamond silicon near 15 GPa, i.e., a first order phase change from the crystalline diamond to the HDA phase consistent with a recent experiment of porous silicon[11].

5.2 Methodology

We use a local orbital first principles quantum molecular dynamics method of Sankey and Niklewski [52], designed for application to large complex systems. The essential approximations are (1) nonlocal, norm-conserving pseudopotentials, (2) slightly excited local-orbital basis set of four orbitals per site, and (3) the Harris functional implementation of the local density approximation. This method has been successfully applied in a wide variety of silicon systems; *c*-Si including high pressure phases [52], expanded volume phases of silicon ("zeolites without oxygen")[105], and *a*-Si [78, 108]. The Parrinello-Rahman method [48] used conjection with this *ab initio* technique successfully predicts a first order amorphous to amorphous phase transition in silicon [127], high pressure phases of *c*-Si [127], and a continuous amorphous to amorphous phase change in $GeSe_2$ [128].

We employ a starting model of a-Si due to Djordjevic *et al.* which is in uniform agreement with structural, vibrational and optical measurements [104]. The high pressure phase is determined from starting with Djordjevic *et al.* model and using the method of the preceding paragraph. All the calculations used solely the Γ point to sample the Brillouin zone, which is reasonable for cells with 216 atoms.

5.3 Results and Discussion

Diamond, β-Sn, a-Si and HDA phase are optimized for several volumes and fit to the Birch-Murnaghan equation of state [116]. We report the minimum structural energy per atom E_{min} and corresponding atomic volume V_{min} for each structure in Table 5.1. The relative total energy difference per atom between β-Sn and diamond structure $\Delta E_{min}(= E_{min}^{\beta-Sn} - E_{min}^{diamond})$ is 0.289 eV/atom, which is consistent with 0.27 eV/atom [129]. It is found that the ratio of the equilibrium volume of β-Sn to diamond $V_{min}^{r}(= V_{min}^{\beta-Sn}/V_{min}^{diamond})$ is 0.74, which is close to 0.77 [129]. Nevertheless we find agreement of the approximate method with accurate self-consistent calculations.

In a-Si, the energy difference $\Delta E_{min}(= E_{min}^{amorphous} - E_{min}^{diamond})$ is 0.199 eV/atom in good agreement with a nonorthogonal tight-binding model [88]. However, the difference is a factor of two higher than an experimental result 0.0977 eV, as extrapolated to 0 K from the measurement at 960 K using the specific heat listed in that work [89]. The density of a-Si is slightly less than the crystal density in agreement with experiment.

Table 5.1: The minimum energies E_{min}, the relative energy difference $\Delta E (= E^i - E^{diamond})$, the corresponding minimum volume per atom V_{min} and its ratio $V^r_{min} = V^i_{min}/V^{diamond}_{min}$, where i is diamond, β-Sn, a-Si and HDA phase.

Structure	diamond	β-Sn	a-Si	HDA
E_{min}(eV/atom)	-108.006	-107.717	-107.807	-107.53
ΔE_{min} (eV/atom)	0	0.289	0.199	0.476
V_{min}(Å^3/atom)	20.76	15.42	21.26	15.87
V^r_{min}	1.0	0.74	1.02	0.76

The calculated Gibbs free energy ($G = E_{tot} + PV$) at zero-temperature for diamond, β-Sn, a-Si and the HDA structure is shown in Figure 5.1. The transition pressure between diamond and β-Sn phase is found to be 9 GPa, which is consistent with the result of 9.5-15.4 GPa reported in previous experiment and theoretical studies [111]. The transition volume of diamond $V_t(diamond)$ and β-Sn $V_t(\beta\text{-Sn})$ is 0.924 and 0.684 (Figure 5.2) respectively and $V_t(diamond)$ value is in good agreement with experiment and theoretical results of 0.89-0.928 whereas the transition volume of β-Sn is less than 0.70-0.719 [111].

Gibbs free energy calculations predict a first order phase transition between a-Si and β-Sn phase around 2.5 GPa. The critical pressure in this transition is about one quarter of the diamond to β-Sn transformation. The transition volume $V_t(amorphous)$ is 0.96 while $V_t(\beta\text{-Sn})$ is 0.70 (relative to zero-pressure a-Si volume). The transition volume of β-Sn is 0.72 when it is normalized to the zero-pressure

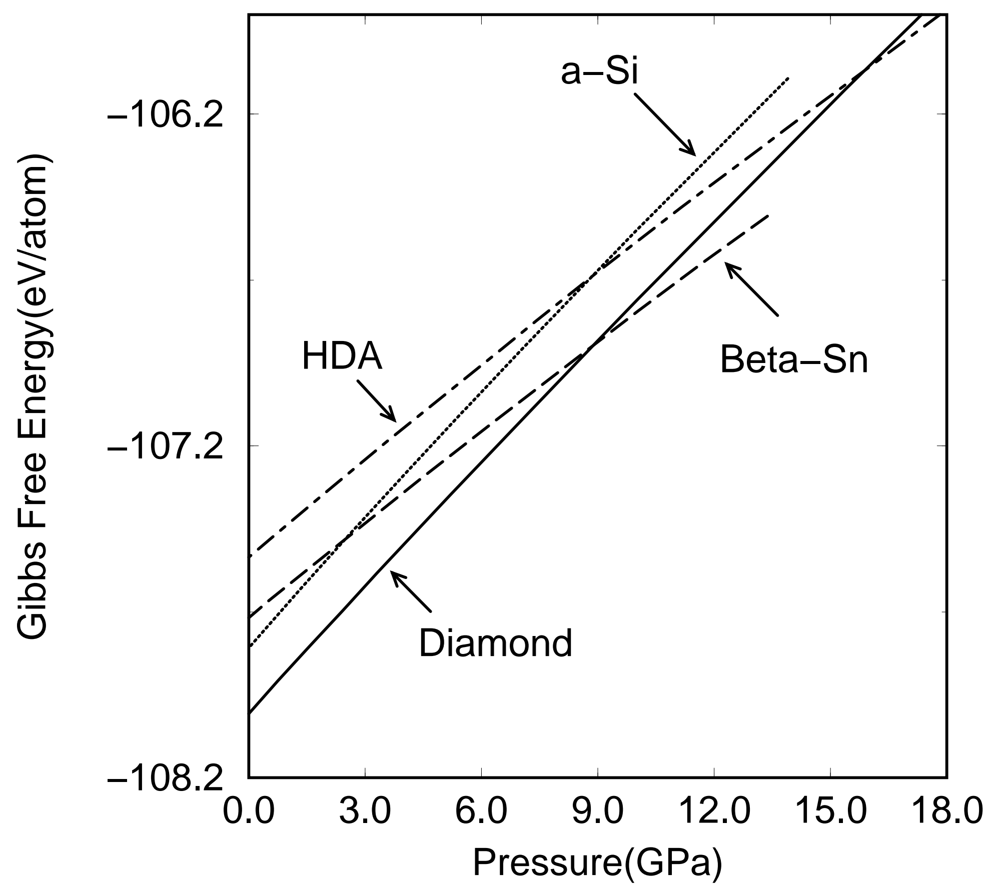

Figure 5.1: The calculated Gibbs free energy for diamond, β-Sn, a-Si and the HDA phase.

volume of diamond. This is a bit larger than 0.684 obtained in the diamond to β-Sn transition.

Even though the transition obtained between a-Si and β-Sn agrees with the experiment, the predicted crystallization pressure (2.5 GPa) is much less than 8 GPa, which is probably due to the initial amorphous structure, i.e., the model's properties. We mentioned that the relative energy difference between a-Si and c-Si ($\Delta E_{min} = E_{min}^{amorphous} - E_{min}^{diamond}$) is larger than the experimental value. When the slope of the common tangent line is considered in energy volume curve, an amorphous network with a small energy difference at the same minimum volume will yields an increase of the slope and so the transition pressure. We find that an amorphous model with ΔE_{min}=0.174 eV/atom and V_{min}^{r}=21.03 Å^3/atom leads to a 1.0 GPa increase of the crystallization pressure. However, further investigation is required to clear this issue using several models with different size and structures (containing void, crystalline grain etc.).

There is no easy pathway between a-Si and β-Sn structure, and the crystallization requires bond breaking (considering ring formation) and a large number of displacements of some atoms in a contrast to diamond to β-Sn transition. These structural rearrangements need to more thermal activation. We believe that the crystallization of a-Si was kinetically hindered in earlier experiments [9, 10] and constant pressure simulations [61, 127] and hence a-Si persists until it reached a metasatbility limit in which it transformed to a HDA phase. Above room temperature the crystallization can be achievable.

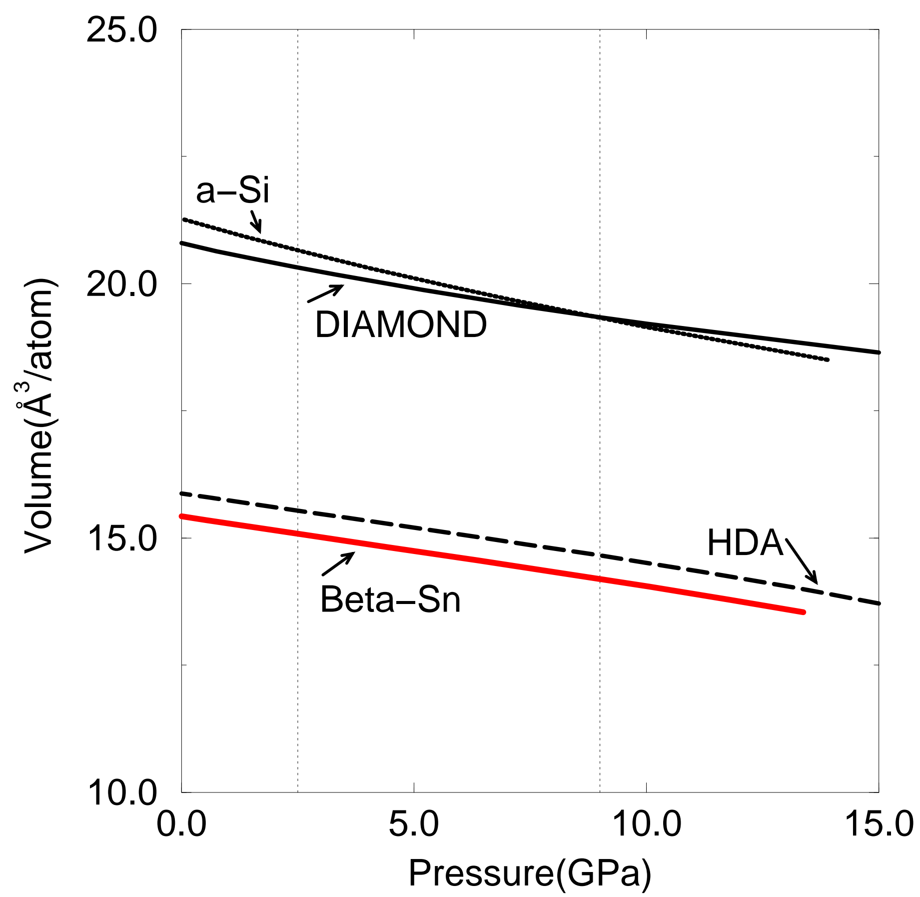

Figure 5.2: The pressure dependence of the volume per atom.

The constant pressure relaxation simulations and the Gibbs free energy calculations show that a-Si undergoes a first order phase transition from a low density amorphous phase to a HDA phase. The predicted transition pressure using the Gibbs free energy calculations is 9 GPa, which is in agreement with the experimental result of 10 GPa [9, 10] and theoretical result of 9.8(7.8) GPa[61]. We find $V_t(amorphous)$ and V_t(HDA) are 0.90 and 0.68 relative to the zero-pressure a-Si.

Another observation of interest is that there is no phase transition between β-Sn and the HDA phase but, a phase transition between crystalline diamond silicon and the HDA phase at 15 GPa, which may indicate a pressure-induced high density amorphization of crystalline diamond silicon. In this phase transformation we find that the transition volume of $V_t(diamond)$ and V_t(HDA) is 0.89 and 0.65 relative to the zero-pressured diamond structure. There is no experimental evidence of pressure-induced amorphization of diamond silicon with the application of pressure. Recently Deb *et al.*[11] have shown the pressure-induced amorphization of diamond silicon 15-16 GPa in porous silicon. That is, the crystalline portion of the porous silicon transforms to a HDA phase upon compression which is attributed to the sample properties and transformation mechanisms to the high-density phases. In addition, the extrapolated negative melting slope in the temperature-pressure diagrams of diamond silicon (see Fig.3 of Ref.[11]) yields a pressure-induced amorphization near 14 GPa at 300 K. On the pressure release, it is shown that this HDA phase transforms to a low density amorphous phase [11]. Both transitions reported in this experiment[11] confirm the predicted transition in the present study.

One puzzle of this field is the experimental observation that elemental tetrahedral materials like Si and Ge undergo *first order* phase transitions, whereas binary materials like $GeSe_2$ exhibit a continuous transition. We have observed these effects in our simulations

5.4 Conclusions

We have studied pressure-induced phase transitions in c-Si and a-Si using an *ab initio* technique. c-Si transforms from diamond structure to β-Sn structure at 9 GPa in agreement with experiments. We find that pressure-induced crystallization of a-Si at 2.5 GPa and argue that the crystallization pressure strongly depends on structural properties. At 9 GPa, a-Si undergoes a first order phase transition from a low density amorphous phase to a HDA phase. A pressure-induced amorphization of crystalline diamond silicon is predicted near 15 GPa.

Chapter 6

Ab initio simulation of pressure-induced low-energy excitations in amorphous silicon

6.1 Introduction

Extensive experimental and theoretical investigations have made considerable progress toward understanding the nature of vibrational dynamics of amorphous silicon (a-Si) [130, 131, 132, 133, 134, 135, 136, 137, 138, 139, 140, 141]. However, the changes in the vibrational spectrum of a-Si with external perturbations need to be explored. An investigation of a-Si under pressure is, therefore, important to understand not only changes in the vibrational spectrum but also the structure of a-Si.

a-Si can be prepared in various ways, which yields structures with different physical properties. It has been reported that the vibrational spectrum of a-Si depends on degree of structural disorder, sample preparation, deposition conditions and hydrogen concentration[130, 131, 132]. The TA/TO intensity ratio and TO line-width

correlate with bond angle distribution of the sample[132, 135]. The coordination defects lead to localized states not only near the high frequency band edge, but also in the low-frequency tail [136]. There is a correlation between the density of a-Si and the number of localized states (the number of localized states decreases with increasing density of a-Si)[141]. Nakhmanson and Drabold have shown that a four-fold coordinated model of a-Si does not exhibit low-energy excitations and that the presence of voids leads to extra low energy states in the vibrational density of states (VDOS) [137] and a sharp peak in $C(T)/T^3$ [138].

Recently we showed that a-Si transformed via a first order phase transition into an amorphous metallic phase using an *ab initio* constant pressure relaxation simulation [127], which is in agreement with experiments [9, 10]. Kelires [61] confirms an amorphous-to-amorphous phase transition in a-Ge and a-Si using EDIP and Tersoff potential. Kelires finds that the transition in both structures proceeds gradually and the free-energy calculation suggests a first-order transition in a-Si [61]. Since the behavior of a-Si under pressure is known from experimental and theoretical studies, a-Si is an excellent system to further study the phonon spectrum and states under pressure. In this chapter, we present the pressure dependence of the low- and high-energy modes in a-Si using an *ab initio* constant pressure relaxation simulation and lattice-dynamical calculation. We find that pressure softens the low-energy modes and leads to a dramatic decrease in the acoustic-like nature of these frequencies. The higher frequency modes shift to larger energies up to the transition pressure at which point the mode frequencies decrease abruptly. The pressure-induced delocalization of highly localized high frequency modes is observed with the application of pressure.

6.2 Methodology

The simulations reported here are carried out in a 216-atom model of a-Si. The a-Si model is by Djordjevic *et al.* and is in uniform agreement with structural, vibrational and optical measurements[104]. At zero-pressure, the a-Si model is relaxed with a local orbital first principles quantum dynamic method due to Sankey and Niklewski [52]. In this method, the local density approximation to density functional theory is used with a minimal basis of one s and three p pseudoatomic orbitals on each atom. These basis functions are slightly excited from their ground state and these are referred to as "fireball orbitals". The Harris functional with hard norm-conserving pseudopotentials is used. This method has been successfully applied in c-Si including high pressure phases [52], expanded volume phases of silicon ("zeolites without oxygen")[105], and a-Si [78, 108]. This Hamiltonian predicts successfully the pressure-induced phase transition in crystalline silicon (diamond to simple hexagonal) and in a-Si (amorphous to amorphous) [127]. Slow dynamical quenching starting at 800 K under constant pressure is performed to fully relax the system to zero-temperature. The number of steps required depends on pressure, and near the transition required about 10,000 force calls. Pressure is applied via the method of Parrinello and Rahman [48] which enables the simulation cell to change volume and shape.

Once the equilibrium configurations under pressure are obtained, we compute the dynamical matrix, displacing every atom in the cell in three orthogonal directions (0.03 Å) and computing the resulting spring constants as second derivatives of the

total energy of the system. Diagonalizing the dynamical matrix we receive its eigenvectors and corresponding squared normal-mode frequencies ω^2, which enable us to carry out a study of the vibrational behavior of the high pressure configurations.

As a preliminary, we perform the calculation in a crystal silicon cell and find that the acoustic phonons are softened, while the optical phonons shift to higher energies [127], which is consistent with Raman scattering experiments [122].

6.3 Results and Discussion

6.3.1 Vibrational density of states

First, we give a brief review of the structural properties of a-Si under pressure (Table 4.2). The details of the pressure-induced phase transition of a-Si is reported in chapter 4 and in Ref.[127]. The initial compression causes narrowed tetrahedral angles, shortened bond lengths and a small increase in the coordination. At 16.25 GPa, a pressure-induced phase transition occurs with abrupt volume and topological change. At the transition, the average bond angle drops to 98.23° which is intermediate between the tetrahedral and octahedral values of 109.5° and 90°, respectively. The average bond length is 2.54 Å.

The VDOS of a-Si under pressure is given in Figure 6.1. At zero-pressure a-Si shows no vibrational states present with energies below 60 cm^{-1} because of the finite size and ideal structure of the simulation cell [138]: small **k** acoustic modes are missing from our simulation which is strictly zone centered. As the applied pressure

increases, the low-energy vibrational states shift to smaller-energies. Near the transition pressure, there are negative squared eigenvalues ($\omega^2 < 0$) yielding imaginary frequencies. We have followed the method used in Ref. [142] and multiplied the imaginary frequencies by i so that they show up on the negative real frequency axis. At 14 GPa, an unstable frequency appears in the VDOS for the first time and the maximum unstable frequencies are observed at 16 GPa before the phase change. We also find that pressure pushes the frequency modes ($\omega > 200$ cm^{-1}) toward larger energies.

The behavior of modes in a-Si is very different from that of a-$GeSe_2$ [128] and SiO_2 [46], in which the bands shift to higher frequencies without softening modes. The modification of the modes in a-Si can be understood by examining the Grünesien parameter. Fabian and Allen [143] have shown that the low frequency modes of a-Si have a negative Grünesien parameter, which means that these modes soften with a decrease of volume.

6.3.2 Imaginary frequencies

In the study of coesite under pressure [44], it was reported that the mechanical instability as indicated by imaginary frequencies and group velocities occurs near the coesite-stishovite phase boundary. Binggeli *et al.* [43] have shown that the instability is associated with vanishing acoustic velocities and leads to imaginary frequencies near Γ in the quartz phonon spectrum above the critical pressure. Lacks [7] reported that the decrease of a normal mode frequency to zero implies that the dynamical matrix (Hessian) becomes nonpositive definite. This corresponds to disappearance

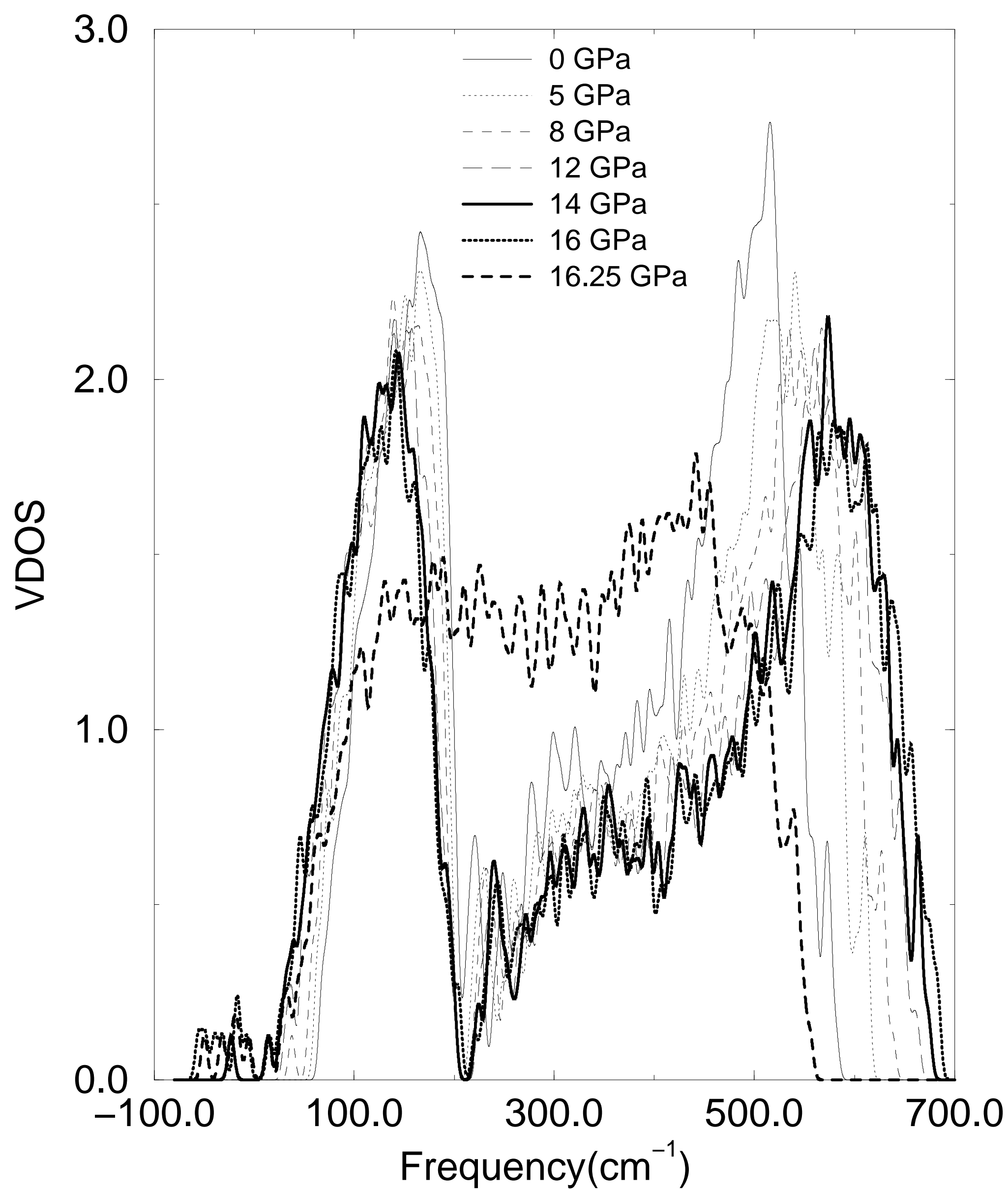

Figure 6.1: The behavior of the VDOS under pressure.

of the local energy minimum. Afterwards the system becomes mechanically unstable and relaxes at an unrelated local minimum.

The existence of imaginary frequencies near the transition pressure is an artifact of the simulations because of the short-time scale of the simulations' exploration of configurational space. These imaginary frequencies, however, can be attributed to the mechanical instability of the model system. Although they are unphysical, for the model system they serve as a harbinger of mechanical instability. As reported in the study of silica under pressure [7], the mechanical instabilities are irreversible, lead to discontinuous structural change and are localized to small groups of atoms with different groups of atoms becoming unstable at different pressures. Also it is argued that pressure-induced amorphization and amorphous-to-amorphous transitions arise from the phonon softening and mechanical instability [45] which is consistent with the results obtained in the present study. However, further investigations are required to clarify these issues.

6.3.3 Phase quotient

In a crystal, vibrations can be explained with acoustic and optic phonons. In acoustic modes, neighboring atoms move in phase while in optic modes the motion is out of phase. In amorphous materials, the atomic vibrations cannot be characterized with a definite wave vector and a division of atomic vibration into acoustic and optic phonons is not possible in general [144]. However, some characteristics can be calculated for vibrational modes in amorphous materials. One of the useful quantities is phase quotient. The phase relationship between vibrations of neighboring atoms

can be explained with the phase quotient PQ [140]:

$$PQ(\omega_n) = \frac{\sum_m \mathbf{u}_n^i \cdot \mathbf{u}_n^j}{\sum_m | \mathbf{u}_n^i \cdot \mathbf{u}_n^j|} \tag{6.1}$$

where atoms i and j constitute the mth bond, $\mathbf{u}_n^i$ is the displacement of atom i from its equilibrium position when it vibrates in mode n, and the summation is over all nearest-neighbor bonds in the cluster. In terms of values of the phase quotient, it is possible to talk about acoustic-like and optic-like modes in amorphous materials. In acoustic-like modes, the motion of atoms i and j is roughly in phase and the PQ is close to +1, and in optic-like phonons, the relative motion of atoms is roughly antiparallel for each pair and the PQ is around -1,

The pressure dependence of the PQ is depicted in Figure 6.2. At zero-pressure the vibrations with $\omega < 200$ cm^{-1} are acoustic-like while the high frequency spectral tail states have an optic-like character. The general features of the PQ at zero-pressure are in agreement with a previous report [140]. With the application of pressure, the PQ exhibits a dramatic change at low-energy: the PQ tends to decrease under pressure, indicating a decrease in the acoustic-like nature of these eigenmodes. After the network undergoes a phase transition, the PQ at the low-energy part declines dramatically (PQ $\sim$ 0.5), implying that a high coordination of the structure yields an increase of the optic-like nature of the low-energy modes.

6.3.4 Stretching character

The stretching character $S(\omega)$ can be given by

$$S(\omega_n) = \frac{\sum_m |(\mathbf{u}_n^i - \mathbf{u}_n^j) \cdot \hat{\mathbf{r}}^m|}{\sum_m | \mathbf{u}_n^i - \mathbf{u}_n^j|} \tag{6.2}$$

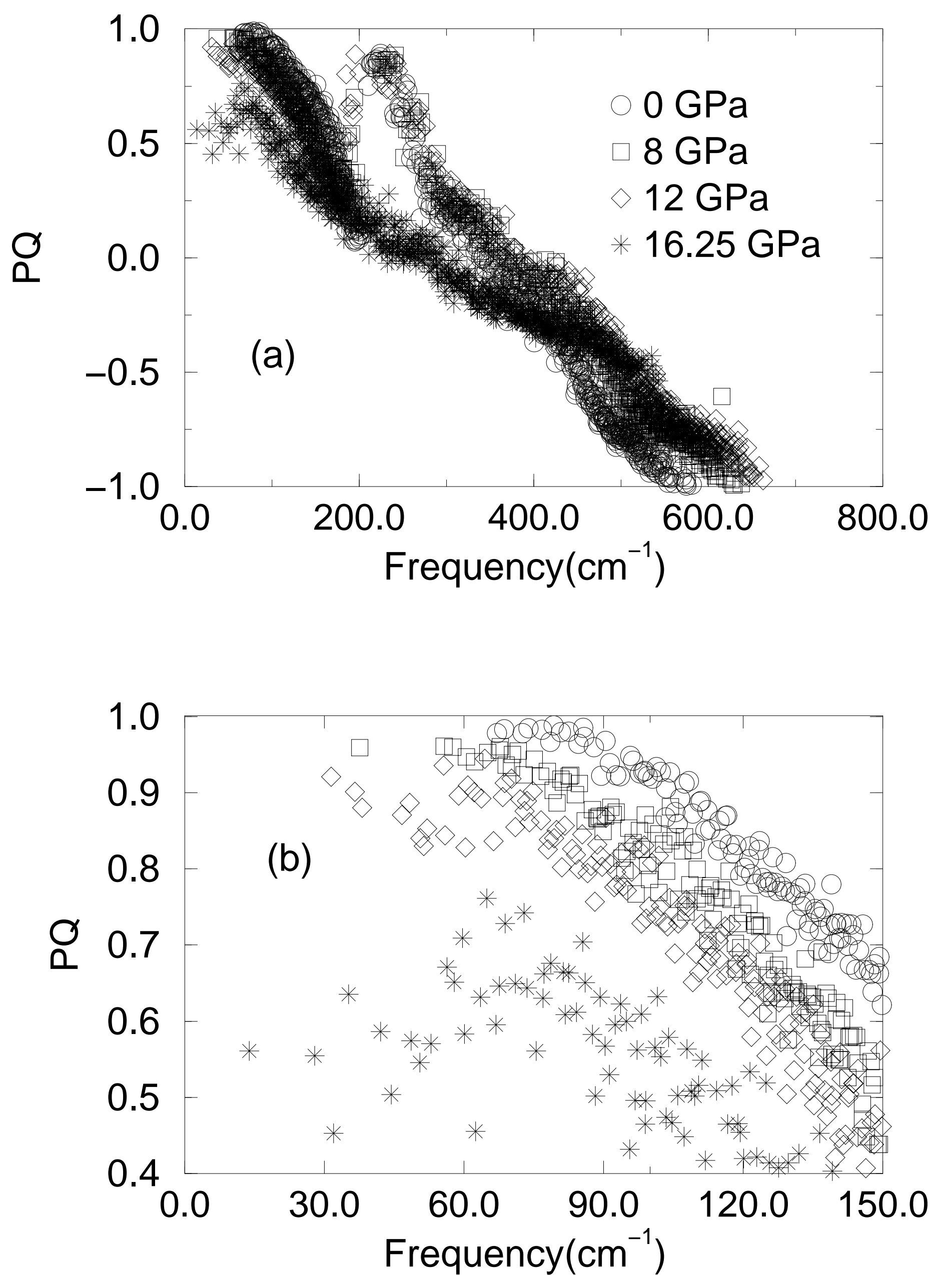

Figure 6.2: The phase quotient. The PQ is close to +1 for acoustic-like modes and it is around -1 for optic-like modes.

where $\mathbf{r}^m$ is a unit vector parallel to the mth bond (see Ref. [140]). $S(\omega)$ is close to unity if the mode n is predominantly of a bond stretching character and close to 0 if the n mode is a bond bending type.

The pressure dependence of $S(\omega)$ is given in Figure 6.3. The modes less than 200 cm^{-1} have a bond bending character while the phonons above 200 cm^{-1} have a bond stretching character. As pressure increases a small change of $S(\omega)$ is seen up to the transition pressure. At transition $S(\omega)$ shows very dramatic modification ($\omega < 400$ cm^{-1}) and all modes have bond stretching character.

6.3.5 Localized states and response to pressure

The usual measure of the degree of localization of vibrational modes is the inverse participation ratio (IPR) P^{-1},

$$P^{-1}(\omega_n) = N\sum_{j=1}^{N}(\mathbf{u}_n^j.\mathbf{u}_n^j)^2\Big[\sum_{j=1}^{N}(\mathbf{u}_n^j.\mathbf{u}_n^j)\Big]^{-2} \tag{6.3}$$

where N is the number of atoms in the supercell and $\mathbf{u}_j$ is the displacement of atom j from its equilibrium position. The IPR will have a value of ~ 1 for an extended mode where all atoms contribute equally and a value of $1/N$ for a mode defined by only one atom. In Figure 6.4 we have the IPR of a-Si under pressure. In the figure each peak represents a single eigenmode. The larger the IPR for a state, the more it is spatially localized. At zero-pressure all states except those at highest frequency are extended. The localized spectral tail states are extended with increasing pressure and they move into higher frequencies up to the transition pressure. At this pressure the states shift in the lower frequencies because of the abrupt structural change of the network. The delocalization of high-energy states under pressure has been reported

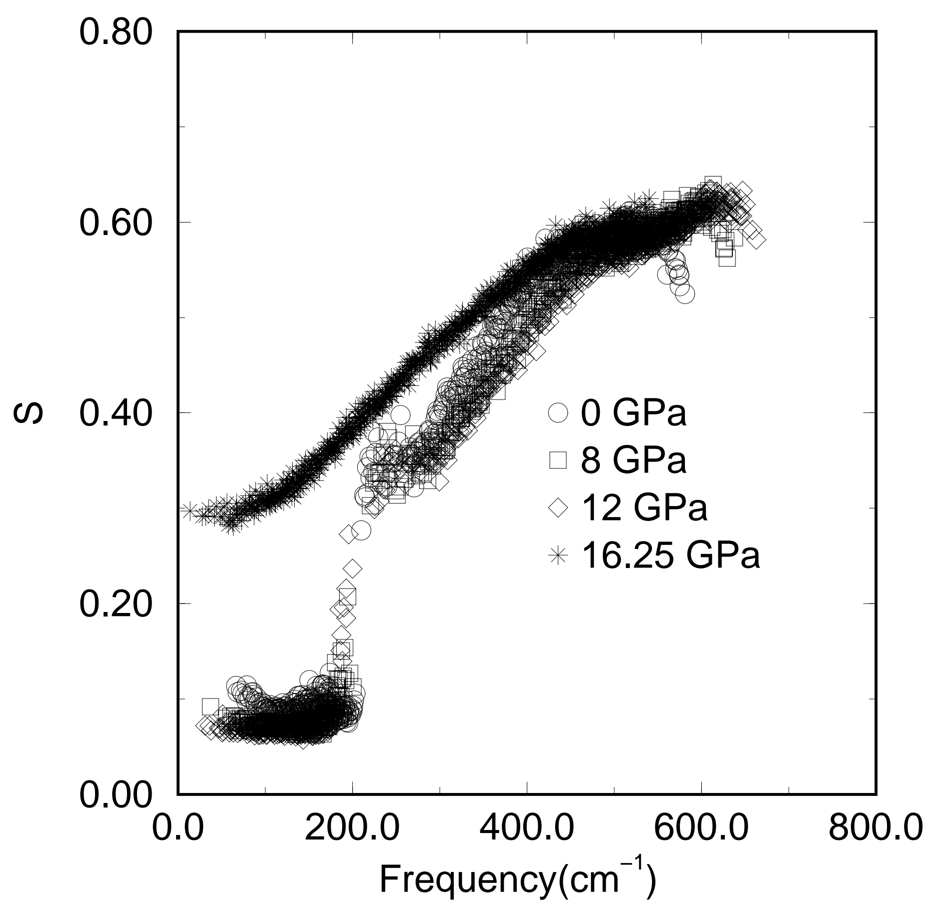

Figure 6.3: Stretching character of the vibrational modes.

in SiO_2 [46] and a-$GeSe_2$ [128].

On the other hand, the low-frequency modes shift to smaller energies and a few of the states have a high IPR at 14 and 15 GPa. The eigenmodes at low-frequencies, except for the first eigenmode, are delocalized at transition pressure. In order to understand whether these high IPR states at 14 GPa and 15 GPa are spatially localized or delocalized we visualize the states in two steps: (i) the eigenvector associated with each atom site is calculated for a given eigenvalue, and (ii) each atom is then drawn in one of the three levels of the gray scale according to the amount of eigenvector (squared component) associated with it. Very dark atoms represent strongly localized sites that contribute more than 10% of the total excitation, less dark atoms are the sites that contribute more than 5%, and the white atoms contribute the rest in Figure 6.5. The gray scale map enables us to predict where the vibrations are localized and how they decay in space. In the figure, approximately 10-20 atoms (very dark) show strongly localized sites and they are associated with a large deviation of the bond angle from the ideal tetrahedral angle. Those atoms are involved with the mechanical instability. The excitations are rather uniformly distributed in space, indicating that these unstable modes are extended. In the study of liquid-glass transition [145], it was reported that when the delocalized unstable modes show up at high temperatures, then a continuous flow mechanism for diffusion would be possible.

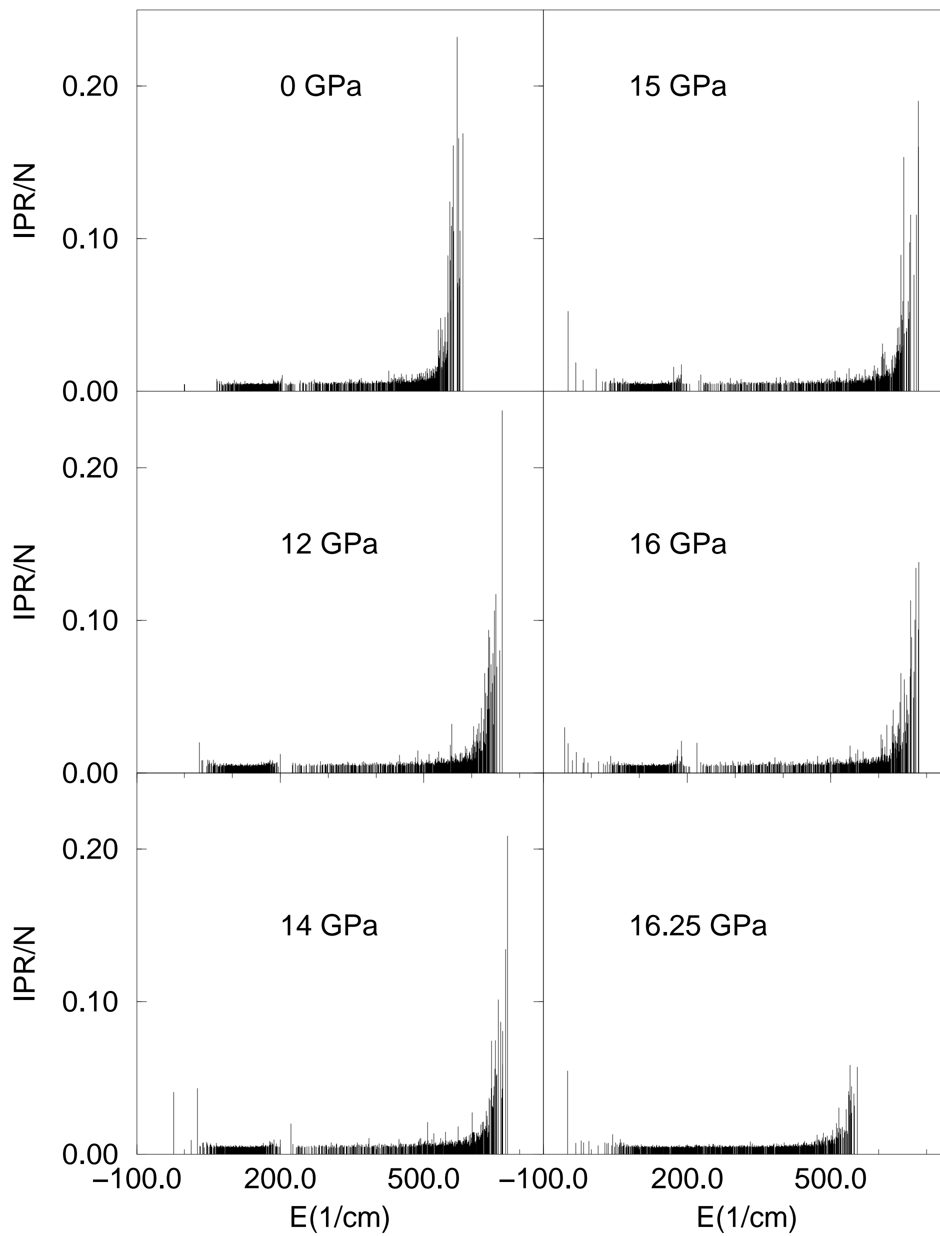

Figure 6.4: The inverse participation ratio of the a-Si modes under pressure. Note that the low-energy states are completely extended and the high-energy modes are localized at zero pressure.

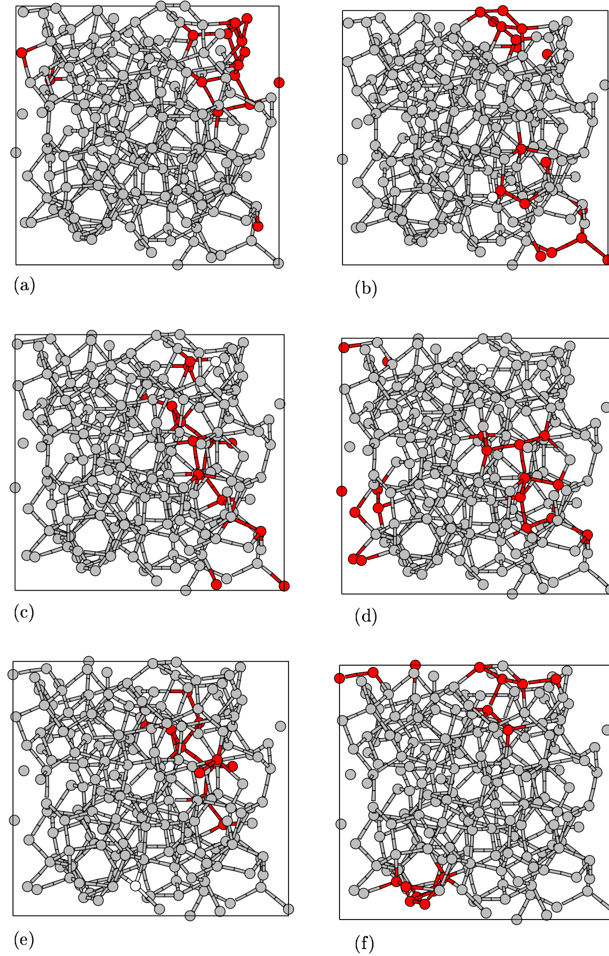

Figure 6.5: The black, gray, and white atoms correspond to $\geq 10\%$,$\geq 5\%$ and $\leq 5\%$ of the total excitation, respectively. (a) ω = 37.63 cm^{-1} at 8 GPa. (b) ω = 31.47 cm^{-1} at 12 GPa, (c) $i\omega = -23.0$ cm^{-1} at 14 GPa, (d) ω = 26.57 cm^{-1} at 14 GPa, (e) $i\omega = -49.26$ cm^{-1} at 15 GPa, and (f) $i\omega = -32.22$ cm^{-1} at 15 GPa. These modes with high IPR's at the low-energy regime are extended since the excitation is rather uniformly distributed.

6.4 Conclusions

Pressure dependence of the vibration spectrum of a-Si has been studied using an *ab initio* constant pressure relaxation simulation. Pressure leads to extra low-energy states and reduces the acoustic-like nature of these states. Up to the transition pressure, the high frequency modes shift into larger values. It is found that the localized high frequency states at zero-pressure are extended with the application of pressure.

Chapter 7

Pressure-induced structural phase transition of paracrystalline silicon

7.1 Introduction

The application of pressure to solids leads to a diverse collection of interesting phenomena. The most dramatic may be pressure-induced insulator-metal phase transitions. The pressure-induced phase transitions in crystalline silicon (c-Si) have been studied extensively. The diamond structure of c-Si transforms into a metallic β-Sn phase around 9.5-12 GPa [95, 96, 97]. Under further compression, c-Si undergoes a structural transformation from the β-Sn to an *Imma* structure at 13 GPa [98]. The *Imma* phase transforms into the simple hexagonal (SH) structure near 16 GPa [96, 97, 98]. The hexagonal closed packed (HCP) structure is observed at 42 GPa [96, 97]. In addition, a phase Si(VI) between SH and HCP is obtained at 39 GPa[96]. Recently the structure of Si(VI) was identified as orthorhombic with 16 atoms per unit cell and space group symmetry *Cmca* [146]. On release of pressure, c-Si does not transform back to the diamond structure. Instead, a metastable BC8 phase is

recovered on slow pressure release from the β-Sn [147], while two tetragonal phases are obtained from very rapid pressure release [148]. The *expanded* phase of silicon, clathrate Si_{136} with a wide gap of $\sim$ 2 eV, transforms to a β-Sn structure at 8 GPa [31].

The behavior of amorphous silicon (a-Si), porous silicon (p-Si), and nanocrystalline silicon under pressure, however, is very different from that of diamond and clathrate. Nanocrystalline silicon transformed directly to a SH structure at 22 GPa[126]. On pressure release, an *Imma*, a β-Sn and finally an amorphous phase were recovered. In p-Si, a diamond to β-Sn transformation was reported [149]. However, Deb *et al.* showed pressure-induced amorphization of diamond silicon at 15-16 GPa in a p-Si sample [11]. That is, the crystalline portion of the sample appears to transform to a high density amorphous phase upon compression, which is attributed to the sample properties and transformation mechanisms to the high-density phases.

For a-Si, contradictory high pressure data has been reported. The amorphous sample obtained using pressure-induced amorphization exhibited a sharp phase transition to a β-Sn at 8 GPa on compression [19]. We should note that samples formed by this method contain crystalline grains and have some different physical properties compared to amorphous thin films [20]. The crystallization of a-Si, however, was not seen in other investigations, and instead a high density disordered phase was obtained [9, 10, 127].

Fluctuation electron microscopy investigations have shown that as-deposited amorphous silicon thin films exhibit significant medium range order, which is interpreted as indicating the presence of small crystalline grains (< 30 Å) embedded in a disordered matrix [150, 151, 152]. The grains have topologically crystalline bonding, in which the atoms are significantly displaced from their crystalline lattice positions by strain caused by the grain boundaries. Since the grains are dilute and strongly deformed, they appear amorphous to diffraction experiments. However, the grains contribute significant medium-range order to the amorphous thin films, which is detectable by fluctuation electron microscopy. Such materials have been designated *paracrystalline* [151]. In this paper, we study the pressure-induced phase transition in a 400-atom model of paracrystalline silicon (*para*-Si) including a single crystalline grain, using an *ab initio* constant pressure-relaxation simulation. We find that the model undergoes a first order phase transition to a high density amorphous phase at 16 GPa. On the other hand, the Gibbs free energy calculation predicts a structural transformation from the *para*-Si model to a β-Sn structure at 3-4 GPa. The discontinuous metallization of the network is in agreement with experimental studies of amorphous thin films [9, 10] and computer simulation of a continuous random network model of *a*-Si [127]. It is also found that the localized electronic states at zero-pressure become extended with the application of pressure.

7.2 Methodology

The simulations reported here are carried out on a 400-atom model of *para*-Si. The *para*-Si model is generated using a generalized version of the bond-switching method of Wooten, Winer, and Weaire [74]. The model has one grain consisting of 44-atoms. It has a structure factor and electronic density of states essentially identical to continuous random network models of *a*-Si [137]. Compared to a 4000-atom model with four crystalline grains of roughly the same size (100 atoms), the 400-atom model does not reproduce the fluctuation microscopy signal, which indicates that the medium range order is not realistic. Nevertheless, the simulation does faithfully model a crystalline grain embedded in an amorphous matrix. At zero-pressure, the 400-atom model is relaxed with a local orbital first principles quantum molecular dynamics method of Sankey and Niklewski [52]. The method employs the density functional theory within the local density approximation using the Harris functional with hard norm-conserving pseudopotentials. This Hamiltonian was successfully applied in *c*-Si including high pressure phases [52], expanded volume phases of silicon ("zeolites without oxygen")[105], *a*-Si [78, 108]. The combination of this *ab initio* technique with the Parrinello and Rahman method [48] was employed to study a first order amorphous to amorphous phase change in Si[127] and Ge [128], a continuous amorphous to amorphous phase transformation in $GeSe_2$[154], ZB→*Cmcm*→*Imm2* transitions in GaAs [171], and a diamond to simple hexagonal phase transition in Si [127], and a diamond to β-Sn phase change in Ge [128]. Pressure is increased in an increment of 3 GPa up to 15 GPa, after which an increment of 0.5 GPa is carried out in order to accurately estimate the transition pressure. For each value

of the applied pressure, we fully relax the system according to the criterion that the maximum force is smaller than 0.01 eV/Å. The optimization is performed with the conjugate-gradient technique. We use Γ-point sampling for the supercell's Brillouin zone integration, which is reasonable for a 400-atom model. A fictitious cell mass of 11×10^3 amu was found to be suitable for this simulation.

7.3 Results and Discussions

7.3.1 Structural properties

The pressure volume curve of the *para*-Si model is depicted in Fig.7.1. The volume changes smoothly up to 15.5 GPa, and at which point it drops $\sim 2.5\%$. At 16 GPa, an abrupt decline of the volume is seen, indicating a first-order pressure-induced phase transition. The volume drops about 24%, which is close to the value of $\sim 21\% - 23\%$ reported in the diamond to β-Sn transformation of c-Si [99, 111]. The discontinuous metallization of the model is in agreement with the experimental result on conductivity of the amorphous thin films [9, 10] and the previous simulation of a-Si [127]. Crystallization of the model is not observed, and instead a transition from diamond to a high density amorphous phase is seen, which is recently reported in a p-Si sample with an average crystalline size of ~ 50 Å[11].

In order to determine high density nucleation centers, we visualize the model in Fig.7.2. The white atoms represent four-fold coordinated atoms whereas the black ones correspond to higher coordinated atoms (> 4). At 15 GPa, the nucleation begins in the vicinity of defects with large bond angle deviations, which enable distortions

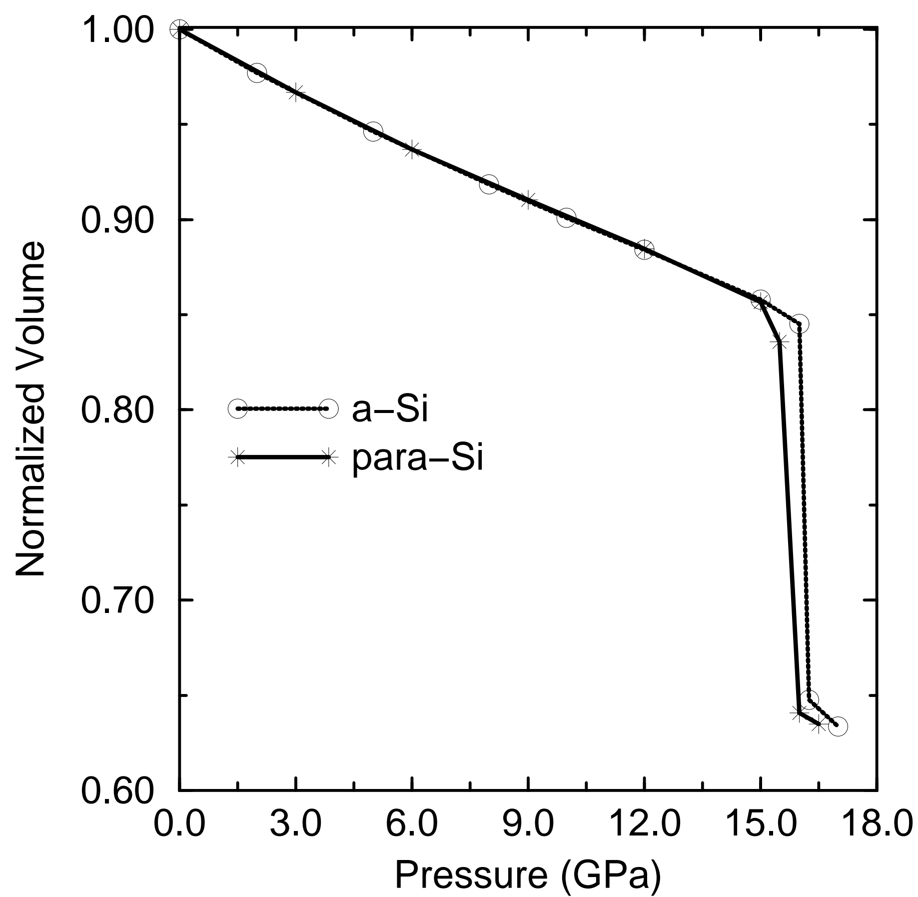

Figure 7.1: The normalized volume of *para*-Si and *a*-Si as a function of pressure.

leading to a more close packed topology. At 15.5 GPa and an intermediate step at 16 GPa, the size of the higher coordinated clusters grows. This result suggests that the transition in the *para*-Si model is not homogeneous.

Dramatic structural changes are seen at the boundary of the grain after the normalized volume reaches a value of 0.8. At this volume, $\sim 20\%$ of the disordered matrix transforms to a highly coordinated geometry but, the crystalline grain still persists in the network. Although the size of crystalline grain in the model is small, we find that the transformation of the grain begins at the interface and gradually proceeds into the core.

The real space pair distribution function g(r) is given in Fig.7.3. The peak positions shift to shorter distances, indicating tighter packing of the network, with pressure up to 16 GPa. The intensity of the peaks changes slightly until the transition pressure, at which a huge coordination change is observed. At the transition pressure, the intensity of the first peak decreases abruptly with a broadened distribution, and its position moves to a larger distance, reflecting a much higher ($\approx$ 8-9 fold) coordination. The intensity of the second peak exhibits a sharp decrease, and its position shifts toward a shorter distance.

The bond angle distribution function of the model is shown in Fig.7.4. The perfectly coordinated model up to 12 GPa shows a smooth distribution with a single peak centered at the tetrahedral angle. Above this pressure, the distribution is broadened with a significant decrease in the intensity. At 15.5 GPa, a peak appears near 60° in the distribution due to the higher coordinated topology. At the transition, the function is rather broad with main peaks around 60°, 90° and 150°. The peak

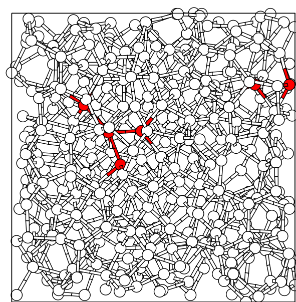
(a)

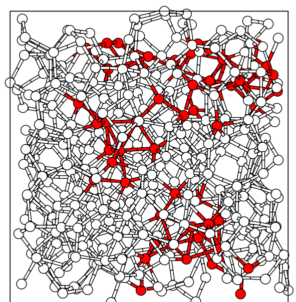
(b)

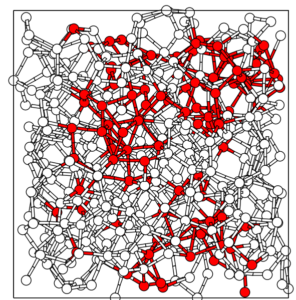
(c)

Figure 7.2: Nucleation centers define in the model at (a) 15 GPa, (b) 15.5 GPa and (c) 16 GPa (an intermediate step).

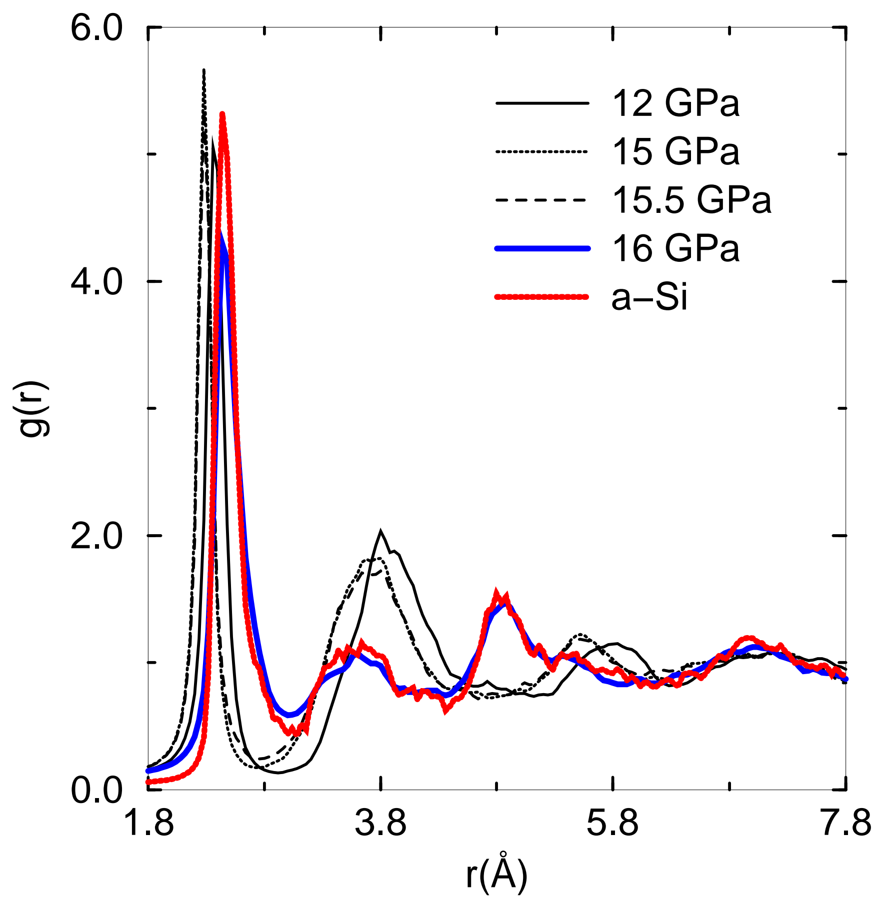

Figure 7.3: The real space pair distribution function g(r) of *para*-Si under pressure. g(r) of *a*-Si is also given at the transition pressure (16.25 GPa).

Table 7.1: Structural properties of *para*-Si under pressure: average bond length (ABL), average bond angle (ABA), width bond angle distribution (WBAD), and average coordination number (ACN).

Pressure (GPa)	0	12	15	15.5	16
ABL (Å)	2.38	2.308	2.29	2.31	2.55
ABA	109.22°	108.9°	108.69°	106.90°	98.07°
WBAD	10.47°	11.58°	12.90°	18.67°	32.97°
ACN	4.000	4.000	4.015	4.200	8.975

at 60° is a clear indication of a close packed geometry with metallic bonding.

The structural properties of the *para*-Si geometry under the application of pressure are presented in Table 7.1. The compression up to 15 GPa causes the narrowing of tetrahedral angles, and shortened bond lengths with no increase in the coordination. At the transition, the average coordination from the first minimum of g(r) within a critical cutoff radius $r_c = 3.02$Å is found to be 8.9 and quite sensitive to choice of the cutoff radius. The average bond length changes from 2.31 Å to 2.55 Å, and the average bond angle drops to 98.07°, which is intermediate between the tetrahedral and octahedral values of 109.5° and 90° respectively.

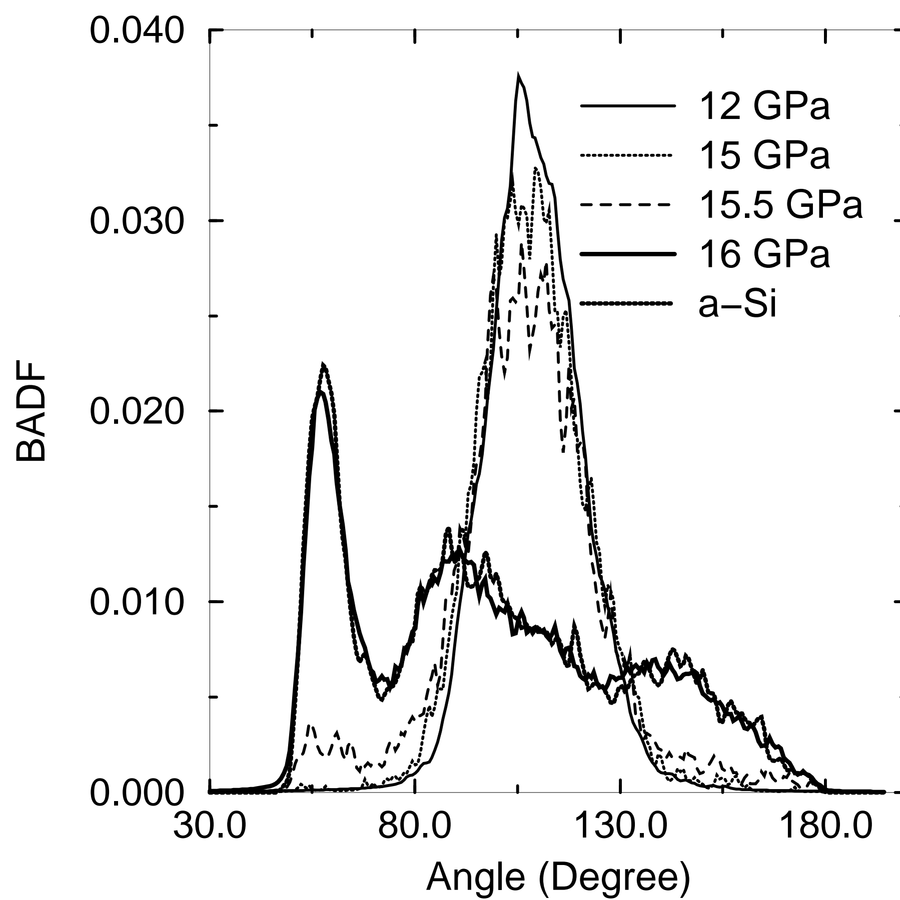

Figure 7.4: The bond angle distribution function (BADF) of *para*-Si and *a*-Si at transition pressure.

Table 7.2: The minimum energies E_{min}, the relative energy difference $\Delta E (= E^i - E^{diamond})$, the corresponding minimum volume per atom V_{min} and its ratio $V^r_{min} = V^i_{min}/V^{diamond}_{min}$, where i is diamond, β-Sn, and *para*-Si phase.

Structure	diamond	β-Sn	*para*-Si
E_{min}(eV/atom)	-108.006	-107.717	-107.826
ΔE_{min} (eV/atom)	0	0.289	0.18
V_{min}(Å^3/atom)	20.76	15.42	21.20
V^r_{min}	1.0	0.74	1.013

7.3.2 Gibbs free energy calculation

In order to study crystallization of the model, we compute the volume dependence of Gibbs free energy. Diamond, β-Sn, and *para*-Si are optimized for several volumes and fit to the Birch-Murnaghan equation of state. We report the minimum structural energy per atom E_{min} and corresponding atomic volume V_{min} for each structure in Table 7.2. For diamond and β-Sn structure, the relative total energy difference per atom ($\Delta E_{min} = E^{\beta-Sn}_{min} - E^{diamond}_{min}$) and the ratio of the equilibrium volume ($V^r_{min} = V^{\beta-Sn}_{min}/V^{diamond}_{min}$) are found to be 0.289 eV/atom and 0.74, respectively. These values are comparable to 0.27 eV/atom and 0.77 reported in accurate self-consistent calculations [99].

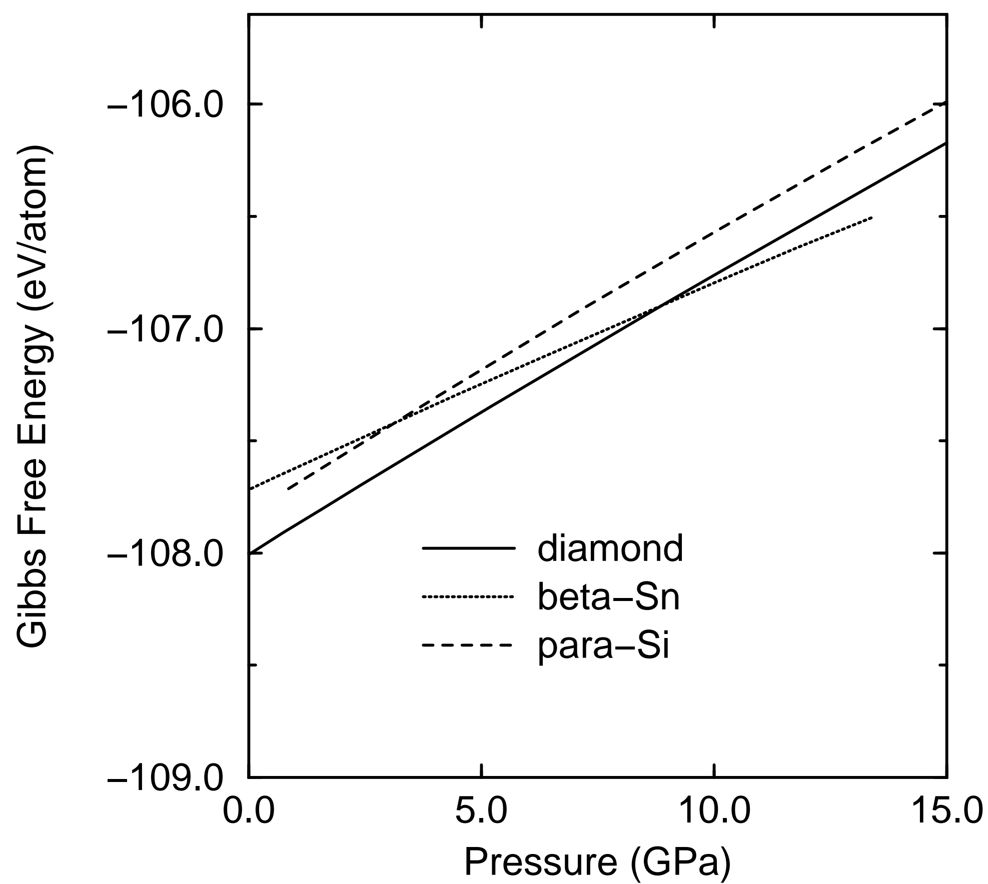

Figure 7.5: Gibbs free energy curve of c-Si, β-Sn and *para*-Si.

The calculated Gibbs free energies ($G = E_{tot} + PV$) at zero-temperature for diamond, β-Sn, and the *para*-Si structure are shown in Fig.7.5. The transition pressure between diamond and β-Sn phase is found to be 9 GPa, which is consistent with the result of 9.5-15.4 GPa reported in previous experiment and theoretical studies [111]. The transition volume of diamond $V_t(diamond)$ and β-Sn $V_t(\beta\text{-Sn})$ is 0.924 and 0.684, respectively. $V_t(diamond)$ value is in good agreement with experiment and theoretical results of 0.89-0.928 whereas the transition volume of β-Sn is less than 0.70-0.719 [111].

The Gibbs free energy curve of the *para*-Si network and β-Sn crosses about 3-4 GPa, indicating a first order phase transition. The critical pressure of this transition is less than that of the diamond to β-Sn transformation. The transition obtained between the *para*-Si model and β-Sn agrees with the experimental study of *a*-Si under pressure but, the predicted crystallization pressure (3-4 GPa) is much less than 8 GPa, which is probably due to the relative energy difference between the *para*-Si structure and *c*-Si ($\Delta E_{min} = E_{min}^{para} - E_{min}^{diamond}$=0.183 eV). This value is higher than an experimental result 0.0977 eV for *a*-Si, as extrapolated to 0 K from the measurement at 960 K using the specific heat listed in that work [89]. When the slope of the common tangent line is considered in energy volume curve, a network with a small energy difference at the same minimum volume yields an increase of the slope and so the transition pressure.

One expects that there is no easy pathway between *para*-Si and β-Sn structure, and the crystallization requires bond breaking (considering ring formation) and a large diffusion of some atoms in contrast to the diamond to β-Sn transition. The

displacement of atoms is hindered at low temperatures and needs more thermal activation. Thus, the crystallization of *para*-Si is kinetically inhibited in the simulation.

7.3.3 Electronic structure

The application of silicon in industry depends strongly on the nature of the electron states near the Fermi level. The pressure dependence of a few tail states and the Fermi level are given in Fig.7.6. The valence tail states tend to move gradually toward the center of the band gap up to 15.5 GPa, and after this pressure the shift of the states becomes more dramatic. The conduction tail states shift into higher energies at low pressures. With further increase of the pressure, the states begins to move to lower energies. When the higher coordination is encountered in the network at 15 GPa, the states move abruptly to the middle of the band gap. The Fermi level exhibits a smooth increase up to 12 GPa. Above this pressure, it shifts to a lower energy. When the topology has higher coordination, the conduction tail states and the Fermi level reveal a complex behavior.

In amorphous tetrahedral materials, the optical gap increases with pressure (0-1GPa) [118]. The pressure coefficient of the fundamental absorption in *a*-Si is positive, +0.25 meV/kbar [118], whereas it is negative in *c*-Si, -1.5 meV/kbar[118] and in *a*-Si:H, -1meV/kbar [119, 121]. Fig.7.6 shows the pressure dependence of the optical gap of *c*-Si and *a*-Si and *para*-Si. The optical gap of *c*-Si decreases smoothly with the application of pressure, and the pressure derivative of the gap is found to be -1.73 meV/kbar in the pressure ranges 0-17 GPa, which is consistent with the experimental result of -1.5 meV/kbar[118]. However, the behavior of the *para*-Si and *a*-Si

model under pressure is different from that of c-Si: It increases initially, reaches a maximum and then decreases under pressure. Above 12 GPa, the gap of the *para*-Si declines because of the increase in the coordination. In the pressure ranges 0-6 GPa, we find that the pressure derivative of the band gap in the *para*-Si model is +0.39 meV/kbar, which is comparable to +0.25 meV/kbar value of amorphous silicon[118].

In order to study the pressure dependence of the localization of electron states, we define the Mulliken charge [87], $Q(n, E)$, for atom n associated with the eigenvalue E. This charge can then be used as a measure of the localization of a given state $Q_2(E) = N \sum_{n=1}^{N} Q(n, E)^2$, where N is the number of atoms in a supercell. For a uniformly extended state, $Q_2(E)$ is 1, while it is N for a state perfectly localized on a single atom. The localization of the electron states near the band gap is depicted in Fig.7.7. As expected the states near the band gap are quite localized at zero-pressure, and the localization of these states decreases gradually, indicating pressure-induced delocalization of the states, similarly to that found in the a-Si [127] and the a-$GeSe_2$ model[154]. At the transition pressure, the tail states are abruptly delocalized as seen in the a-Si networks [127].

7.4 Conclusions

We have studied the pressure-induced phase transition in a 400-atom model of *para*-Si using an *ab initio* constant pressure relaxation technique. The model undergoes a first order phase transition into an amorphous metallic phase. The transition is inhomogenous and begins in the vicinity of defects. The embedded crystalline (diamond) grain transforms to a high disordered topology, which is consistent with

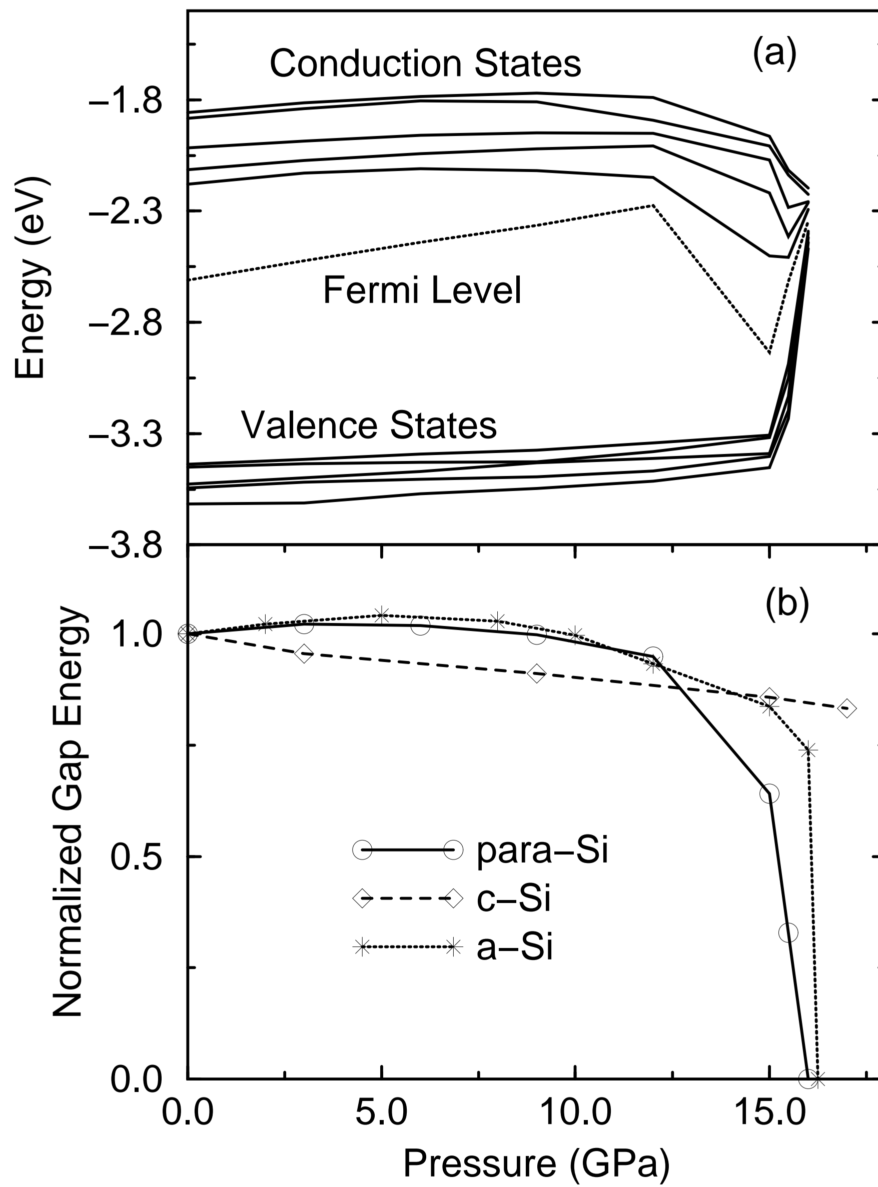

Figure 7.6: Pressure dependence of the normalized optical gap for *para*-Si, *c*-Si and *a*-Si.

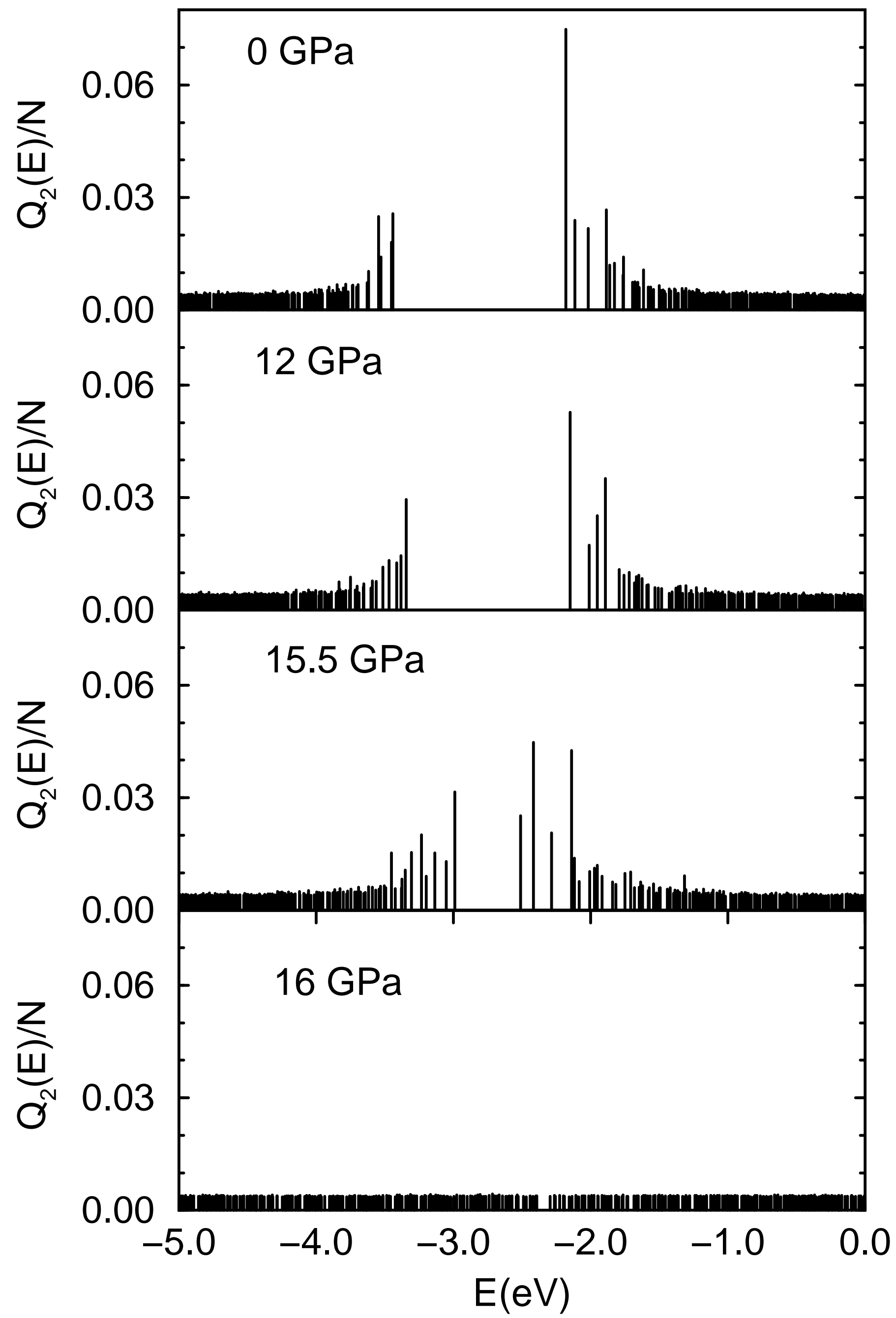

Figure 7.7: The localized states near the band gap.

the study of *p*-Si under pressure. The transition of the grain begins at the boundary and proceeds into the bulk. In order to reveal the size effects of the crystalline grains, it is worth repeating these type of the calculations using large models with a different size of grains. The Gibbs free energy calculation predicts the pressure-induced crystallization of the *para*-Si network. We find that the small increase of the coordination dramatically changes electronic structure of the model.

Chapter 8

First-order pressure-induced polyamorphism in germanium

8.1 Introduction

Some disordered materials show an unusual response to applied pressure. H_2O [1] undergoes a first order phase change from a low-density amorphous phase to a high density amorphous (HDA) phase. The existence of such multiple disordered phases is termed "polyamorphism". A similar transition to that of H_2O was reported in amorphous silicon (a-Si) [127], and in SiO_2 [7, 8]. The general problem of disorder to disorder phase transitions in tetrahedrally bonded materials is little explored with theoretical methods because of the challenge of constructing realistic models and the lack of the good empirical potentials.

Experiment has shown that amorphous germanium (a-Ge) undergoes a transition to a metallic amorphous phase with a sharp drop in resistivity and the optical gap at room temperature around 6 GPa[9], and it appears that this transition was first order. Minomura [10] reported that a-Ge transforms to a disordered β-Sn structure

at 6-7 GPa. An amorphous to β-Sn phase transition with a 5% volume drop is seen at room temperature near 6 GPa in an x-ray diffraction study [17]. However, the amorphous sample contains some crystalline grains, and with the application of pressure the crystalline parts undergo a phase change to β-Sn (only 25% of the amorphous structure transforms to β-Sn) while the other parts still remain amorphous, a "partial structural transition" [17]. On the other hand, no phase transition was observed up to 8.9 GPa in an EXAFS analysis of a-Ge [156]. These studies indicate that the different types of high pressure structures can form (amorphous or crystal) depending on the sample preparation and loading condition [17, 156].

In a theoretical investigation using the Tersoff potential, a gradual amorphous to amorphous phase transformation was obtained [61]. In the same study, however, a free energy calculation predicts a first order amorphous to amorphous phase transition in a-Ge [61]. It is also argued that the HDA phase of a-Ge is similar to liquid-Ge (l-Ge).

Despite extensive experimental studies and one theoretical analysis, several issues concerning a-Ge under pressure remain: (1) What are the microscopic changes in the structure which occur with the application of pressure? (2) Is the transition is first order? (3) Is the transition reversible ? (4) What is the nature of insulator-metal transition? In this chapter, we perform accurate *ab initio* simulations of the response of a-Ge to pressure and give unambiguous answers to the issues reviewed above.

8.2 Methodology

The model used here is generated using an improved version of the Wooten-Winer-Weaire algorithm [74]. At zero-pressure, the model is equilibrated and relaxed with a local orbital first principles quantum molecular dynamic method of Sankey and Niklewski [52]. The energy difference between diamond and the amorphous structure is found to be 150 meV/atom in agreement with 120 meV/atom from a heat crystallization measurement [157, 158]. This Hamiltonian was applied to study a first order amorphous to amorphous phase change in silicon [127], a continuous amorphous to amorphous phase transformation in $GeSe_2$[128], ZB→*Cmcm*→*Imm2* transitions in GaAs and a diamond to simple hexagonal phase transition in silicon [127]. Pressure is applied via the method of Parrinello-Rahman [48], and it is increased in increments of 2 GPa up to 12 GPa, after which an increment of 0.25 GPa is carried out in order to accurately estimate the transition pressure. Dynamical quenching at zero temperature under constant pressure is performed to fully relax the system according to the criterion that the maximum force is smaller than 0.01 eV/Å. We use Γ-point sampling for the supercells Brillouin zone integration, which is reasonable for a 216-atom model. A fictitious cell mass of 16×10^3 amu was found to be suitable for these simulations.

8.3 Result and Discussion

As a preliminary, we perform a simulation for crystalline Ge (c-Ge). At 22-24 GPa the diamond structure transforms into a β-Sn structure in excellent agreement with experiments. The computed transition volume ($V_t^{\beta-Sn}/V^{diamond}$) of the β-Sn is 0.65 and the axial ratio, c/a, is 0.52 at 24 GPa. Both values, however, are less than the experimental results of 0.69 and 0.551 [159] respectively. We calculate the bulk modulus (B) and its pressure derivative (B') of diamond and β-Sn structure using the Birch-Murnaghan equation of state [116] and find $B = 80$ GPa and $B' = 5.19$ for diamond, which are consistent with the experimental values for diamond of $B = 77$ GPa and $B' = 4.6$ [160], and $B = 89$ GPa and $B' = 3.5$ for β-Sn structure, in agreement with $B = 86$ GPa reported in a theoretical calculation using the local density approximation with a nonlinear core-valence interaction[161]. The details of this simulation will be discussed elsewhere.

In the rest of the chapter, we will concentrate on the amorphous structure. The pressure-volume curve of a-Ge is given in Figure 8.1. The volume changes smoothly up to 12.75 GPa and at this pressure an abrupt decline of the volume is seen, indicating a first order phase transition. The volume drops about 19%, which is close to the value of 19.2% obtained in diamond to β-Sn transformation of c-Ge [159]. a-Ge transforms from a low-density amorphous phase to a metallic HDA phase in agreement with the experiment[9], but the predicted transition pressure is larger than that of the experiment. The large value of the critical pressure compared to experiments is commonly seen in constant pressure simulations and can be attributed to the kinetics because of the short time scale of the simulation and finite size of

the simulation cell. In order to obtain an equilibrium critical pressure, we calculate the Gibbs free energy ($G = E_{tot} + PV$) at zero-temperature for a-Ge and the HDA phase of Ge. The Gibbs free energy curve of these phases crosses about 5.2 GPa, which is consistent with the experimental value of 6 GPa[9]. This polyamorphic phase transition is similar to that of H_2O [1, 4],a-Si[127] and SiO_2[7].

Zero-pressure samples upon decompression are mostly amorphous structure with some crystalline fragments [9, 17] and the sample is denser than the initial amorphous structure because of a 5% volume drop at transition pressure [17]. We find that the path on pressure release is not reversed (Figure 8.1), and the obtained structure remains amorphous. The structure is found to be 18% denser than the initial amorphous structure indicating an irreversible amorphous to amorphous phase transition as in H_2O [1, 4], a-Si[127] and SiO_2[7].

The pair distribution function is given in Figure 8.2. The positions of the peaks shift gradually to shorter distances, indicating tighter packing of the network, up to the transition pressure at which the first peak shifts abruptly to a larger distance with a broadened distribution and decreased intensity while the third peak continues to move to a shorter distance with a slightly pronounced intensity. However, there is no well defined second peak at the transition. Upon decompression, the second peak appears gradually and the first and third move to larger distances .

The bond angle distribution function of a-Ge is depicted in Figure 8.2. The network exhibits a smooth distribution with a single peak centered at tetrahedral angle up to the transition pressure. At 12.75 GPa, the bond angle distribution function is rather broad with main peaks around 60°, 90° and 140°. Upon the pressure release,

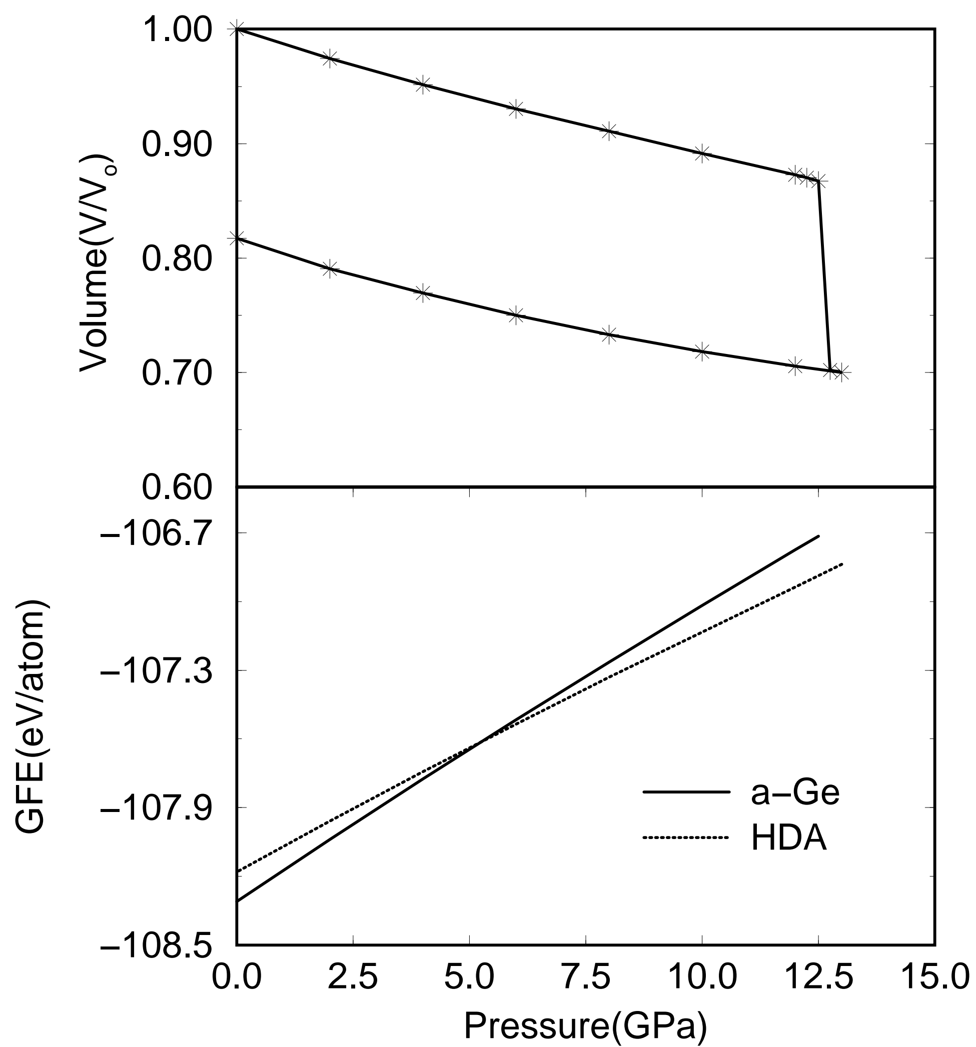

Figure 8.1: (a) The pressure dependence of the normalized volume of a-Ge. (b) The Gibbs free energy of the amorphous and the HDA phase.

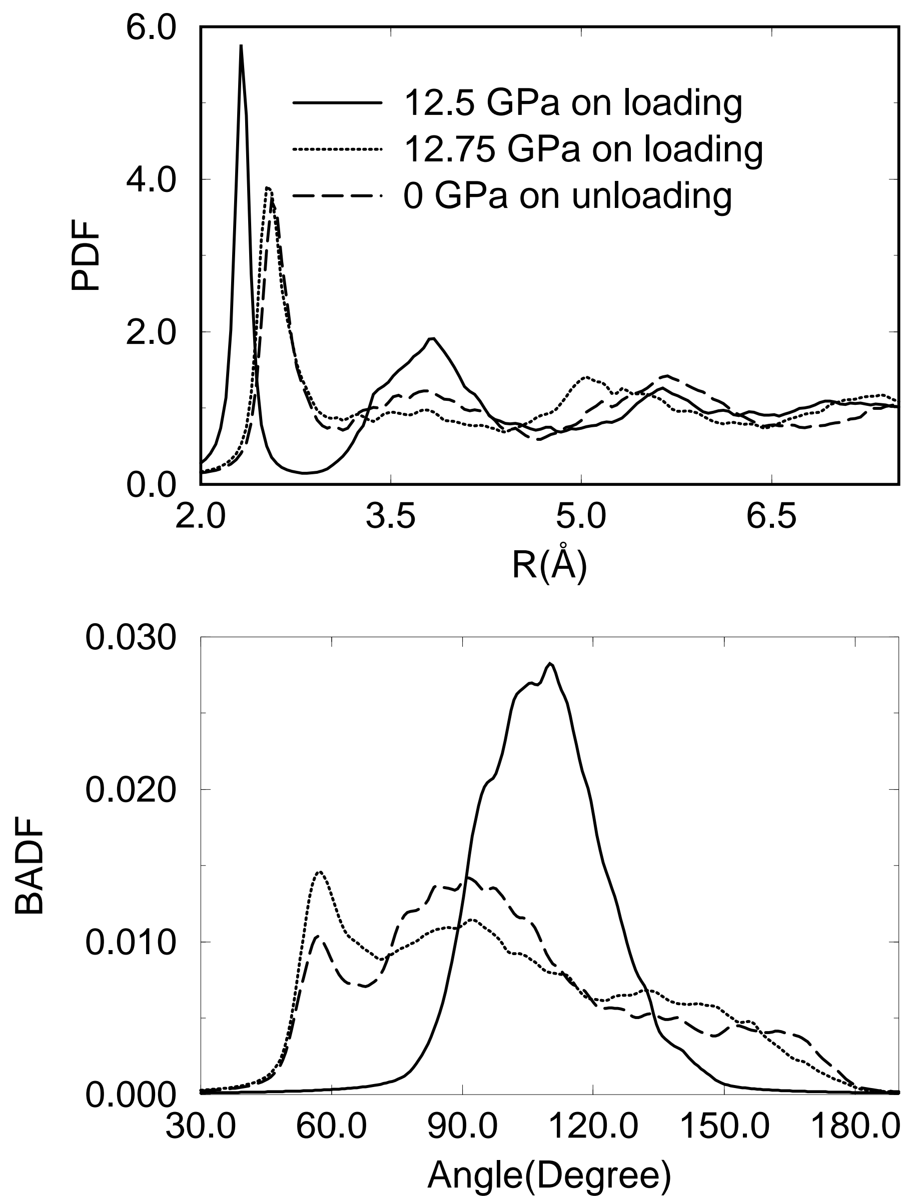

Figure 8.2: (a) The real space pair distribution function. (b) The bond angle distribution function on compression and decompression.

Table 8.1: Structural properties of a-Ge on compression: average bond length (ABL), average bond angle (ABA), width of bond angle distribution (WBAD), and average coordination number (ACN).

Pressure (GPa)	0	8	10	12.5	12.75
ABL (Å)	2.421	2.357	2.345	2.332	2.638
ABA	109.16°	108.98°	108.90°	108.71°	98.81°
WBAD	10.18	11.09	11.46	12.28	32.37
ACN	4.0	4.0	4.0	4.0	8.03

the height of the peaks at 60° and 90° is reversed, and a relatively similar bond angle distribution function to that of l-Ge is formed even though the density of the high pressure phase is larger than that of l-Ge. The peak at 60° represents a more closed packed structure with typical metallic bonding. Upon decompression, the structure gradually changes from a more closed packed structure to an open structure with some tetrahedral bonding.

The high pressure properties of a-Ge are given in Table8.1. Pressure yields shortened bond lengths and narrowed bond angles up to the transition at which point the average bond angle drops to 98.81° which is intermediate between the tetrahedral and octahedral values of 109.5° and 90° respectively, and the average bond length increases to 2.63 Å. The average coordination from the first minimum of the pair distribution function within a critical cutoff radius $R_c = 3.01$ Å is ~ 8 and is quite sensitive to choice of the cutoff radius. Upon pressure release, the average bond angle

Table 8.2: Structural properties of a-Ge on decompression. Same nomenclature as Table 8.1.

Pressure (GPa)	0	2	6	8	10
ABL (Å)	2.667	2.676	2.640	2.639	2.653
ABA	100.73°	100.09°	100.31°	99.97°	99.21°
WBAD	31.30	31.90	31.64	31.92	32.41
ACN	6.48	6.97	6.98	7.27	7.87

and bond length exhibit a small change, whereas the average coordination is reduced to 6.48(Table 8.2). This value is close to the coordination of l-Ge, 6.8 obtained in an x-ray diffraction study [162], and 6-7.1 in a first principles calculation[163]. Also the position of the first peak, 2.59 Å , is comparable to 2.70 Å [162] and 2.63 Å [163] of l-Ge.

The volume change upon compression (up to 12.5 GPa) and decompression can be fitted to the Birch-Murnaghan equation of state [116]. The calculation yields $B = 73$ GPa and $B' = 3.2$ for a-Ge. These values are different from $B = 34.5$ GPa and $B' = 8$ reported in an x-ray diffraction study [17], and $B = 97 \pm 8$ GPa and $B' = 6 \pm 2$ obtained in an EXAFS analysis [156]. For the HDA phase, we find $B = 55$ GPa and $B' = 3.19$. The softening of these bulk modulus compared to the other structures is due to the high coordination, which leads to additional restrictions to the bulk relaxation in the disordered networks [117].

We can track the electronic nature of the pressure-induced insulator-metal transition in the simulation. With the application of pressure the valence tail states tend to move toward the center of the band gap. However, the conduction tail states reveal a complex behavior: up to 8 GPa, the states shift to higher energies, producing an increase of the band gap, and after this pressure the states move to lower energies, yielding a decrease of the gap. The response of the conduction tail states to pressure determines the optical gap of a-Ge. Simultaneously, a broadening of the band is observed. The Fermi level lies on the middle of the band gap and gradually shifts to a higher energy with an increase of pressure. The pressure dependence of the optical gap is depicted in Figure 8.3. The gap *increases* smoothly up to 8 GPa, in agreement with the experiment but, after this pressure it decreases gradually. The band gap exhibits a linear behavior up to 4 GPa and has a slope of 1.68 meV/kbar, which is comparable to the coefficient 0.8 meV/kbar[17] and 3.5 meV/kbar [118]. At 12.75 GPa, a-Ge transforms to a metallic phase with a sharp drop in the optical gap. The tiny gap is a finite size and minimal basis artifact: the material is certainly conducting.

In order to study the pressure dependence of the localized states, we define the Mulliken charge [87], $Q(n, E)$, for atom n associated with the eigenvalue E. This charge can then be used as a measure of the localization of a given state $Q_2(E) = N \sum_{n=1}^{N} Q(n, E)^2$ where N is the number of atoms in a supercell. For a uniformly extended state, $Q_2(E)$ is 1, while it is N for a state perfectly localized on a single atom. The localization of the electron states near the band gap is depicted in Figure 8.3. As expected the states near the band gap are quite localized

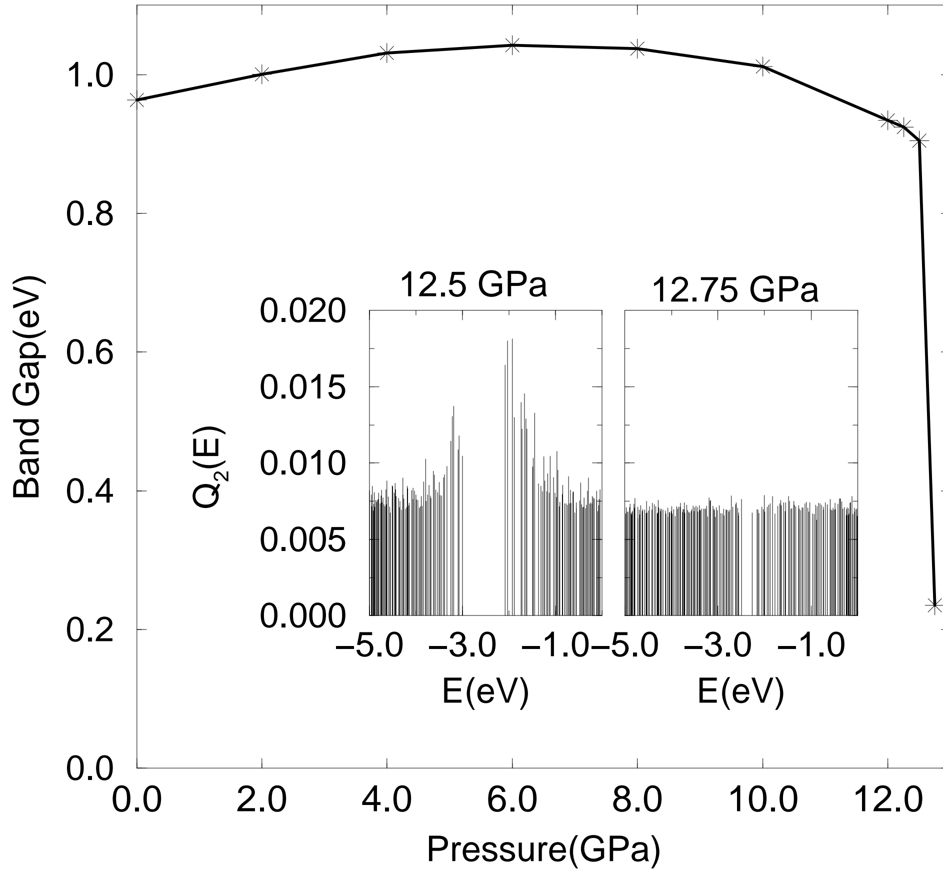

Figure 8.3: The pressure dependence of the optical gap. **Inset:** Electronic eigenstates in the band gap region. The position of the vertical bars represent the eigenvalues of the electronic eigenstates, and the height of the bars is the spatial localization ($Q_2(E)$). The Fermi level lies in the middle of the band gap. Note the abrupt delocalization of the tail states at 12.75 GPa.

at zero-pressure, and the localization of these states decreases gradually, indicating pressure-induced delocalization of the states, similarly to that found in *a*-Si[127] and *a*-$GeSe_2$[128]. At the transition pressure the tail states are abruptly delocalized as seen in *a*-Si.

It is valuable to predict the pressure dependence of the phonon modes before and after the phase transition. The physical origin of the phase transition can be understood by examining the soft phonon modes. The vibrational density of states (VDOS) is given in Figure 8.4. With the application of pressure the acoustic modes soften while the optical band shift to higher frequencies up to the transition pressure, at which point the mode frequencies decline abruptly and the bands overlap as seen in *a*-Si [127]. We also find that the localized eigenmodes at zero-pressure are extended with pressure. Similar change of localized states has been observed in the theoretical study of *a*-$GeSe_2$ [128], *a*-Si [127] and SiO_2 [46].

In summary, *a*-Ge undergoes a first order amorphous to amorphous phase transition, which is due to the ideal amorphous structure such that no crystalline remnant exists in the network. Nevertheless, it is worth repeating this type of study on large systems with different structures, especially containing crystalline grains, at different temperature.

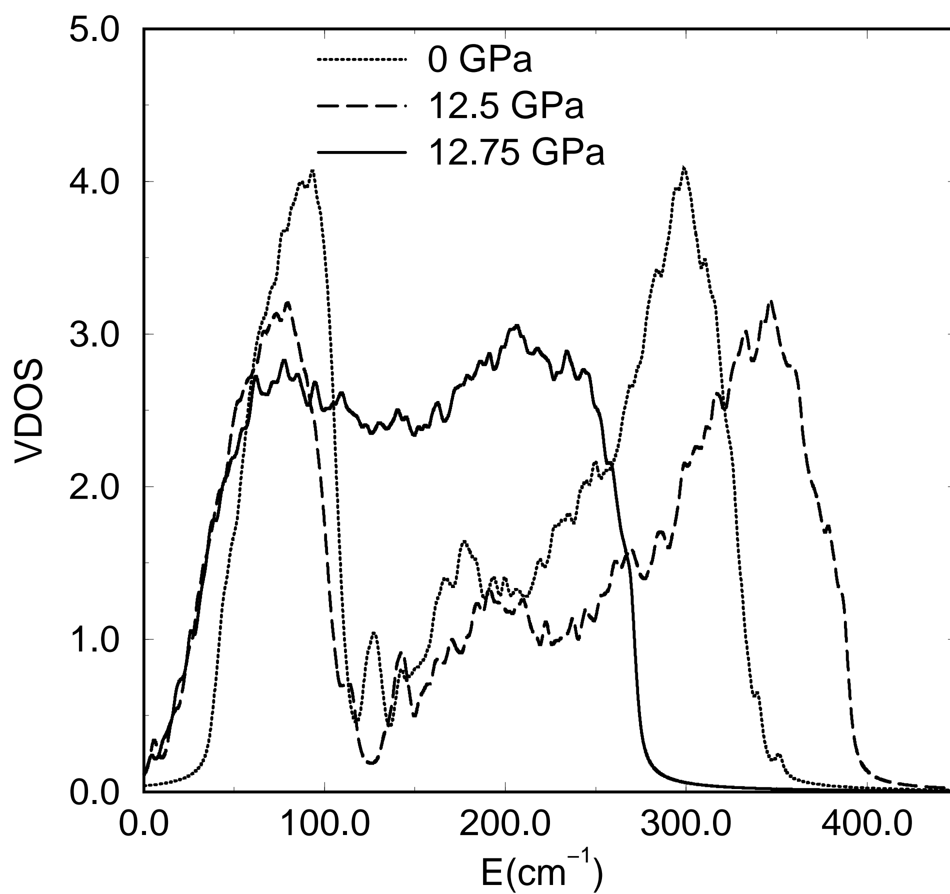

Figure 8.4: Vibrational DOS at 0, 12.5 and 12.75 GPa.

Chapter 9

Simulation of pressure-induced polyamorphism in a chalcogenide glass $GeSe_2$

9.1 Introduction

Pressure-induced insulator-metal transitions have long attracted interest in the condensed matter physics community. An area of recent emphasis is the amorphous to amorphous phase transition. For example a-Si [127, 9], a-Ge [9] and H_2O [1] show a first order phase change from a low density amorphous (LDA) to a high density amorphous (HDA) phase while the transition proceeds gradually in SiO_2 [5, 7] and GeO_2 [6]. In the case of amorphous and crystalline binary chalcogenide (AB_2, A=Ge, Si; B=S, Se) the pressure- induced phase transition is little understood. This is due to the challenge of constructing large realistic models, and the lack of good empirical potentials. In the present study, we perform a first principles study to elucidate the mechanism of insulator-metal transition in amorphous $GeSe_2$ (a-$GeSe_2$). The

material was intensively studied and thoroughly reviewed by Boolchand [164].

For the crystal, the three-dimensional $I\bar{4}2d$ [165, 166] and two-dimensional HgI_2 [21] structures are reported at high pressure in chalcogenides. Recent experiments showed that crystalline $GeSe_2$ and GeS_2 transform to an amorphous state near 7 GPa at room temperature [167]. Shimada *et al.* [21] have reported the production of a high pressure form of a-$GeSe_2$ and noted that crystallization at temperatures below 573 K is inhibited. Also, they noted cristobalite and CdI_2 type compounds at about 3 GPa and 7 GPa at 573-873 K. Grande *et al.* [166] reported that a-$GeSe_2$ compressed at 3 and 7.7 GPa (at 573 K) is partially crystallized. Prasad *et al.* [168] studied Ge_xSe_{100-x} ($0 \leq x \leq 40$) glasses up to 14 GPa and temperatures 77-298 K, and observed a discontinuous glassy semiconductor to a crystalline metallic phase transition, contrary to observations by Shimada *et al.* [21]. The high-pressure crystalline phases in a Ge_xSe_{100-x} system do not correspond to any of the known $GeSe_2$ phases. Based on the experiments, it is argued that possible structural transitions in glassy $GeSe_2$ at high pressure and high temperature, could be similar to the ones in crystalline $GeSe_2$ [33].

In this chapter, we present an *ab initio* constant pressure molecular dynamics (MD) study of a semiconductor to metal transition in a-$GeSe_2$, using a relatively large 216-atom realistic model. To our knowledge, this is the first direct MD simulation to model the pressure-induced phase transition in a-$GeSe_2$. We find that a-$GeSe_2$ undergoes a continuous transition to an amorphous metallic phase. The transition is reversible apparently because of the locality of the structural transformations. The coordination of Ge atoms changes gradually from a four-fold to a six-fold coordination

while Se atoms transform from a two-fold to a four-fold coordination. The initial compression causes a slight reduction of chemical disorder while it leads to more topological disorder in the network. At high pressure, chain-like Se-Se clusters emerge as seen in elemental Se. The intensity of the first sharp diffraction peak (FSDP) decreases smoothly, and its position shifts to a higher Q with increase of pressure. The optical gap decreases gradually with pressure. It is also found that highly localized electronic and vibrational states at zero-pressure become extended with the application of pressure.

9.2 Methodology

The simulation reported here is carried out in a large realistic 216-atom model of a-$GeSe_2$. The model is due to Cobb, Drabold, and Cappelletti, and is in uniform agreement with structural, vibrational and optical measurements [76]. The model successfully produces the FSDP which is in excellent agreement with the new experimental results [169] (see Ref. [76, 109] for more details). The model was generated using a local orbital first principles quantum molecular dynamics method which employs density functional theory within the local density approximation and the Harris functional with hard norm-conserving pseudopotentials. The method is implemented entirely in real space. The short-range nonorthogonal single-ζ (1s+3p per site) local orbital basis of compact slightly excited *fireball* orbitals of Sankey and Niklewski offered an accurate description of the chemistry with a significant computational advantage [52], ideal for this complex system. The method was applied to form structural models of the surface of glassy $GeSe_2$ [109], liquid-$GeSe_2$ [170] and a wide

range of other amorphous materials [108, 77]. The Hamiltonian has succesfully predicted a first-order pressure-induced phase transition in crystalline silicon (diamond to simple hexagonal), in amorphous silicon (amorphous to amorphous) [127], and in crystalline GaAs (zich-blende to *Cmcm* and *Imm2*) [171]. Dynamical quenching under constant pressure is performed to fully relax the system. Pressure is applied via the method of Parrinello and Rahman [48] which enables the simulation cell to change volume and shape. The number of steps is chosen according to the criterion that the maximum force was smaller than 0.01 eV/Å. For some pressures, this required in excess of 7000 force calls. All the calculations used solely the Γ point to sample the Brillouin zone, which is reasonable for a cell with 216 atoms. A fictitious cell mass of 1.6×10^4 amu was found to be suitable for this simulation.

Once the equilibrium configuration under pressure is obtained, we compute the dynamical matrix, displacing every atom in the cell in three orthogonal directions (0.03 Å) and computing the resulting spring constants as second derivatives of the total energy of the system. Diagonal zing the dynamical matrix we receive its eigenvectors and corresponding squared normal-mode frequencies ω^2, which enable us to carry out the full investigation of the vibrational behavior of the equilibrium configurations.

9.3 Structural Properties Under Pressure

9.3.1 Pressure Dependence of Volume

We plot the pressure dependence of the relative volume in Figure 9.1. The volume changes smoothly up to about 12 GPa, and then exhibits "ripples" at several pressures. At 12 GPa, $\sim$ 35.2% atoms are involved in coordination changes and the number of atoms suffering coordination modification increases to $\sim$ 51.9% at 13 GPa. Since the volume drop at these pressures is relatively small, we interpret the pressure-induced phase change of a-$GeSe_2$ as a continuous transition, in stark contrast to results on a-Si[127].

Our model reproduces the high pressure form of the amorphous structure which is in excellent agreement with the experiment [21] but, contrary to the study of Grande *et al.* [166] and Prasad *et al.* [168]. It was shown that a-GeS_2 is crystallized at 873 K and densified at 543 K [173]. In a recent study, pressure-induced crystallization of vitreous $ZnCl_2$ was reported at room temperature but, there is a transition to a HDA at low-temperature [16]. The crystallization of an amorphous phase may be inhibited at low-temperature and an amorphous to amorphous transition is favorable.

The pressure-volume curves on decompression at 16 GPa and 75 GPa are given in Figure 9.1. The path followed from 75 GPa is reversed up to 30 GPa. After this pressure the curve develops a hysteresis, as seen in the pressure release from 16 GPa. Such a hysteresis is perhaps expected after 12 GPa because of the discontinuities seen in the pressure volume curve. A decompression started at different final pressure gives a very similar structure, albeit with small differences in density and coordination. In

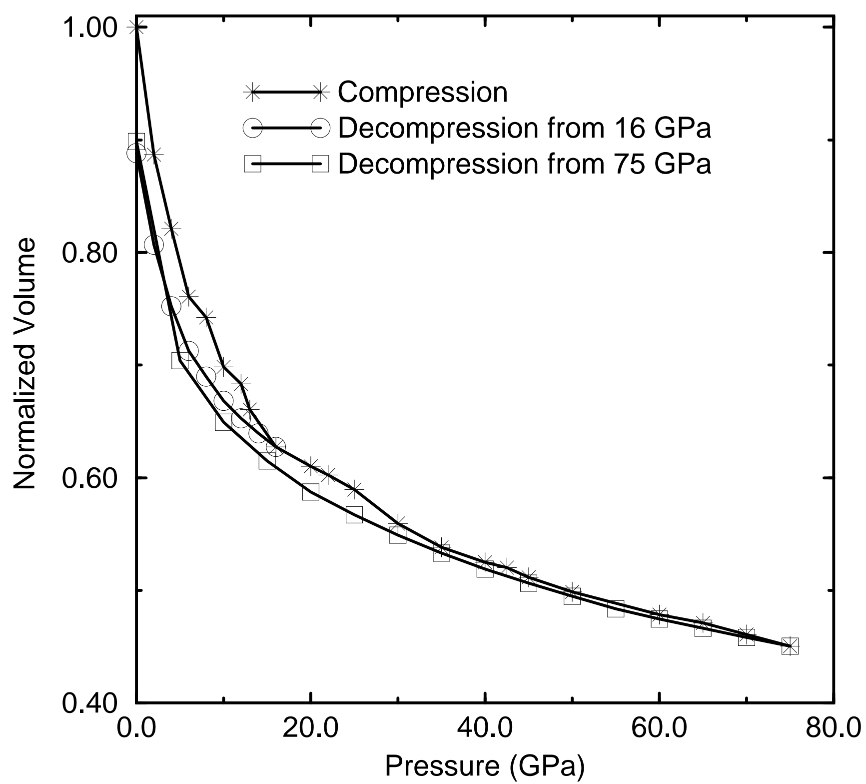

Figure 9.1: The normalized volume of a-$GeSe_2$ changes smoothly with up to 12 GPa. After this pressure and several others, it shows slope changes. Upon pressure release from 75 GPa, the path is reversed up to 30 GPa, and thereafter hysteresis is seen.

a contrast to SiO_2 [7], GeO_2 [6], H_2O [1] and a-Si [127], the amorphous to amorphous phase transition in a-$GeSe_2$ is reversible, as reported for a-As_2Te_3 [174].

9.3.2 Structural Correlation

The effect of pressure on the FSDP was studied in many glasses. X-ray diffraction patterns of GeS_2 glass [119], x-ray diffraction of SiO_2 [5], pressure densified SiO_2 glass [175] and models [176] showed a decrease of the intensity of the FSDP and a shift of its position into a higher Q relative to the zero-pressure matrix. The densification of liquid-$GeSe_2$ due to a temperature increase produces the same effect on the FSDP [177]. An experiment [5] also reported the appearance of a peak between the FSDP and the second peak in $S(Q)$ of SiO_2 under pressure.

The total $S(Q)$ and Faber-Ziman partial structure factors are depicted in Figure 9.2. The intensity and position of $S(Q)$ exhibits dramatic changes at $Q < 6$ Å^{-1} under pressure. The FSDP is suppressed, and its position shifts to a higher Q with the application of pressure. The result emphasizes an inverse correlation between the density (coordination) of the glassy materials and the FSDP. We also find the emergence of a peak at about 2 $\AA^{-1}$. This peak is due to Ge-Ge correlations. The suppression of the FSDP and the emergence of the new peak suggest a change of the intermediate range order in the network [5]. Dramatic changes are observed in the second and third peak: Although both peaks move to a higher Q, the intensity of the second peak increases while the third one decreases with pressure. All partials lead a contribution to the increase of the second peak, but Ge-Se correlations contribute predominantly. Generally the behavior of $S(Q)$ under pressure is in excellent

agreement with experiments on glassy systems [5, 119].

The total and partial real space pair distribution functions of a-$GeSe_2$ are given in Figure 9.3. The position of the first peak shifts to a larger distance, and its intensity decreases with pressure corresponding to the onset of the coordination change. The second peak position shifts to a lower distance with broadened distribution. The Ge-Se pair distribution function becomes quite uniform after the nearest neighbor-peak, except for a feature around 5.7 Å. With an increase of pressure, the position of the peak shifts to smaller distance with broadened distribution, which is parallel to how the FSDP changes with pressure. A weak peak emerges around 3.2 Å in Ge-Se partial. The corresponding Q value for this distance is crudely estimated to be $\sim$ 1.96 $Å^{-1}$ using $r = 2\pi/|\mathbf{Q}|$, which is also in agreement with the appearance of a peak in $S(Q)$ at about 2 $Å^{-1}$. The nearest and second nearest peak in Se-Se correlations merge and make a broad peak around 2.8-3.2 Å. In addition, a second peak emerges at about 4.8-5.4 Å . The results suggest that Se atoms exhibit a comparatively large structural modification relative to Ge atoms. The Ge-Ge and Se-Se clusters at 65 GPa are given in Figure 9.4. Surprisingly we find that Se atoms form chain-like clusters, as seen in pure Se, while Ge atoms form very simple clusters.

The bond angle distribution function is given in Figure 9.5. We find dramatic changes in the position and intensity of the peak; the intensity of the peak decreases with a broad distribution, and its position shifts gradually to lower angles. We calculated the information entropy [178] of the bond angle distribution function at a given pressure using $S = -\sum_i P_i \ln P_i$, where P_i is the distribution of the bond angles. The entropy of the bond angle distribution function is a measure of how

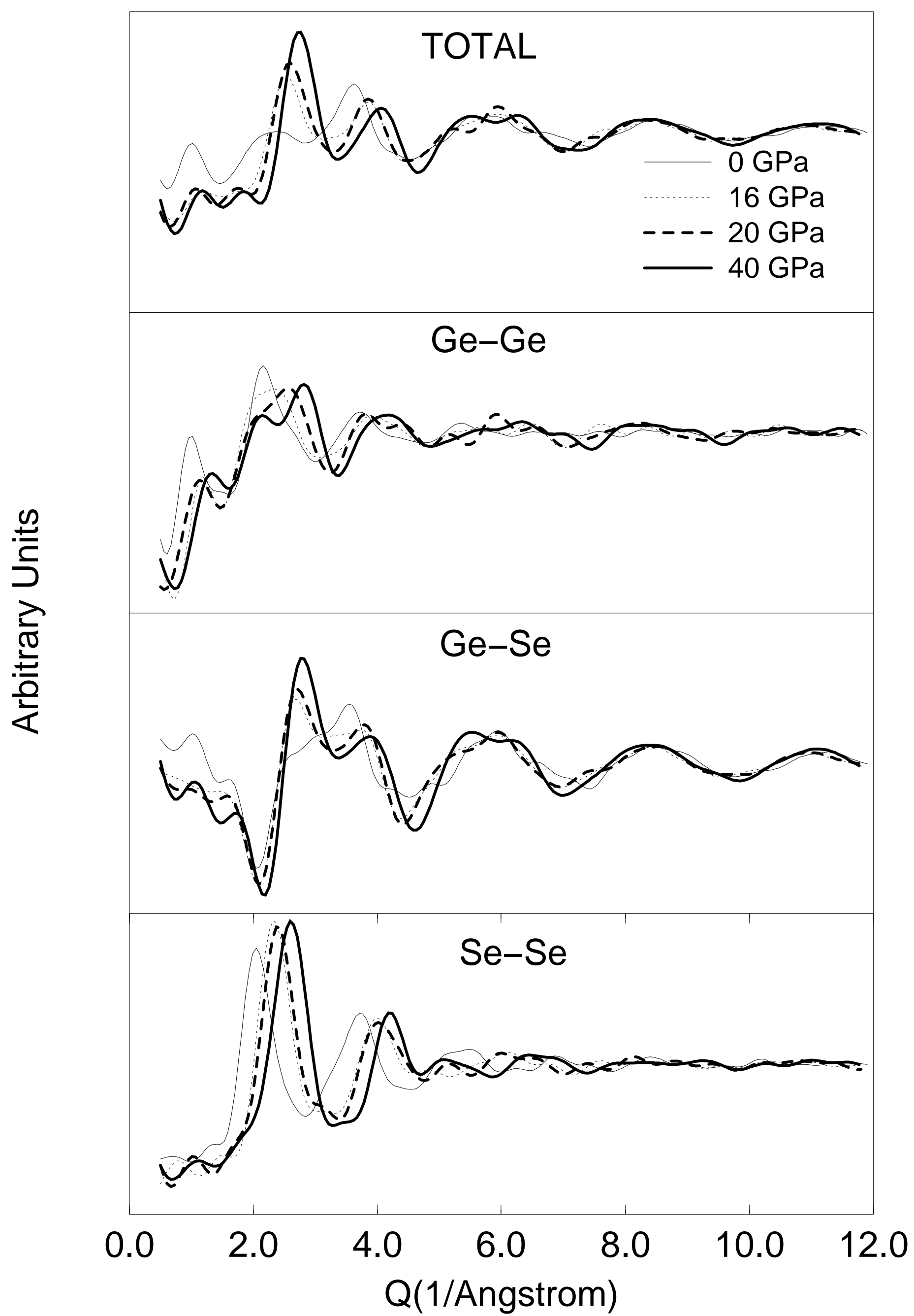

Figure 9.2: The behavior of the total structure factor $S(Q)$ and Fiber-Ziman structure factors. The FSDP is suppressed and its position shifts toward higher Q with increasing pressure. A new peak emerges at about 2 Å^{-1} which is mostly due to Ge-Ge correlation.

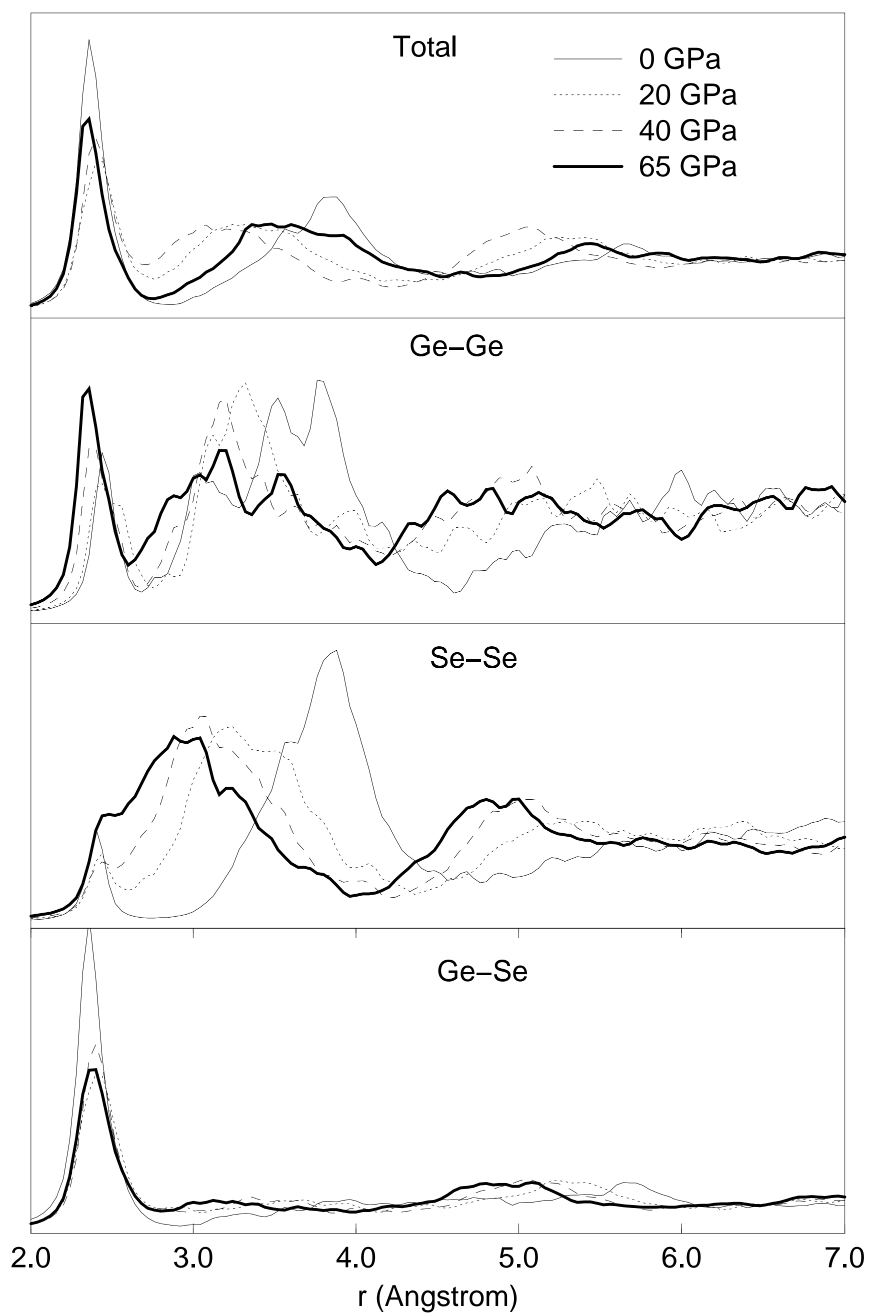

Figure 9.3: The total and partial real space pair distribution functions of a-$GeSe_2$.

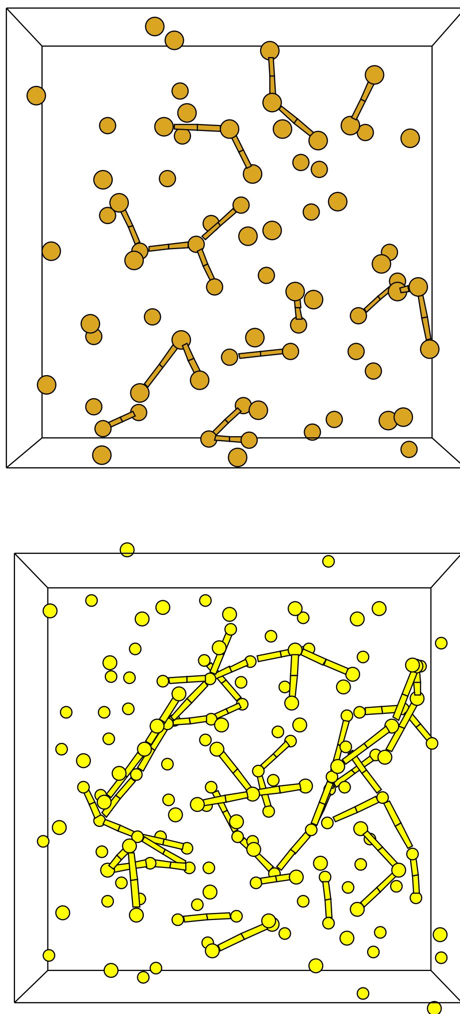

Figure 9.4: Atomic configuration at 65 GPa. Ge (top) and Se (bottom) atoms are shown separately. Note the chain-like cluster of Se atoms.

well defined the bond angles are at each pressure (large entropy, broad distribution). The pressure dependence of the entropy is depicted in Figure 9.5.We find a very dramatic increase in the entropy up to 16 GPa, implying a fast structural change in the network. After this pressure, the growth in S is slower. The utility of S for analyzing structural properties is under investigation.

9.3.3 Topology and Bonding Under Pressure

Table 9.1 presents structural properties of a-$GeSe_2$ at several pressures. We also plot the pressure dependence of structural properties in Figure 9.6. The average coordination, which is defined from the first minimum of the total pair distribution function (R_c=2.70-2.80 Å depending on pressure) increases gradually up to 12 GPa. In a pressure range of 13-20 GPa, it shows a small abrupt increase at several pressures. Ge atoms transform gradually from four-fold to six-fold coordination while the average coordination of Se changes from two-fold to four-fold. Either Ge or Se atoms involved in homopolar bond(s) have a tendency to form a more closely packed structure than those chemically ordered.

The average nearest neighbor distance between atoms is given in Figure 9.6. The average nearest neighbor distance and the Ge-Se separation exhibit a small increase up to 12 GPa, and then both increase substantially in the pressure range of 12-16 GPa. Above 16 GPa, these separations do not show a significant modification but a small fluctuation. The increase of the neighbor distance is due to the formation of new bonds which are larger than the average. Pressure induces a large increase of the Se-Se separation. The large modification of the Se coordination is responsible

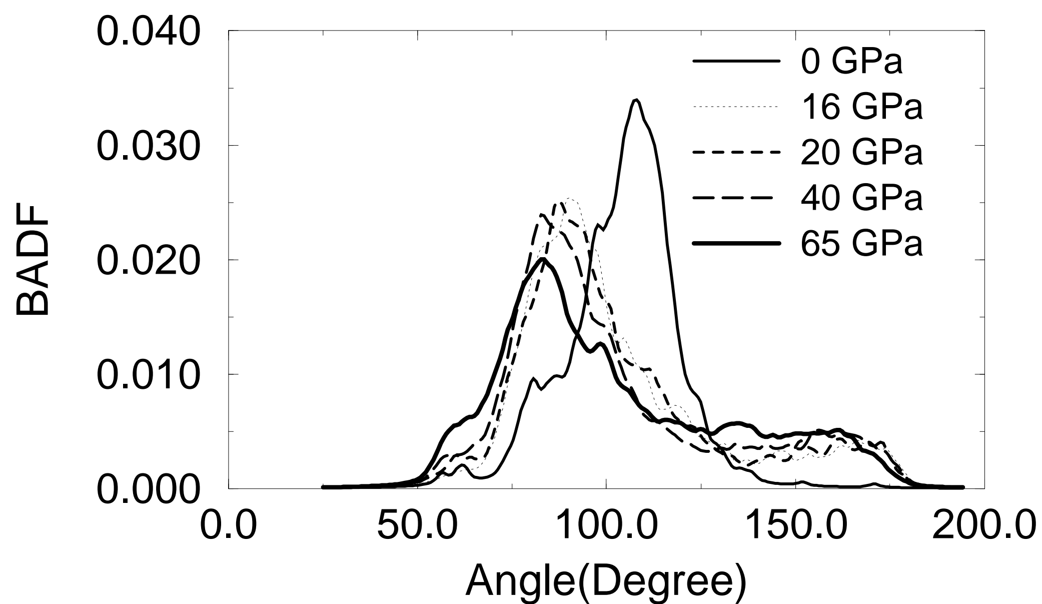

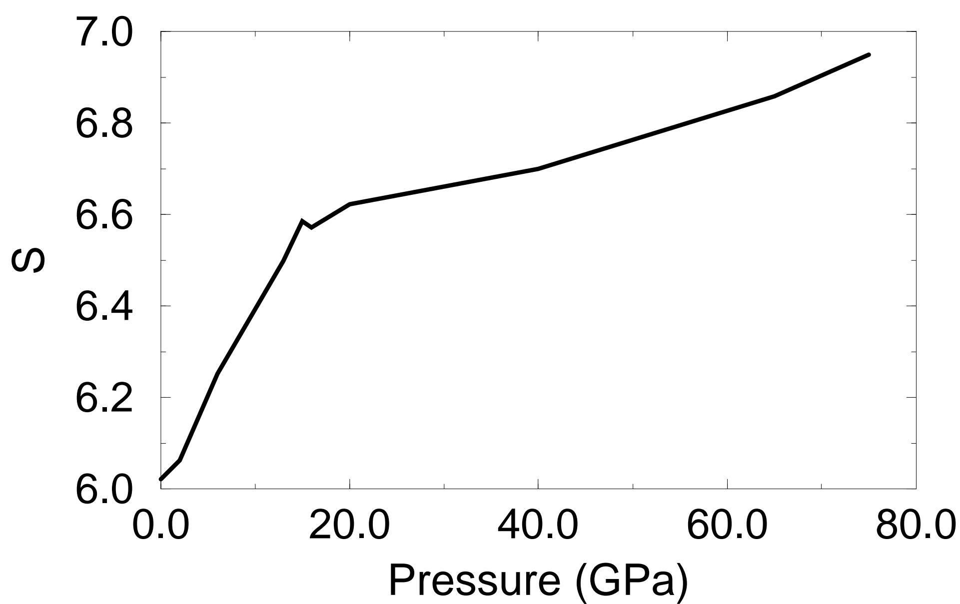

Figure 9.5: (a) The bond angle distribution function (BADF). (b) The information entropy of the bond angle distribution function.

Table 9.1: Structural properties of a-GeSe$_2$ under pressure: average nearest neighbor distance (ANND), average bond angle (ABA), and average coordination number (ACN) which is calculated from the first minimum of the PDF (R_c=2.70-2.80 $\mathring{A}$).

Pressure (GPa)	0	20	40	60	65
ANND (Å)	2.39	2.455	2.446	2.431	2.442
ABA	103.76°	102.87°	102.64°	102.51°	102.31°
ACN	2.68	3.46	4.04	4.40	4.84
ACN-Ge	3.86	4.83	5.52	6.08	6.10
ACN-Se	2.09	2.77	3.30	3.7	4.2

for this behavior, yielding the occurrence of large Se-Se clusters in the network. On the other hand, the average Ge-Ge distance decreases, except for pressures at which "ripples" are observed in the pressure volume curve.

One of the concerns in a-GeSe$_2$ is the quantity of chemical disorder, in particular the fraction of "wrong" (homopolar) bonds between like atoms. The initial compression causes a slight reduction of wrong bonds in a-GeSe$_2$. In the pressure range of 12-20 GPa, there is a significant increase from $\sim$ 10.95% to $\sim$ 17.11% because of structural changes in the network. At 65 GPa, $\sim$ 28.48% of bonds are homopolar. The fraction of chemically disordered Ge and Se atoms as a function of pressure is given in Figure 9.6. At zero-pressure, 25% of Ge and Se atoms are involved in homopolar bonds, which is in close agreement with the value of 25(5)%

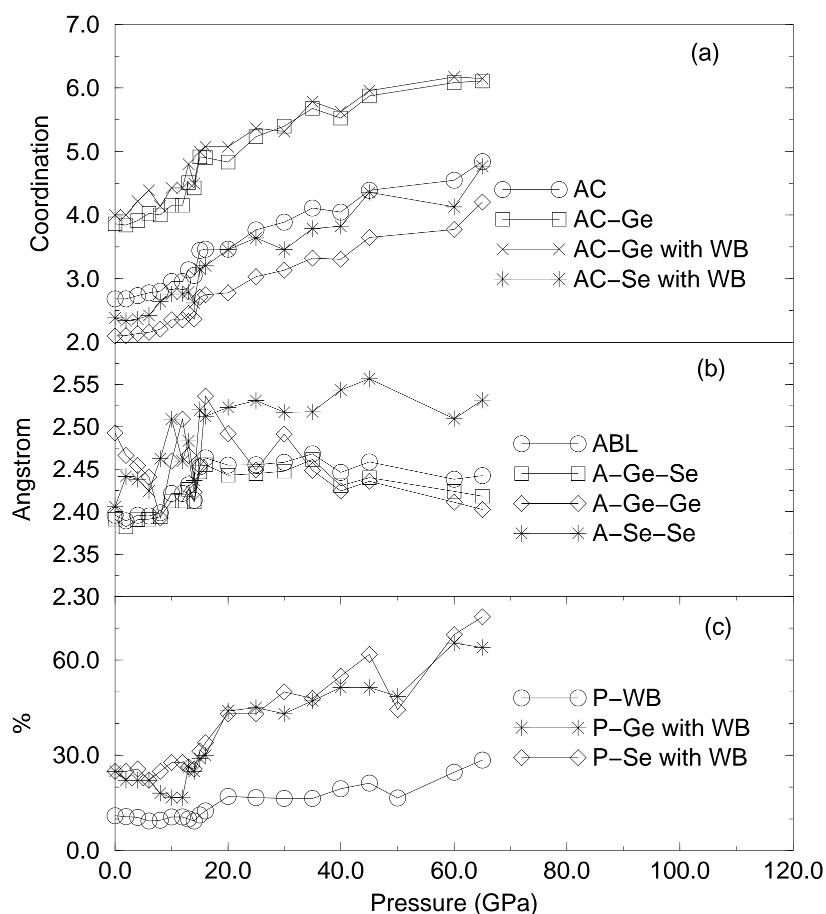

Figure 9.6: Pressure dependence of structural properties of a-$GeSe_2$: (a) the average coordination (AC), the average coordination of Ge (AC-Ge), the average coordination of Se (AC-Se), the average coordination of Ge with wrong bond(s) (AC-Ge with WB), and the average coordination of Se with wrong bond(s) (AC-Se with WB). (b) The average bond length (ABL), the average Ge-Se separation (A-Ge-Se),the average Ge-Ge distance (A-Ge-Ge), and the average Se-Se separation (A-Se-Se). (c) The percentage of the total wrong bond (P-WB), the percentage of Ge atoms with wrong bond(s) (P-Ge with WB), and the percentage of Se atoms with wrong bond (P-Se with WB).

Ge and 20(5)% Se (if only dimers are formed) [169]. The fraction of Se atoms with wrong bonds does not change significantly up to 12 GPa, and then its behavior tracks that of the wrong bonds. The number of chemically disordered Ge atoms declines slightly in the presure range of 0-13 GPa. We find that some Ge-Ge homopolar bonds break under pressure, and the atom forms new bond(s) with decreasing or increasing coordination or sometimes without changing coordination depending on the local environment. In an experimental study of pressure-induced amorphization of $GeSe_2$, it is reported that the Raman spectrum of the decompressed sample does not show the presence of the vibrational modes at about 180 cm^{-1}, indicating that pressure suppresses Ge-Ge bonding [33]. At 13 GPa, the number of Ge involved in homopolar bonding rises suddenly from $\sim$ 16.66% to $\sim$ 26.28%, where the pressure volume curve shows the first discontinuity. After 20 GPa, it increases gradually with pressure. In summary, pressure suppresses the occurrence of chemical disorder up to 13 GPa. At this pressure and thereafter, the system cannot resist an increase in chemical disorder. We note that while pressure reduces chemical disorder, it results in a softening of different parts of the network and in more topological disorder in the system, which leads to a gradual transformation to a HDA phase of a-$GeSe_2$.

9.3.4 Discussion

In oxide glasses and a-$GeSe_2$, the cation atoms transform gradually from four-fold to six-fold coordination while the average coordination of the anion atoms is different; in SiO_2 and GeO_2, the anion atoms (O) transform from two-fold to three-fold coordination whereas the average coordination of Se in a-$GeSe_2$ change from two-fold to

four-fold. The existence of Se-Se clusters contribute to the increase of the coordination. This important distinction is due to the ionicity of the materials; the oxide glasses are far more ionic and hence homopolar bonding is much disfavored.

Unlike elemental amorphous materials (selenium [179], germanium [9, 17], and silicon [9]), the transition proceeds continuously in most amorphous compounds such as *a*-GaSb [180] and *a*-GaAs [10]. Bond angle distributions seems to be a key signature in the behavior of the tetrahedral network under pressure [180]. Amorphous materials can be classified into two classes; a continuous transition class (mostly compounds) and a discontinuous transition class (mostly elemental) based on their behavior under pressure. The similarity of these two classes is a structural disorder which causes mainly a significant reduction in the transition pressure compared to their crystalline states. The difference is that the continuous transition class has chemical disorder in addition to the structural disorder, and the importance of the chemical disorder is determined to large extent by ionicity (the more ionicity present, the more chemical order). To our knowledge, the effects of chemical disorder on pressure-induced phase transition have not been studied or considered. The present study suggests that chemical disorder plays a very important role in amorphous compounds. Since the formation of wrong bond(s) is unfavorable energetically (the penalty is small in *a*-$GeSe_2$), the application of pressure causes a suppression of the occurrence of chemical disorder, and simultaneously it results in a decomposition of the different parts of the model. Therefore, we argue that not only structural disorder but chemical disorder needs to be considered for a gradual transformation.

9.4 Electronic Structure

Simulation enables us to study the electronic nature of a pressure-induced insulator-metal transition. It is found that both the conduction and valence tails shift to higher energies at low-pressure. The shift of the valence tail dominates, producing a decrease of the band gap. Above 2 GPa, the conduction tails moves to lower energies while the valence band continues to shift toward higher energies, implying a pronounced decrease of the band gap. A broadening of the bands under pressure is also observed. Figure 9.7 shows the pressure dependence of the optical gap in a-$GeSe_2$. The gap decreases non-linearly with pressure. The decrease of the band gap is consistent with a previous report on a-$GeSe_2$ [181]. In a pressure range 2-16 GPa the decrease is so pronounced because of the dramatic structural changes in the system.

Sakai *at al.* [174] pointed out that the decrease in the gap of chalcogenide semiconductors is associated with an increase of the dielectric constant which tends to decrease the localization of the gap states and to promote metallic conduction at high pressure. In order to characterize the localization of electronic states through the transition, we define the Mulliken charge [87] $Q(n, E)$ for atom n associated with the eigenvalue E. This charge can then be used as a measure of the localization of a given state $Q_2(E) = N \sum_{n=1}^{N} Q(n, E)^2$, where N is the number of atoms in a supercell. For a uniformly extended state, $Q_2(E)$ is 1, while it is N for a state perfectly localized on a single atom. The localization of the electron states is shown in Figure 9.8. Each peak on the figure represents an eigenvalue. The larger $Q_2(E)$

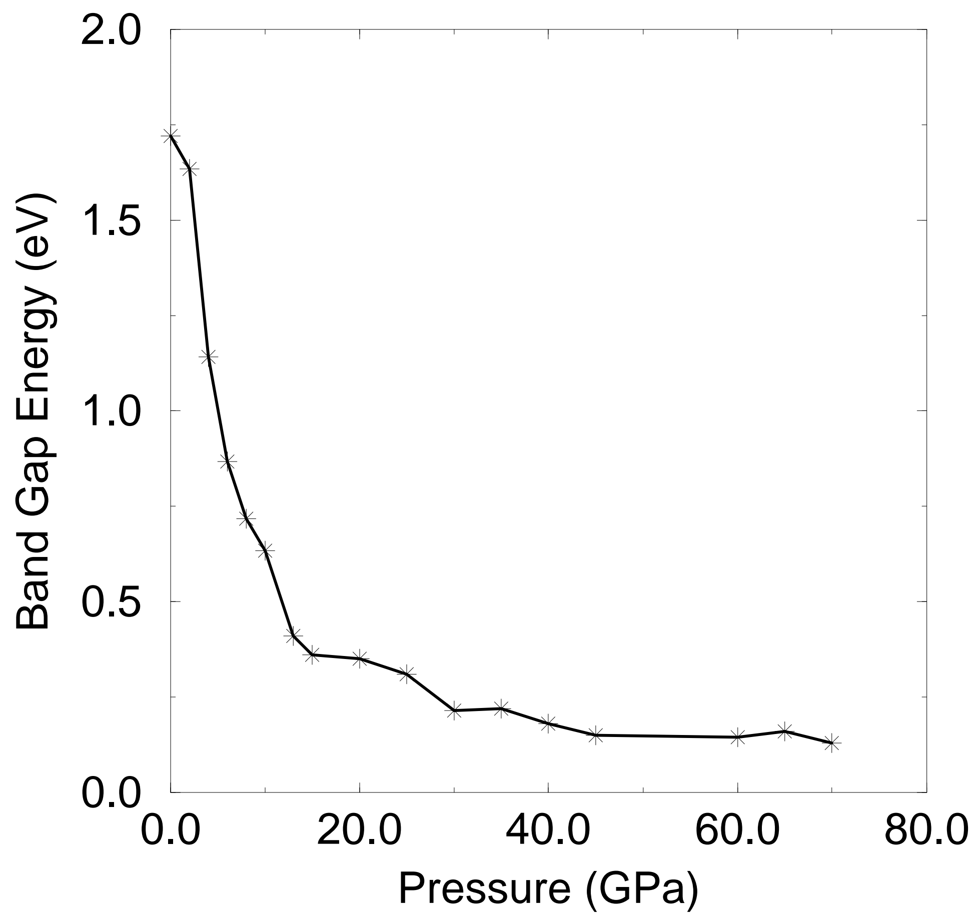

Figure 9.7: Pressure dependence of the optical gap.

is for a state, the more localized the state is. At zero-pressure, the top of the valence band is associated with three-fold Ge atoms, two-fold Se atoms forming Se dimers and one-fold Se atoms, whereas the conduction band edge is associated with three-fold Se atoms to a large extent. The pressure-induced delocalization is due to the increasing number of overlapping orbitals, yielding a broadening of bands and a decrease of the gap. The localized states in the valence band at 20 GPa arise from three-fold and four-fold coordinated Se atoms involved with at least two homopolar bonds. The result confirms our previous report [109] that Se-Se wrong bonds cause more localized states than the geometrically more defective structures. As the pressure increases, Se-related states become fully extended while a few states associated with Ge atoms at the top of the conduction band are still localized (40 GPa). They are due to five-fold and six-fold coordinated Ge atoms with wrong bonds. At 65 GPa, all localized states are completely delocalized.

9.5 Vibrational Density of States

It is useful to predict the phonon modes for LDA $GeSe_2$ and HDA $GeSe_2$. The physical origin of the phase transition can be understood by examining the pressure sensitive soft phonon modes. The vibrational density of states (VDOS) is given in Figure 9.9. The bands shift to higher frequencies with pressure without softening modes as reported in the Raman spectra of β-$GeSe_2$ [33]. The same behavior reported in t theoretical [46] and experimental [182, 183] studies of SiO_2. On the other hand, the modes of a-Si [127] show very different behaviors compared to a-$GeSe_2$; in a-Si, the optical band shifts to higher frequencies up to a critical pressure, at which point

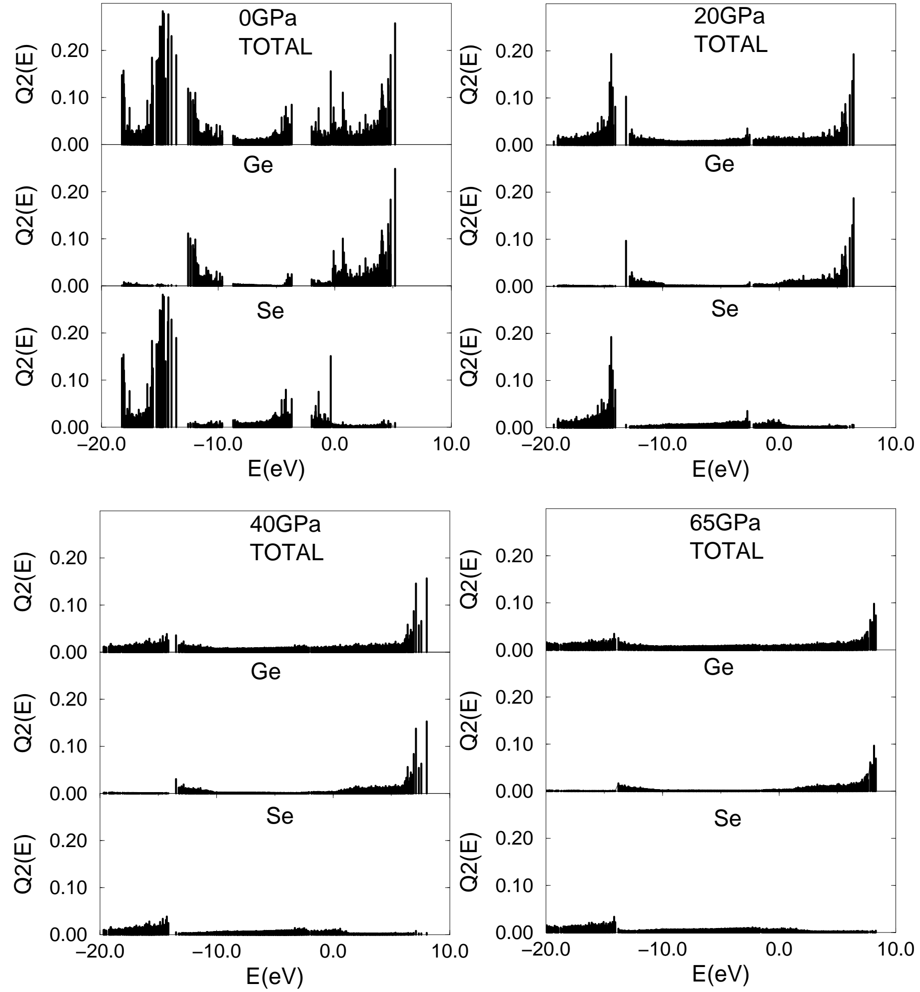

Figure 9.8: Electronic eigenstates of a-GeSe$_2$ at several pressure. The position of the vertical bar represents the eigenvalues of the electronic eigenstates, and the height of the bars is the spatial localization ($Q_2(E)$). Note the gradual delocalization of the states.

the mode frequencies decrease abruptly whereas the acoustic modes soften at high pressure.

Particular attention was devoted to vibrational modes with energies around 200 cm^{-1} with regard to the interpretation of features A_1 and A_{1c} modes. A_1 modes are in-phase breathing vibrations extended along corner-sharing $GeSe_4$ tetrahedral chain structure and A_{1c} modes are breathing like motions of Se about the edge sharing $GeSe_4$ tetrahedra [184, 185]. At low-pressure, although the intensities of A_1 and A_{1c} change, their frequencies are not shifted which is consistent with the Raman scattering study of a-$GeSe_2$ up to 2 GPa [186]. At 2 GPa, the intensity of A_1 decreases dramatically because of about 37.5% decrease of the corner sharing tetrahedra. However, the intensity of A_{1c} modes increases and broadens, although we find about 5% decrease in the concentration of clusters with edge-sharing $GeSe_4$ tetrahedra. Also, the intensity at about 180 cm^{-1} which derives from the fact that the Ge-Ge bonding increases significantly even though the number of Ge atoms involved with homopolar bond(s) decreases at 2 GPa. The results suggest a strong correlation of the modes around 200 cm^{-1}. At 4 GPa, the feature of the band around 200 cm^{-1} changes, and strong peaks at about 200 cm^{-1} and 189 cm^{-1} merge because of the structural reconstruction.

At high pressures, the intensity of the bands decrease and the bands overlap. The VDOS of the zero-pressure model from decompression at 16 GPa is slightly different from that of the initial model. In the range of 0-150 cm^{-1}, no significant change are seen except for a small shift of the frequency. Dramatic changes are seen between about 150 and 240 cm^{-1}. The increase of the intensity of the peak at 180 cm^{-1} is due

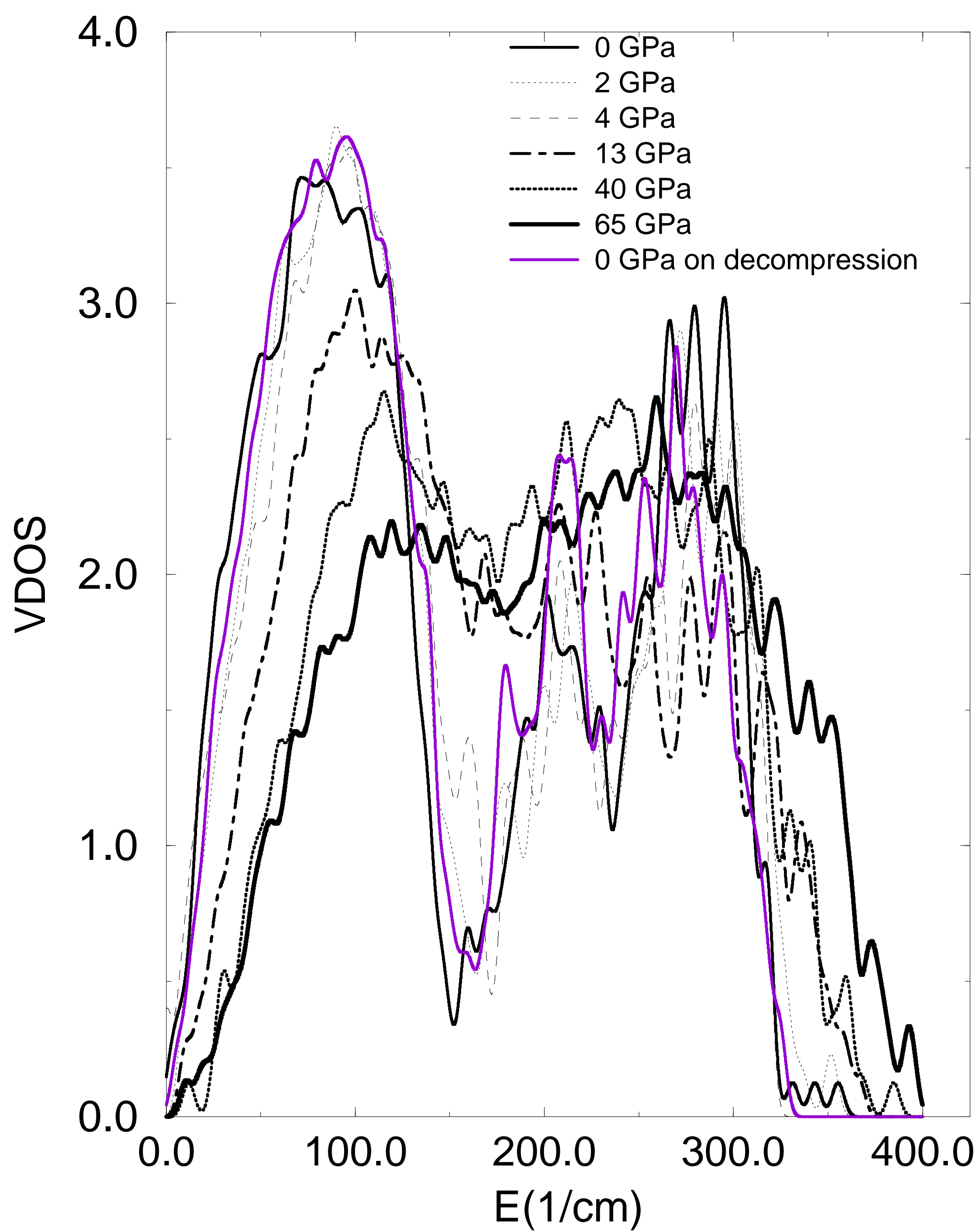

Figure 9.9: Vibrational density of states on compression and decompression from 16 GPa.

to the increase of Ge atoms with wrong bond. The peaks around 200 cm^{-1} evolve a single peak with a broad distribution. In a Raman study of $GeSe_2$ under pressure, the spectrum of the sample obtained on decompression is differ from the melt-quenched amorphous samples, and it has been shown that very broad bands in the 150-300 cm^{-1} region are well separated, and there is no low-wavenumber shoulder feature in the 150-200 cm^{-1} region which is associated with the stretching vibration of the Ge-Ge bonds [33]. The obtained spectrum from pressure release presents results similar to those of the Raman study, except for the peak at around 180 cm^{-1}, which is probably due to the finite size of the simulation cell.

A convenient measure of the degree of the localization of the vibrational modes in an amorphous solid is the inverse participation ratio,

$$IPR = N \sum_{j=1}^{N} (\mathbf{u}_n^j . \mathbf{u}_n^j)^2 \big[\sum_{j=1}^{N} (\mathbf{u}_n^j . \mathbf{u}_n^j) \big]^{-2} \tag{9.1}$$

The calculated IPR of the models is depicted in Figure 9.10. There are two types of the VDOS motion at zero pressure: (1) extended modes at frequencies less than 130 cm^{-1}, involving the motion of the entire tetrahedral units; and (2) more localized modes at frequencies higher than 130 cm^{-1} involving internal tetrahedral motion. The localized eigenmodes are extended with pressure. Similar change of the localized states has been observed in the theoretical study of SiO_2 [46].

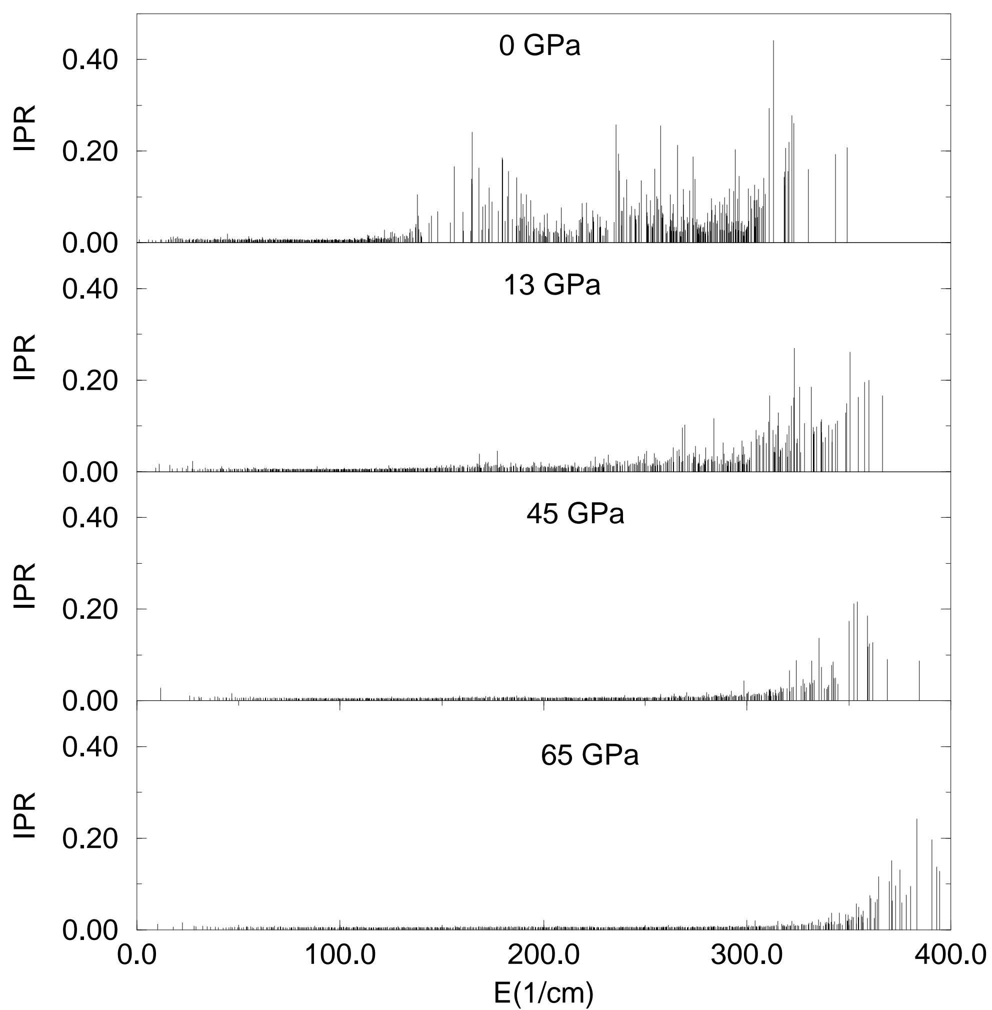

Figure 9.10: Vibrational inverse participation patio (IPR) of a-$GeSe_2$ under pressure. The highly localized modes at zero-pressure are extended with application of pressure.

9.6 Conclusions

We have studied the pressure-induced insulator-metal transition in a-$GeSe_2$ using an *ab initio* constant pressure MD technique. a-$GeSe_2$ presents a reversible continuous phase transition into a metallic amorphous phase. The gradual changes of Ge (four-fold to six-fold) and Se (two-fold to four-fold) coordinations are responsible for the amorphous to amorphous phase transition in a-$GeSe_2$. Pressure reduces the occurrence of chemical disorder, while simultaneously causing a softening of the different parts of the model and more structural disorder. We argue that chemical disorder needs to be considered a gradual transformation in addition to the topological disorder. We find an inverse correlation between the coordination of a-$GeSe_2$ and the FSDP and a reduction of the intermediate range order with an increase of pressure. Se-Se clusters at high pressure are chain-like as seen in pure Se. Under pressure both localized electronic and vibrational states are delocalized.

These calculations strongly suggest that the pressure-induced structural changes are gradual in a-$GeSe_2$. It is possible that this conclusion could depend upon the finite size of the sample and or on limited sampling of possible conformations of the glass from using only one model. We suspect that these possibilities are remote, since the admittedly small (216 atom) model studied appears to have the characteristics of the real material compared to available experiments, and also because the changes seen in a-Si are *spectacularly* different (a first-order transition is observed). It is, nevertheless, worth repeating this type of study on a larger system.

Chapter 10

Ab initio simulation of high-pressure phases of GaAs

10.1 Introduction

Numerous experimental and theoretical investigations have successfully identified high pressure phases of semiconductors. In the case of GaAs, the high pressure phases are the subject of many speculations. Recently GaAs-II has been determined to have *Cmcm* structure. However, the identity of GaAs-III remains unsolved In this study, we perform a first principles calculation to elucidate the high pressure phases of GaAs and a possible transition path between GaAs-II and GaAs-III.

An earlier x-ray diffraction study [187] has reported on several high pressure phases of GaAs at room temperature; GaAs-I (zinc blende) → GaAs-II → GaAs-III(*Imm2*) → GaAs-IV (simple hexagonal) at about 17, 24 and 60-80 GPa respectively. The study assigned GaAs-II as an orthorhombic (*Pmm2*) structure. Motivated by experiment Zhang and Cohen [188] performed a first principles calculation

and found that this structure is thermodynamically favored over the rocksalt structure. However, a recent experiment using the angle-dispersive technique [189] has reported that the structure of GaAs-II is *Cmcm*, which is observed in ZnTe [190] and InSb [191]. In addition, the experiment has shown that there is no phase transition to GaAs-III above 24 GPa. Mujica and Needs [192] performed a first principles calculation and found that *Cmcm* structure is more stable than *Pmm2* for GaAs.

In contrast to Si and Ge, the GaAs-II phase transforms back to zinc blende (ZB) structure upon decompression. McMahon and Nelmes [194] observed a new hexagonal phase, four-fold coordinated *Cinnabar*, between *Cmcm* and ZB phase on the pressure release. They also reported that *Cinnabar* phase persists with applied pressure before transforming to *Cmcm* at about 15 GPa and on further pressure release it transforms to ZB phase near 4 GPa. However there is no evidence of a transformation from ZB to *Cinnabar* on pressure increase at room temperature. First principles calculation [195, 196] have found that *Cinnabar* phase is thermodynamically unstable.

First principles calculations using thermodynamic criterion of equal free energies have successfully explained pressure-induced phase transitions. However, the methods can be only applied to known structures. In principle, first principles dynamical simulations are preferable, which may provide detailed information about transition paths and electronic structure of phases for each applied pressure. Unfortunately the predicted transition pressures are commonly larger than experimental and theoretical (from the free energy calculations) values. The large value of the metastable transition pressure from the dynamical simulations can be attributed to an intrinsic

activation barrier, and hence the simulation cell is super-pressurized in analogy to isobaric superheating in simulations [59, 60].

In this chapter, we perform a partial study of the GaAs phase diagram by simulating the response of GaAs to pressure. In our calculation, we 1) directly simulate pressure-induced phase transitions by dynamical simulation from Parrinello-Rahman method [48], and 2) use the structure of Gibbs free energy at zero-temperature ($G = E_{tot} + PV$) to accurately estimate transition pressures which are overestimated in the dynamical simulations (Parrinello-Rahman method) because of kinetics. Potentially significant features of the transitions are neglected here, including entropic contributions from lattice vibrations. The dynamical simulations successfully identify the high-pressure phases of GaAs with overestimated transition pressures. Nevertheless, the simulations eliminate doubts about the identity of both phases. The predicted transition pressure from the Gibbs free energy calculations is 23.5 GPa for *Cmcm* and 24 GPa for *Imm2*, which are comparable to the experimental results. The transformation from *Cmcm* to *Imm2* is associated with the sliding of some planes of *Cmcm* structure. Both high pressure phases of GaAs are semimetallic.

10.2 Methodology

The simulation reported here is carried out in a 216-atom model GaAs which is initially arranged in ZB structure at initial lattice parameter $a_\circ = 5.658$ Å. We use a local orbital quantum molecular dynamic method [52]. The essential approximations are (1) nonlocal, norm-conserving pseudopotentials, (2) slightly excited

local-orbitals basis set of four orbitals per site, and (3) the Harris functional implementation of density functional theory in the local density approximation. This method has been successfully applied to predict expanded volume phases of GaAs [197], and pressure-induced phase transition in crystalline silicon (a diamond to simple hexagonal), in amorphous silicon (first order amorphous to amorphous)[127], and a continuous amorphous to amorphous phase transformation in $GeSe_2$[128]. For each pressure, slow dynamical quenching starting at 1400 K is performed to fully relax the ZB structure to zero-temperature. For dynamical approach, pressure is applied via the method of Parrinello and Rahman [48], which enables the simulation cell to change volume and shape. The number of steps was selected to ensure that the system was completely relaxed (according to the criterion that the maximum force was smaller than 0.01 eV/Å). All the calculations used solely the Γ point to sample the Brillouin zone, which is reasonable for a cell with 216 atoms. A fictitious cell mass of 15×10^3 amu was found to be sui for these simulations.

10.3 Results and Discussion

10.3.1 Parrinello-Rahman simulation

In order to understand the mechanism of the semiconductor to metal transition, we first plot the pressure dependence of the relative volume from the dynamical approach in Figure 10.1. The volume changes smoothly up to 39 GPa. At this pressure, an abrupt decline of the volume is seen. In the pressure range 39-54 GPa, the volume decreases gradually and at 54 GPa another small change of the volume relative to

the first one is obtained. Up to 65 GPa no sharp modification of volume is seen.

In tetrahedrally bonded materials, initial compression causes a reduction of bond lengths and change of bond angles. The structural properties of GaAs under pressure are given in Table 10.1. The average bond length and bond angle decrease smoothly up to 39 GPa. At this pressure, a slight increase of the average bond length is seen while the average bond angle and especially the width of the bond angle distribution changes significantly without modification of coordination indicating that a transition to a distorted structure takes place (Figure 10.3). This result is consistent with the experiment [193] which has reported that GaAs presents "crystalline disorder" before it transforms into GaAs-II. At ambient temperature, the phase transition in GaAs tends to be sluggish and diffraction patterns of the high pressure phases characterized by broad peaks indicative of strain and disorder [49]. In the pressure range 39-54 GPa, the average bond angle and the width of the bond angle distribution exhibit a significant modification, implying more distorted phases. The structures in the pressure range 39-54 GPa do not have partial six-fold coordination as reported in the experiment[193], which is probably due to the use of a perfect crystalline structure with periodic boundary conditions. In a perfect crystal, the compression is uniformly distributed and nucleation centers for phase transitions do not exist, which may hinder a partial coordination change and favor a global coordination modification. When defects are introduced a transition nucleates at defects, which is seen in the previous study of amorphous materials under pressure, and in simulation of the solid to liquid phase transition of silicon [198].

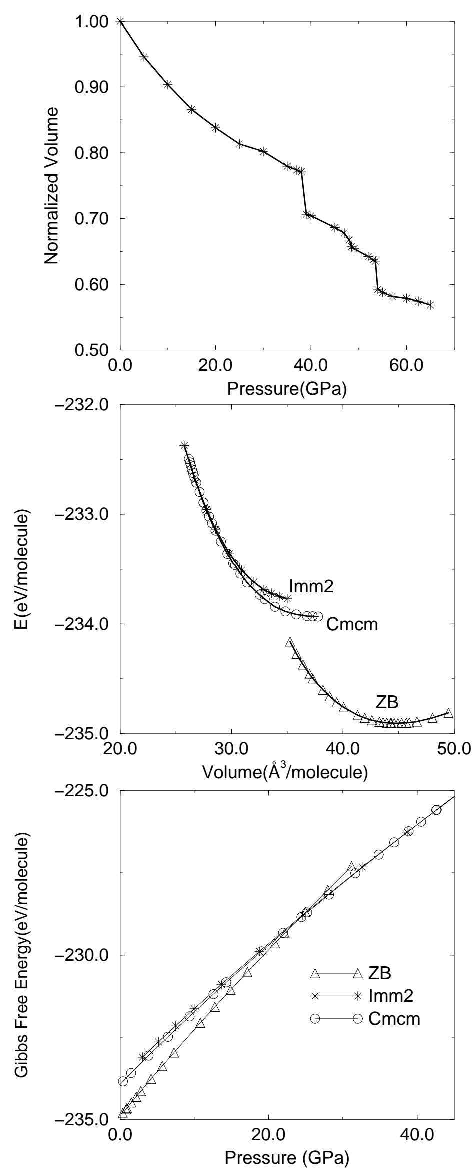

Figure 10.1: (a) The normalized volume to the zero-pressure measured volume.(b) The energy E in eV per molecule versus the volume per molecule for ZB and the *Cmcm* and *Imm2* phase.(c) The Gibbs free energy of ZB and *Cmcm* and *Imm2* structures.

Table 10.1: Structural properties of GaAs under pressure; average bond length (ABL), average bond angle (ABA), width of bond angle distribution (WBAD), and average coordination number (ACN).

Pressure (GPa)	35	39	53.5	54	57
ABL (Å)	2.241	2.265	2.273	2.41	2.405
ABA(degree)	109.40	106.76	104.415	103.995	104.84
WBAD(degree)	2.58	16.06	20.964	30.74	30.65
ACN	4.0	4.0	4.0	6.0	6.0

The second abrupt change of the structural parameters is seen at 54 GPa. The average bond length increases and the coordination changes from four-fold to six-fold. All bonds are heteropolar. The bond angle distribution function of the obtained structure at 54 GPa is given Figure 10.2. The structure presents several peaks at about 70°,82°, 90°, 98°, 109.6°(close the ideal tetrahedral angle), 140°,162° and 177°. The structure at 54 GPa is depicted in Figure 10.3. The structure is a zigzag stacking of slightly distorted NaCl-like planes. The phase is only compatible with *Cmcm* structure of GaAs which can be related to NaCl-phase by shearing of alternate (010) planes and a puckering of [100] rows. Mujica and Needs [192] have reported that the NaCl phase is unstable to such shearing of (010) planes, which is the driving force leading to a *Cmcm* structure, while puckering and cell shape distortions are consequences of the shearing. *Cmcm* is a usual structure seen in II-VI and III-V semiconductors[189]. We find $b/a \sim 0.983$ and $c/a \sim 1.046$, which are in good

agreement with the the experimental values of $b/a = 0.973$ and $c/a = 1.055$[187], and the theoretical results of $b/a = 0.953$ and $c/a = 1.049$ [192]. The transition volume of the *Cmcm* in the constant pressure relaxation simulation is 26.5 Å^3 per molecule volume. However, it is found to be 30.447 Å^3 in the thermodynamic criterion of the Gibbs free energy calculation (see below), which is in a good agreement with an accurate self-consistent calculation result of 31.538 Å^3 per molecule volume of *Cmcm* phase [192].

A gradual phase change to an orthorhombic structure for GaAs-III occurs at 57 GPa (Figure 10.3). The structure, of space group *Imm2*, consists of a body centered orthorhombic lattice with a basis (0,0,0) and (0,1/2,Δ). This transition is in excellent agreement with the earlier experiment [187]. This structure, however, has not been seen in the recent experiment [189] and hence there are some doubts about the identity of the GaAs-III phase. The present study suggests that there is a transition to *Imm2* phase.

The lattice parameters obtained for *Imm2* are $a = 4.63\text{Å}$, $b = 4.55\text{Å}$ and $c = 2.435\text{Å}$, which are less than the experimental value of $a = 4.92\text{Å}$, $b = 4.79\text{Å}$ and $c = 2.635\text{Å}$. The important parameter of *Imm2* is Δ, which ranges between 0.25 and 0.5. When $\Delta = 0.25$ and $b/a = 1$ the symmetry increased and *Imm2* phase becomes β-Sn structure, and when $\Delta = 0.5$ the structure becomes *Immm*. In the case of $\Delta = 0.5$ and $b/c = \sqrt{3}$, *Imm2* turns to simple hexagonal structure. We find that $\Delta \sim 0.325$, which is slightly less than the experimental result of $\Delta = 0.425$ but lies on the range $0.25 < \Delta < 0.5$.

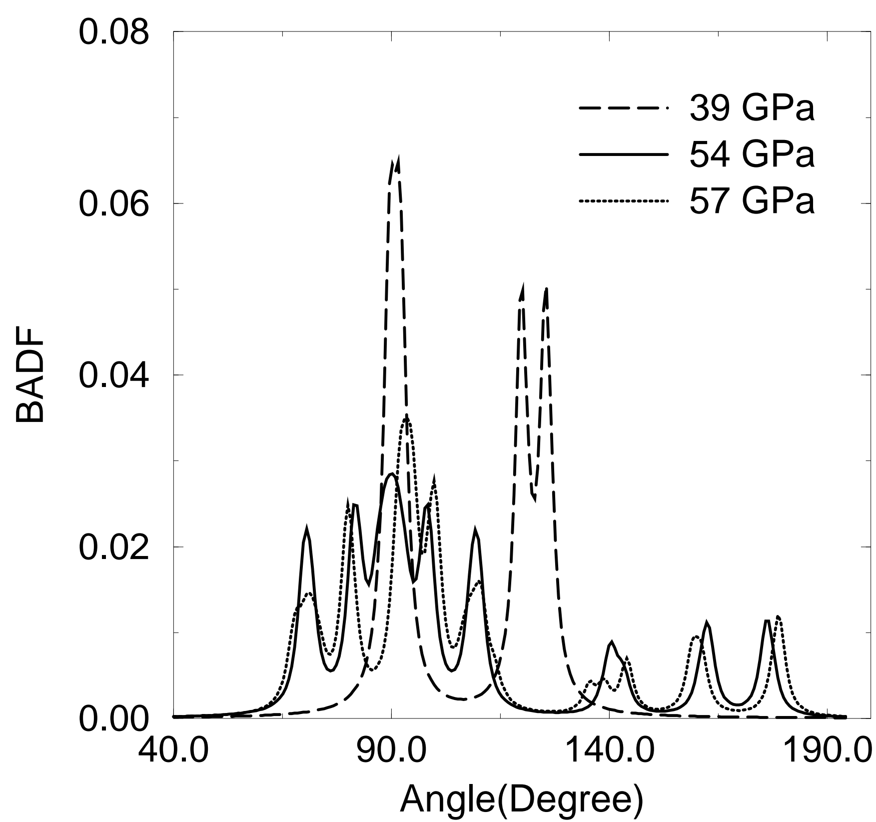

Figure 10.2: The bond angle distribution function (BADF) is calculated using a Gaussian representation and the width of broadening is $\sim 2^{\circ}$.

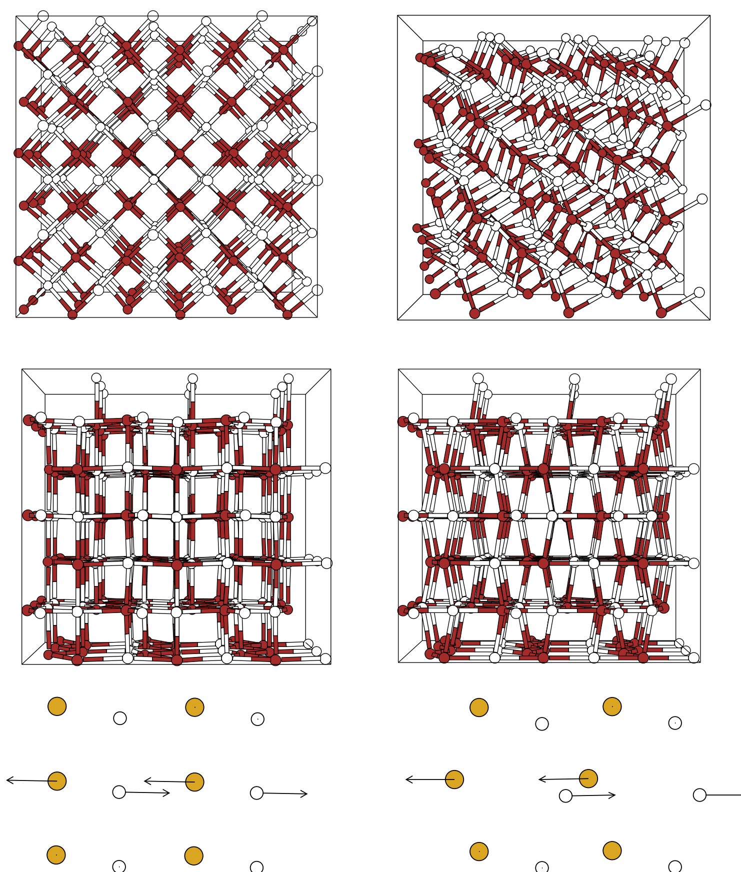

Figure 10.3: The upper-left panel is ZB at 0 GPa, the upper-right panel is distorted structure at 39 GPa, the middle-left panel is *Cmcm* structure at 54 GPa and the middle-right panel is *Imm2* at 57 GPa. In the upper and middle panels, the dark atoms are Ga and white ones are As. The lower-left panel is *Cmcm* and the right one is *Imm2* and in these panels Ga and As is not identified. The lower-panels are correspond to the simple picture of transition path.

In order to elucidate the transition path, a simple picture is depicted in Figure 10.3. The dark atoms belong to the first (001) plane and white ones to the second (001) plane in the lower-panels of the figure. For clarity we do not identify Ga and As atoms, and the shift of the atoms is exaggerated. The atoms with arrow on the second (010) plane are most active in the transformation from *Cmcm* to *Imm2* and the arrows indicate the direction of displacement. The atoms on the second (010) and the first (001) planes move to $[\bar{1}00]$ direction whereas those on the second (010) and (001) planes move to [100] direction. This opposite displacement leads to a transformation from *Cmcm* to *Imm2*. With this transition path, it can be seen that a large displacement of the active atoms yields a transition to simple hexagonal structure. This picture also supports gradual transitions of *Cmcm* $\rightarrow$ *Imm2* $\rightarrow$ simple hexagonal.

10.3.2 Phase transitions from Gibbs free energy

The ZB, *Cmcm* and *Imm2* structures are optimized at several volumes using a constant volume simulation. The total energy per molecule versus the volume is shown in Figure 10.1. The energies at minimized structures are fit to the third order Birch-Murnaghan equation of state [116];

$$E(V) = E_\circ + \frac{9}{8}KV_\circ[(V_\circ/V)^{2/3} - 1]^2\left\{1 + \left(\frac{4-K'}{2}\right)\left[1 - \left(\frac{V_\circ}{V}\right)^{2/3}\right]\right\}. \quad (10.1)$$

The equilibrium volume $V_\circ$, the bulk modules at zero temperature and pressure, K and its pressure derivative K' for the ZB phase are given in Table 10.2. The calculated parameters for the ZB structure are in excellent agreement with the experimental

Table 10.2: Structural parameters at zero temperature for ZB. Equilibrium volume per molecule $V_\circ$, bulk modules K, and pressure derivative of bulk modules K'.

K(GPa)	K'	$V_\circ$ (Å^3 per molecule)
74.19[a]	4.6[a]	44.812[a]
74.0[b]	4.6[b]	44.135[b]
75.0[c]	4.49[c]	45.168[d]

and theoretical studies.

In the constant volume simulation, we find that Δ parameter of *Imm2* phases reaches the lower limit 0.25 (the smallest value for which *Imm2* is defined) near 3 GPa and hence below this pressure *Imm2* phase becomes unstable and transforms to a *Cmcm* structure.

As found in the previous study of silicon [127] and other simulations [59, 60], the predicted transition pressure from Parrinello-Rahman simulations is much higher than experimental values. In order to obtain an equilibrium critical pressure, we calculate the Gibbs free energy ($G = E_{tot} + PV$) at zero-temperature for ZB and *Cmcm* and *Imm2* structures. The Gibbs free energy curve of ZB and *Cmcm* phases (Figure 10.1) crosses at about 23.5 GPa, indicating a first order phase transition. Although the critical pressure is higher than the starting pressure of 17 GPa, it is close to the value of 22-23.4 GPa at which the transformation is completed. The transition from ZB to *Imm2* occurs at 24 GPa, which is in excellent agreement with the experimental result of 24 GPa. The free energy of *Cmcm* phase is lower than

that of *Imm2* up to 30 GPa, indicating that *Cmcm* phase is more stable than *Imm2*. In the pressure range 30-55 GPa, the Gibbs free energy of both structures becomes equal and it is not well defined which structure is more stable. This is compatible with a continuous phase change between these structures.

It is also argued that the GaAs-II phase is a semiconductor or semimetal [187]. The electron density of states (EDOS) of the high pressure phases is depicted in Figure 10.4. We find that both high pressure phases of GaAs are semimetals.

The vibrational density of states (VDOS) is depicted in Figure 10.5. The optical and acoustic bands are broadened and their intensity decreases dramatically. The acoustic modes are softened while the optical modes shift into higher frequencies. The VDOS of *Cmcm* phase can be separated into three bands; below 120 cm^{-1}, in the range of 120-240 cm^{-1} and above 240 cm^{-1}. For *Imm2* phase, these bands are well separated with a shift to high frequencies.

10.4 Conclusions

We have studied the pressure induced phase transition in GaAs with an *ab initio* constant pressure relaxation. GaAs exhibits a first order phase transition to *Cmcm* structure at 54 GPa. With the increase of pressure a continuous phase change to *Imm2* occurs at 57 GPa. The method identifies both high pressure phases of GaAs with large value of metastable transition pressures. Nevertheless, the simulations provide detailed information about the pressure-induced phase transitions in GaAs. On the other hand, at the present thermodynamic criterion of the Gibbs free energies is required to estimate accurate transition pressures.

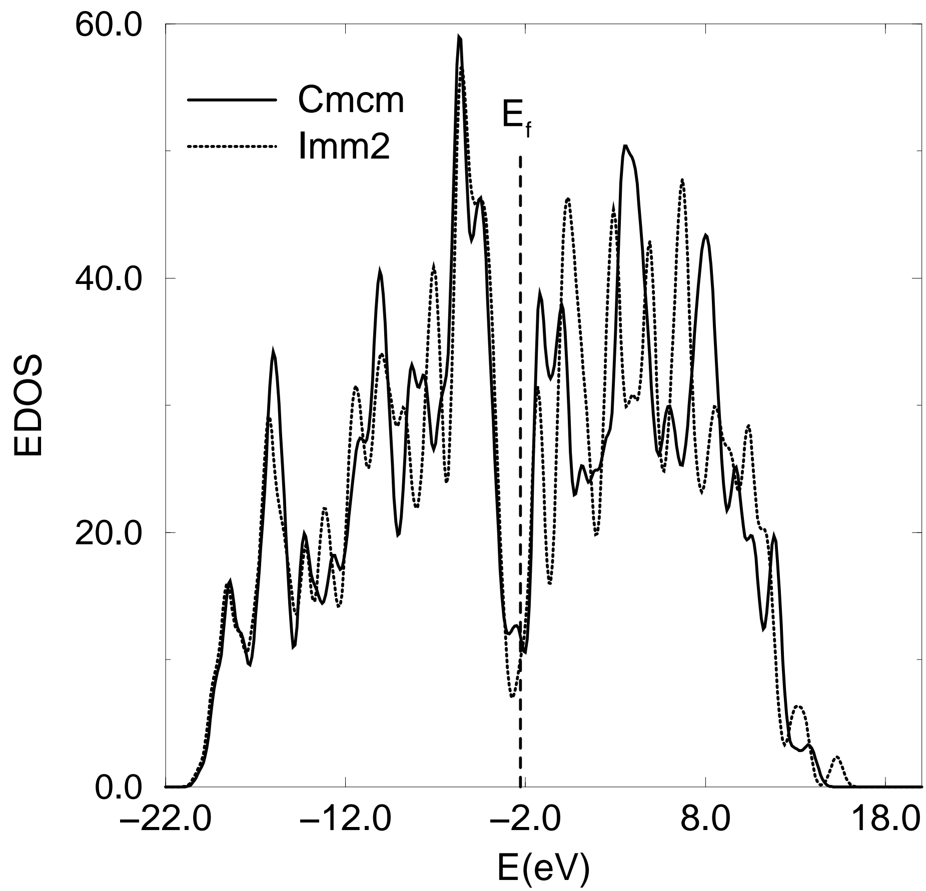

Figure 10.4: Electronic density of states (EDOS) of *Cmcm* at 54 GPa, and *Imm2* at 57 GPa.

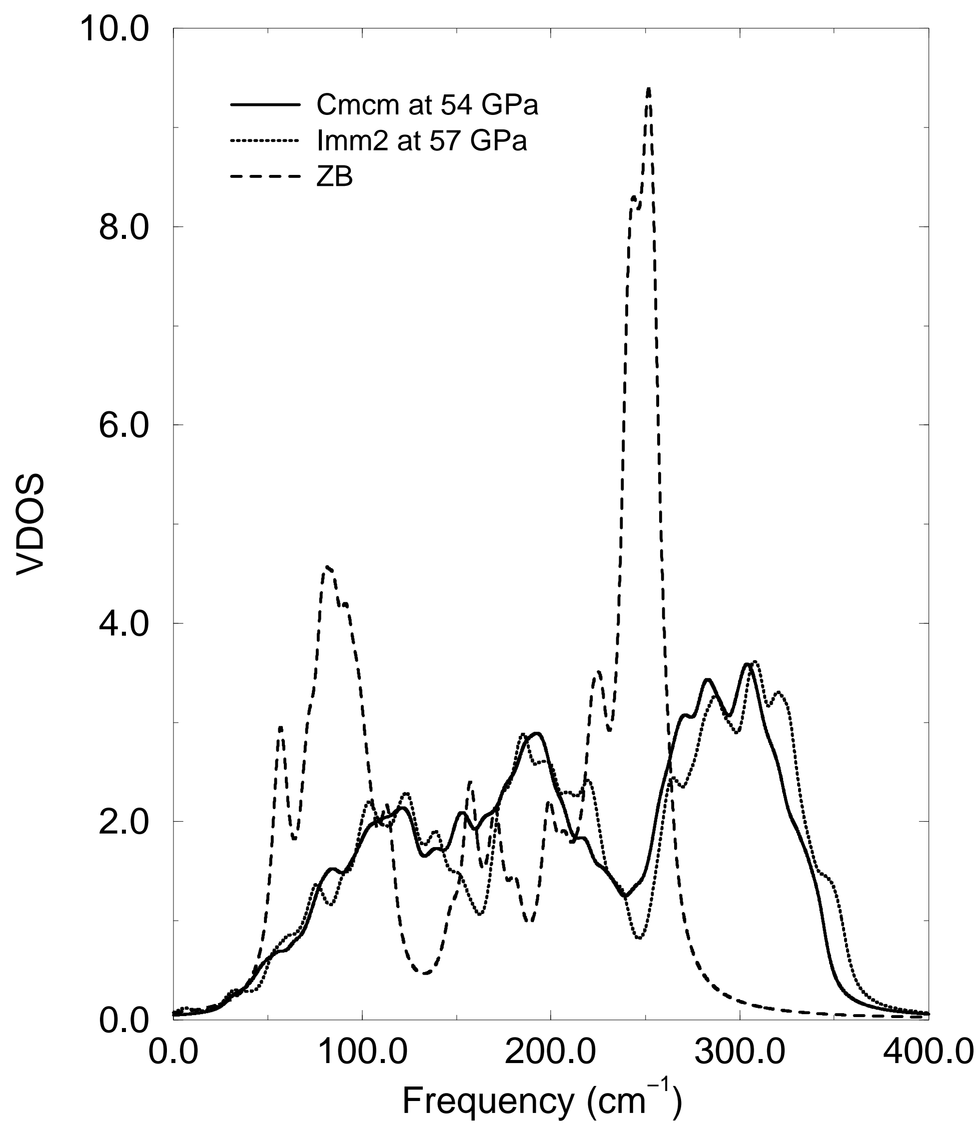

Figure 10.5: VDOS of ZB structure at zero-pressure, *Cmcm* at 54 GPa, and *Imm2* at 57 GPa.

Chapter 11

Concluding Remarks and Further Considerations

11.1 Summary

In this work, we have studied pressure-induced phase transitions in certain amorphous and crystalline semiconductors using constant volume and pressure *ab initio* simulations. We find that a-Si and a-Ge undergo a first order amorphous to amorphous phase transition, which is remarkably similar to that seen for H_2O [1, 2] and SiO_2 (near glass transition temperature) [7, 8]. This suggests an underlying transition between a high density and a low density liquid phase in supercooled Si and Ge. On the pressure release, the amorphous networks do not transform back to their original structures and the networks are found to be about 20% denser that the initial structures, indicating an irreversible phase transition in a-Si and a-Ge. The high density amorphous phase of a-Si and a-Ge is similar to their metallic liquid phase, which is confirmed in a later study [61].

A paracrystalline silicon model (amorphous silicon with a crystalline grain) transforms to a high density amorphous phase, which is very similar to that found for *a*-Si. The crystalline portion of the network appears to transform to a high density amorphous phase upon compression. Such a pressure-induced amorphization of diamond silicon was seen in porous silicon [11]. The transformation of the crystalline grain begins at the boundary and proceeds into the core.

In order to study crystallization of *a*-Si the model, we compute the volume dependence of Gibbs free energy. Diamond, β-Sn, and *a*-Si are optimized for several volumes and fit to the Birch-Murnaghan equation of state [116]. An amorphous to β-Sn phase transformation is predicted at a low pressure. Such a crystallization of *a*-Si is not seen in the present dynamical simulations and in a later investigations [61]. We argue that the amorphous to high density crystalline phase transition is kinetically hindered at low temperatures and needs more thermal activation because the transformation requires bond breaking (considering ring formation) and large displacement of some atoms in contrast to diamond to β-Sn transition.

Another remarkable transition obtained from the Gibbs free energy calculation is a pressure-induced high density amorphization of diamond structure. Recently the occurrence of pressure-induced amorphization of diamond silicon has observed during metastable compression at room temperature.

In stark contrast to *a*-Si, *a*-Ge and paracrystalline silicon, the amorphous to amorphous phase transition proceeds gradually in *a*-$GeSe_2$ and the transition is reversible. Such a continuous transition is expected since the experimental studies reported that most binary amorphous compounds undergo a gradual metallization

[10] while their crystalline state exhibits a first order transition. The physical origin of the gradual phase transformation in amorphous compounds is not clear. One may argue that the gradual transition is a result of topological disorder. However, this cannot be primarily due to topological disorder since a-Si and a-Ge structure are geometrically disordered. Bonding in binary amorphous networks is inhomogenous because of the existence of chemical disorder: for example in a-$GeSe_2$, Ge-Ge, Se-Se and dominate Ge-Se bonding (cluster) exist, and hence a-$GeSe_2$ have three distinct domains with a different stability limit. The importance of the chemical disorder is determined to large extent by ionicity. To our knowledge, the effects of chemical disorder on pressure-induced phase transition have not been studied or considered. The present study suggests that chemical disorder plays a very important role in amorphous compounds. Since the formation of wrong bond(s) is unfavorable energetically, the application of pressure causes a suppression of the occurrence of chemical disorder, and simultaneously it results in a decomposition of the different parts of the model. Therefore, we argue that not only structural disorder but chemical disorder needs to be considered for a gradual transformation.

The optical gap of a-Si, a-Ge and paracrystalline silicon increases initially, reaches a maximum and then decreases with the application of pressure while that of their crystalline states decreases smoothly. In either amorphous or crystalline phase, nevertheless, we find that the insulator-metal transition occurs with a sharp drop in the optical gap. In a-$GeSe_2$, the optical gap decreases with increasing pressure because of the dramatic structural change in the network. The localization of the gap states tend to decrease gradually and to promote metallic conduction at high pressures.

Pressure yields dramatic changes in vibrational spectra of amorphous networks. It is found that the behavior of low-energy frequency modes is quite different; low frequency modes of a-Si and a-Ge soften because of a negative Grünesien parameter in low-energy part (means that these modes soften with a decrease of volume), whereas those of a-$GeSe_2$ shift into high frequencies without mode softening as seen in SiO_2 [46]. The results in a-$GeSe_2$ and SiO_2 [46] suggest that amorphous to amorphous phase transitions do not arise primarily from the phonon softening[45]. We also find that the localized vibrational states become extended with increasing pressure in the amorphous networks.

We have investigated crystal to crystal phase transitions in Si, Ge and GaAs and calculated some physical properties of their high pressure phases. The dynamical simulations successfully identify the high pressure phase of GaAs and clear some doubts about the existence of *Cmcm* and *Imm2*.

11.2 Further Considerations

Understanding of pressure induced phase transitions in disordered materials, especially in amorphous semiconductors, is far from complete. In order to determine the transition mechanism and structural, electronic and vibrational properties for each applied pressure, computer simulations are desirable because of difficulties probing thin films and small samples. Our simulation technique appears to be reliable and can be employed with other amorphous and crystalline materials. Before considering other systems, several investigations, however, can be performed to further explain the pressure-induced phase transitions in these materials:

Simulations can be employed to investigate pressure-induced phase transitions at different temperatures, and a pressure-temperature phase diagram of these amorphous materials can be determined, which would provide a full picture of polyamorphism and high density crystallization.

There is direct evidence of liquid to liquid phase transition in a few materials, and the existence of this transition has been investigated for others. Liquid Si and Ge appear to be a candidate to investigate this phenomenon. Liquid $GeSe_2$ was studied under pressure, and no sign of a first order liquid-liquid phase transition is observed but the structure of liquid phase change from two dimension to three dimension. This three dimensional structure can be studied and compared to high density amorphous phase of $GeSe_2$ glass.

Pressure-induced amorphization in Si, Ge and GaAs on decompression is a well-known phenomenon, and the nature of this transition is unclear. An investigation on pressure-induced amorphization in these systems gives insight the physical origin of the transition.

Si and Ge have a various number of high pressure phases. The transition paths between phases, their mechanical, optical, chemical, and vibrational properties can be determined.

Bibliography

[1] O. Mishima, L.D. Calvert, and W. Whalley, Nature (London) **314**, 76 (1985).

[2] O. Mishima, J. Chem. Phys. **100**, 5910 (1994).

[3] P. H. Poole, F. Sciortino, U. Essmann and H. E. Stanley, Nature (London) **360** 324 (1992).

[4] P. H. Poole, U. Essmann, F. Sciortino, and H. E. Stanley, Phys. Rev. E **48**,4605 (1993).

[5] C. Meade, R. J. Hemley and H. K. Mao, Phys. Rev. Lett. **69**, 1387 (1992).

[6] O. B. Tsiok, V. V. Brazhkin, A. G. Lyapin, and L. G. Khvostantsev, Phys. Rev. Lett. **80**, 999 (1998).

[7] D. J. Lacks, Phys. Rev. Lett. **84**, 4629 (2000); Phys. Rev. Lett. **80**, 5385 (1998).

[8] G. D. Mukherjee, S. N. Vaidya, and V. Sugandhi, Phys. Rev. Lett. **87**, 195501 (2001).

[9] O. Shimomura, S. Minomura, N. Sakai, K. Asaumi, K. Tamura, J. Fukushima and H. Endo, Phil. Mag. **29**, 547 (1974).

[10] S. Minomura, *High pressure and Low-Temperature Physics* (Plenum, New York, 1978) p.483.

[11] S. K. Deb, M. Wilding, M. Somayazulu, and P. F. McMillan, Nature (London) **414**, 528 (2001).

[12] N. V. C. Shekar, and K. G. Rajan, Bull. Mater. Sci. **24**, 1 (2001).

[13] S. C. Gupta, and R. Chidambaram, High Press. Res. **12**, 51 (1994).

[14] I. V. Berman *et al.*, Fiz. Nizk. Temper. **16** 1227 (1990) [Sov. Low-Tem. Phys. **16** 10(1990)].

[15] R. J. Hemley, L. C. Chen, and H. K. Mao, Nature (London) **338**, 638 (1989).

[16] C. H. Polsky, L. M. Matrinez, K. Leinenweber, M. A. VerHelst, C. A. Angell and G. H. Wolf, Phys. Rev. B **61**, 5934 (2000).

[17] K. Tanaka, Phys. Rev. B **43**,4302(1991).

[18] K. Tanaka, J. Non-Crystalline Solids **150**, 44 (1992).

[19] V. Domnich, and Y. Gogotsi, Rev. of Advan. Mat. Science **3**, 1-36 (2002); V. Domnich, Y. Gogotsi, and M. Trenary, Mat. Res. Soc. Symp. **649**, 2001.

[20] V. V. Brazhkin, A. G. Lyapin, L.G. Khvostantsev, V. A. Sidorov, O. B. Tsiok, S. C. Bayliss, V. Sapelkin and S. M. Clark, Phys. Rev. B **54**,1808 (1996).

[21] M. Shimada and F. Dachille, Inorg. Chem. **16**, 2094 (1977).

[22] P. Poole, T. Grande, C. A. Angell, and McMillan, Science **275**,322 (1996).

[23] Y. Katayama, Nature (London) **403**, 170 (2000).

[24] V. V. Brazhkin, S. V. Popova, R. N. Volishin, High Press. Res. **15**, 267 (1997).

[25] S. Aasland and P.F. McMillan, Nature (London) **369**, 633 (1994).

[26] P. H. Poole, M. Hemmati, and C. A. Angell Phys. Rev. Lett. **79**, 2281 (1997).

[27] P. H. Poole, U. Essmann, F. Sciortino, and H. E. Stanley, Phys. Rev. B **48**, 4605 (1993).

[28] R. J. Hemley, and H. K. Mao, Phys. Rev. Lett. **57**, 747 (1992).

[29] D. J. Durben and G. H. Wolf, Phys. Rev. B **43**,2355 (1991).

[30] P. W. Anderson, Phys. Rev. **109**, 1492 (1958).

[31] J. Dong and D.A. Drabold, Phys. Rev. Lett. **80**, 1928 (1998).

[32] R. J. Hemley, A. P. Jephcoat, H. K. Mao, L. C. Min, and M. H. Manghnani Nature (London) **334**, 52 (1988).

[33] A. Grezechnik, T. Grande and S. Stølen, J. Solid State Chem. **141**, 248 (1998).

[34] R. G. Green, H. Luo, and A. L. Raoff, Phys. Rev. Lett. **73**, 2676 (1994).

[35] M. Tang, and S. Yip, Phys. Rev. Lett. **75**, 2738 (1995).

[36] D. D. Klud, J. S. Tse, and E. Whalley, J. Chem. Phys. **90**,2390 (1989).

[37] V. V. Brazhkin, A. G. Lyapin, S. V. Popova, and R. N. Voloshin, JETP Lett. **56**, 152 (1992); Phys. Rev. B **51**,7549 (1995).

[38] A. G. Lyapin and V. V. Brazhkin, Phys. Rev. B **54**,12036 (1996).

[39] S. Rastogi, M. Newman, and A. Keller, Nature (London) **353**, 55 (1991).

[40] E. Whalley, D. D. Klud, and Y. P. Handa, Nature (London) **342**, 782 (1989).

[41] Y. P. Handa, J. S. Tse, D. D. Klud, and E. Whalley, J. Chem. Phys. **94**,623 (1991).

[42] J. S. Tse, and D. D. Klud, Phys. Rev. Lett. **67**, 35597 (1991).

[43] N. Binggeli and J.R. Chelikowsky, Phys. Rev. Lett. **69**,2220 (1992).

[44] D. W. Dean, R.M. Wentzcovitch, N. Keskar, J.R. Chelikowsky, and N. Binggeli, Phys. Rev. B **61**, 3303 (2000).

[45] V. V. Brazhkin, A. G. Lyapin, O. V. Stalgorova E. L. Gromnitskaya, S. V. Popova, and O. B. Tsiok, J. Non-Crystalline Solids **212**, 49 (1997).

[46] W. Jin, R. K. Kalia, P. Vashishta, and J. P. Rino, Phys. Rev. Lett. **71**, 3146 (1993).

[47] H. C. Andersen, J. Chem. Phys. **72**, 2384 (1980).

[48] M. Parrinello and A. Rahman, Phys. Rev. Lett. **45** 1196 (1980); S. Nose and M. L. Klein, Mol. Phys. **50** 1055 (1983).

[49] G. J. Ackland, Rep. Prog. Phys. **64**, 483 (2001).

[50] P. Hohenberg, and W. Kohn, Phys. Rev. B **136**,864 (1964).

[51] W. Kohn and L. J. Sham, Phys. Rev. B **140**,1133 (1965).

[52] O. F. Sankey and D. J. Niklewski, Phys. Rev. B **40**, 3979 (1989);O. F. Sankey, D. A. Drabold, and G. B. Adams, Bull. Am. Phys. Soc. **36**,924 (1991).

[53] D. M. Cerpeley, and G. J. Alder, Phys. Rev. Lett. **45**, 566 (1980)

[54] J. Perdew, and A. Zunger, Phys. Rev. B **23**, 5048 (1989).

[55] R. Hamman, M. Shlüter, and C. Chiang Phys. Rev. Lett. **43**, 51494 (1979).

[56] J. Harris, Phys. Rev. B **31**, 1770 (1985).

[57] J. Tersof, Phys. Rev. Lett. **56**, 632 (1986); Phys. Rev. B **37**, 16991 (1988); Phys. Rev. B **38**, 9902 (1988).

[58] M. Z. Bazant, E. Kaxiras and J. F. Justo, Phys. Rev. B **56**, 8542 (1997).

[59] K. Mizushima, S. Yip and E. Kaxiras, Phys. Rev. B **50** 14952 (1994).

[60] I. H. Lee, J. W. Jeong and K.J. Chang Phys. Rev. B **55** 5689 (1997).

[61] P. C. Kelires, unpublished, CECAM Workshop on Rigidity and Strain Fields in Crystalline and Amorphous materials, June 25-27, 2001 (Lyon, France).

[62] S. Nakhmanson, PhD thesis, Ohio University, 2001.

[63] J. P. Rino, A. Chatterjee, I. Ebbsjö, R. K. Kalia, A. Nakano, F. Shimojo, and P. Vashishta, Phys. Rev. B **65**, 195206 (2002).

[64] S. Kodiyalam *et al.* Phys. Rev. Lett. **86**, 55 (2001).

[65] R. Car, and M. Parrinello, Phys. Rev. Lett. **22**, 2471 (1985).

[66] P. Focher, G. L. Chiarotti, M. Bernasconi, E. Tosatti and M. Parrinello, Europhys. Lett. **26** 345 (1994).

[67] M. Bernasconi, G. L. Chiarotti P. Focher, S. Scandolo, E. Tosatti, and M. Parrinello J. Phys. Chem. Solids **56**, 501 (1995).

[68] S. Scandolo, M. Bernasconi, G. L. Chiarotti, P. Focher and E. Tosatti Phys. Rev. Lett. **74**, 4015 (1995).

[69] R. Mantanak, C. Molteni and M. Parrinello Phys. Rev. Lett. **84**, 682 (2000).

[70] R. Rousseau, M. Boero, M. Bernasconi M. Parrinello, and K. Terakura, Phys. Rev. Lett. **85**, 1254 (2000).

[71] W. H. Zachariasen, J. Am Chem. Soc. **54**,3841 (1932).

[72] D. E. Polk, J. Non-Crystalline Solids **5**, 365(1971).

[73] F.Wooten, K. Winer, and D. Weaire Phys. Rev. Lett. **54**, 1392 (1985).

[74] N. Mosseau, T. Barkema Phys. Rev. B **62**, 4985 (2000).

[75] G. T. Barkema, and N. Mousseau, Phys. Rev. Lett. **77**, 4358 (1996).

[76] M. Cobb and D. A. Drabold, Phys. Rev. B **56** 3054 (1997).

[77] J. Li and D. A. Drabold, Phys. Rev. Lett. **85**, 2785 (2000).

[78] P. A. Fedders, D. A. Drabold, and S. Nakhmanson, Phys. Rev. B **58**, 15624 (1998).

[79] D. A. Drabold and P. A. Fedders, Phys. Rev. B **60**, R712 (1999).

[80] D. A. Drabold, J. Non. Cryst. Solid **266**, 211 (2000).

[81] P. N. Keating, Phys. Rev. **145**, 637 (1966).

[82] G. T. Barkema and N. Mousseau, Phys. Rev. Lett. **77**, 4358 (1996); R. L. C. Vink, G. T. Barkema, W. F. van der Weg and N. Mousseau to be published J. Non. Cryst. Solid.

[83] K. Laaziri, S. Kycia, S. Roorda, M. Chicoine, J. L. Robertson, J. Wang, and S. C. Moss, Phys. Rev. B **60**, Nov.15(1999).

[84] A. A. Demkov, J. Ortega, O. F. Sankey and M. P. Grumbach, Phys. Rev. B **52**, 1618(1995).

[85] P. Stumm and D. A. Drabold, Phys. Rev. Lett. **79**,677 (1997).

[86] D. A. Drabold, P. A. Fedders, and P. Stumm Phys. Rev. B **49**, 16415 (1994).

[87] A. Szabo and N. S. Ostlund, *Modern Quantum Chemistry*(Dover, New York, 1996).

[88] N. Bernstein, M. J. Aziz and E. Kaxiras , Phys. Rev. B **58**, 4579 (1998).

[89] E. P. Donovan, F. Spaepen, D. Turnbull, J. M. Poate, and D. C. Jacobson J. Appl. Phys. **57**, 2782 (1985).

[90] D. A. Drabold, P. A. Fedders, S. Klemm, and O. F. Sankey, Phys. Rev. Lett.**67**, 2179 (1991).

[91] L. Ley, J. Reichardt and R. L. Johnson Phys. Rev. Lett.**49**, 1664 (1982).

[92] S. K. Bose, K. Winer, and O. K. Andersen, Phys. Rev. B **37**, 6262 (1988).

[93] D. K. Biegelsen and M. Stutzmann, Phys. Rev. B **33**, 3006 (1986).

[94] Spatial character of the local-to-extended transition in mSW1. For a given eigenstates, the electron charge density depicted according to the four level gray scale. Each atom shown according to the fraction of total charge: very dark ($\geq$ 10%), less dark ($\geq$ 5%), light ($\geq$ 1%), white ($\leq$ 1%) such that at least 35% of the total charge is shown. The upper left panel is a localized (midgap) state with $E = -3.226$ eV, $Q_2(E) = 0.05105N$. The upper right and lower left panel are less extended valence states with $E = -3.588$ eV, $Q_2(E) = 0.0057N$, $E = -3.785$ eV, $Q_2(E) = 0.0027N$ respectively. The lower right panel is an extended valence state with $E = -4.196$ eV, $Q_2(E) = 0.0018N$

[95] M. C. Gupta and A. L. Ruoff, J. App. Phys. **51**, 1072 (1980).

[96] H. Olijnyk, S. K. Sikka, and W. B. Holzapfel, Phys. Lett. **103A**, 137 (1987).

[97] J. Z. Hu, L. D. Merkle, C. S. Menoni and I. L. Spain, Phys. Rev. B **34**, 4679 (1986); J. Z. Hu and I. L. Spain, Solid State Comm. **51**,263 (1984).

[98] M. I. McMahon and R. J. Nelmes, Phys. Rev. B **47**, 8337 (1993); M. I. McMahon R. J. Nelmes and N. G. Wright and D. R. Allan, Phys. Rev. B **50**, 739 (1994)

[99] M. T. Yin and M. L. Cohen, Phys. Rev. Lett. **45** 1004 (1980).

[100] K. J. Chang and M. L. Cohen, Phys. Rev. B **31** 7819 (985).

[101] T. Morishita and S. Nosé, Prog. Theo. Phys. Supp. **138** 251 (2000).

[102] G. Ramachadran, P.F. McMillan, S.K Deb, M. Somayazulu, J. Gryko, Jianjun Dong and O. T. Sankey J. Phs. Conden. Matter. **12**, 4013 (2000).

[103] Jianjun Dong, O. T. Sankey and G. Kern, Phys. Rev. B **60**, 950 (1999).

[104] B. R. Djordjevic, M.F. Thorpe, and F. Wooten, Phys. Rev. B **52**, 5685 (1995).

[105] A. A. Demkov, W. Windl, and O. F. Sankey, Phys. Rev. B **53** 11288 (1996).

[106] J. Song, S. E. Ulloa and D.A. Drabold Phys. Rev. B **53** 8042 (1996).

[107] M. Yu, S. E. Ulloa and D.A. Drabold Phys. Rev. B **61** 2620 (2000).

[108] M. Durandurdu, D.A. Drabold and, N. Mousseau, Phys. Rev. B **62**,15307 (2000).

[109] X. Zhang and D.A. Drabold, Phys. Rev. B **62**,15695 (2000).

[110] S. Duclos, Y. Vohra, and A. Ruoff, Phys. Rev. B **41** 12021 (1990).

[111] F. Zandiehnadem and W. Y. Ching, Phys. Rev. B **41** 12162 (1990).

[112] P. McMillan, B. Piriou, and R. Couty, J. Chem.Phys. **81** 4234 (1984).

[113] I. Stich, R. Car and M. Parrinello, Phys. Rev. Lett. **63** 2240 (1989), Phys. Rev. B **44** 4262 (1991).

[114] G. Fabricius, E. Artacho, D. Sanchez-Portal, P. Ordejon, D. A. Drabold and J. M. Soler, Phys. Rev. B **60** R16283 (1999).

[115] Y. Waseda and K. Suzuki, Z. Phys. B **20** 339 (1975).

[116] F. Birch, J. Geophys. Res.**57** 227 (1952).

[117] V. V. Brazhkin, A. G. Lyapin, V. A. Goncharova, O.V. Stal'gorova and S. V. Popova Phys. Rev. B **56** 990 (1997).

[118] G. A. Connell and W. Paul, J. Non. Cryst. Solids **8-10**, 215 (1972).

[119] T. Tanaka, J. Non. Cryst. Solids **90** , 363 (1987).

[120] T. Tanaka and S. Nitta, Phys. Rev. B **39** 3258 (1989).

[121] S. Minomura J. Phys. (Paris) Colloq. **42** C4-181 (1981); in *Semiconductors and Semimetals*, edited by J. I. Pankove (Academic, Orlando, 1984), Vol.21A,p.273.

[122] B. Weinstein and G. J. Piermarini, Phys. Rev. B **12** 1172 (1975).

[123] P.M. Chaikin and T.C. Lubensky, *Principles of Condensed Matter Physics* (Cambridge University Press, New York, 1995)

[124] J. L. Yarger, C. A. Angell, S. S. Borick, and G. H. Wolf, Ch. in *Supercooled Liquids: Advances and Novel Applications*, Editors: J. Fourkas, D. Kivelson, U. Mohanty, and K. Nelson; (ACS Symposium Series 676; ACS, Washington, D.C. 1997).

[125] H. Schober, M. Koza, A. Tolle, F. Fujara, C. A. Angell and R. Bohmer, Physica B **241-243**, 897-902 (1998).

[126] S. H. Tolbert, A. B. Herhold, L. E. Brus, and A. P. Alivisatos, Phys. Rev. Lett. **76**, 4384 (1996).

[127] M. Durandurdu, and D. A. Drabold, Phys. Rev. B **64**, 14101 (2000).

[128] M. Durandurdu, and D.A. Drabold, Phys. Rev. B **65**, 104208 (2002).

[129] M. T. Yin, and M. L. Cohen, Phys. Rev. B **26**, 5668 (1982).

[130] S. Lannin, L. J. Pilione, S. T. Kshirsagar, R. Messier, and R. C. Ross, Phys. Rev. B **26**, 3505 (1982).

[131] N. Maley, and J. S. Lannin, Phys. Rev. B **36**, 1146 (1987).

[132] N. Maley, D. Beeman, and J. S. Lannin, Phys. Rev. B **38**, 10611 (1988).

[133] X. Liu, B. E. White, R. O. Pohl, E. Iwanizcko, K. M. Jones, A. H. Mahan, B. N. Nelson, R. S. Crandall, and S. Veprek, Phys. Rev. Lett. **78**, 4418 (1997).

[134] X. Liu, and R. O. Pohl, Phys. Rev. B **58**, 9067 (1998).

[135] D. Beeman, R. Tsu, and M. F. Torpe, Phys. Rev. B **32**, 874 (1985).

[136] R. Biswas, A. A. M. Bouchard, W. A. Katmitakara, G. S. Grest, and C. M. Shoukolis Phys. Rev. Lett. **60**, 2280 (1988).

[137] S. Nakhmanson, and D. A. Drabold, Phys. Rev. B **58**, 15325 (1998).

[138] S. Nakhmanson, and D. A. Drabold, Phys. Rev. B **61**, 5376 (2000).

[139] J. L. Feldman, P. B. Allen, and S. R. Birkham, Phys. Rev. B **59**, 3551 (1999).

[140] M. Marinov, and N. Zotov, Phys. Rev. B **55**, 2938 (1997).

[141] F. Finkemeier and W. von Niessen, Phys. Rev. B **58**, 4473 (1998).

[142] S. D. Bembenek, and B. B. Laird, Phys. Rev. Lett. **74**, 936 (1995).

[143] J. Fabian, and P. B. Allen, Phys. Rev. Lett. **79**, 1885 (1997).

[144] S. N. Taraskin, and S. R. Elliot Phys. Rev. B **56**, 8605 (1997).

[145] B. B. Laird, and S. D. Bembenek, J. Phys. Conden. Matter **8**, 9569 (1996).

[146] M. Hanfland, U. Schwarz, K. Syassen and K. Takemura, Phys. Rev. Lett. 82 (1999) 1197.

[147] S. Kasper and M. S. Richards, Acta Crstalloggr. **17** 752 (1964).

[148] Y. X. Zhao, F. Buehler, J. R. Sites and I. L. Spain, Solid State Com. **59** 679 (1986).

[149] J. Zeman, M. Zigone, G. L. J. A. Rikken, and G. Martinez, J. Phys. Chem. Solids **56**, 655 (1995).

[150] M. M. J. Treacy and J. M. Gibson, Acta Crystallogr. **A52**, 212 (1996)

[151] M. M. J. Treacy, J. M. Gibson, and P. J. Keblinski, J. Non-Cryst. Sol. **231**, 99 (1998).

[152] M. M. J. Treacy, P. M. Voyles, and J. M. Gibson, J. Non-Cryst. Sol. **266**, 150 (2000).

[153] S. M. Nakhmanson, P. M. Voyles, N. Mousseau, G. T. Barkema and D. A. Drabold, Phys. Rev. B **63**, 235207 (2001).

[154] M. Durandurdu, and D. A. Drabold, Phys. Rev. B**66**, 041201 (2002).

[155] M. Durandurdu, and D. A. Drabold, Phys. Rev. B **65** 104208 (2002).

[156] J. Freund, R. Ingalls, and E. E. Crozier, J. Phys. Chem. **94**, 1087 (1990).

[157] H. S. Chen, and D. Turnbull, J. Appl. Physics **40**, 4214 (1969).

[158] P. Germain, K. Zellama, S. Squelard, J. C. Bourgoin, and A. Gheorghiu, J. Appl. Physics **50**, 6986 (1979).

[159] C. Jamieson, Science **139**, 762 (1963); **139**, 845 (1963).

[160] H. J. McSkimin, J. Appl. Phys. **24**, 988 (1953); H. J. McSkimin and P. Andreatch, Jr., *ibid.* **34**, 651 (1963); **35**, 2161 (1964).

[161] N. Moll, M. Bockstedle, M. Fuchs, E. Pehlke, and M. Scheffler, Phys. Rev. B **52**, 2550 (1995).

[162] Y. Waseda, *The Structure of Non-Crystalline Material, Liquids, and Amorphous Solids* (McGraw-Hill, New York, 1980).

[163] R. V. Kulkarni, W. G. Aulbur, and D. Stroud, Phys. Rev. B **55**, 6896 (1997).

[164] See, for example, P. Boolchand, in *Insulating and Semiconducting Glasses*, edited by P. Boolchand (World Scientific, Singapore,2000), p.191.

[165] C. T. Prewitt and H. S. Young, Science **149**, 535 (1965).

[166] T. Grande, M. Ishii, M. Akaisi, S. Aasland, H. Fjellvag, and S. Stølen, J. Solid State Chem. **145**, 167 (1999).

[167] Z. V. Popovic, Z. Jaksic, Y. S. Raptis and E. Anastassakis, Phys. Rev. B **57** 3418(1998); Z. V. Popovic, M. Holtz, R. Reimann and K. Syassen, Phys. Status Solidi **198**, 533 (1996).

[168] M. V. N. Prasad, A. Asokan, G. Parthasarathy, S. S. K. Titus and E. S. R. Gropal, Phys. Chem. Glasses **34**, 199 (1993).

[169] I. Petri, P. S. Salmon and H. E. Fischer, Phys. Rev. Lett. **84**, 2413 (2000).

[170] M. Cobb and D. A. Drabold, Phys. Rev. B **56**, 3054 (1997).

[171] M. Durandurdu and D. A. Drabold, unpublished.

[172] H. Sugiura, K. I. Kondo and A. Sawaoka, in *High-Pressure Research in Geophysics*, edited by Akimoto and M. H. Manghnani (Reidel, Dordrecht, 1982),p 551; M. Grimsditch, Phys. Rev. Lett. **52**, 2379(1984).

[173] K. Miyauchi, J. Qiu, M. Shojiya, Y. Kawamoto and N. Kitamura, J. Non-Crys. Solids **279**, 186 (2001).

[174] N. Sakai and H. Fritzsche, Phys. Rev. B **15**, 973 (1977).

[175] S. Susman K. J. Volin, D. L. Price, M. Grimsditch , J. P. Rhino, R. K. Kalia, P. Vashishta, G. Gwanmesia, Y. Wang and R. C. Liebermann, Phys. Rev. B **43**, 1194 (1991).

[176] S. R. Elliott, Phys. Rev. Lett. **67**, 711 (1991).

[177] I. Petri, P. S. Salmon and W. S. Howells, J. Phys. Condens. Matter **11**, 10219 (1999).

[178] E. T. Jaynes, Phys. Rev. **106**, 620 (1957).

[179] K. Tanaka, Phys. Rev. B **42**, 11245 (1990).

[180] V. A. Sidorov, V. V. Brazhkin, L.G. Khvostantsev, A.G. Lyapin, A. V. Sapelkin and O. B. Tsiok, Phys. Rev. Lett. **73**, 3262(1994).

[181] M. Kastner, Phys. Rev. B **7**, 5237 (1973).

[182] P. McMillan, B. Piriou and R. Couty, J. Chem. Phys. **81**, 4234 (1984).

[183] R. J. Hemley, H. K. Mao, P. M. Bell and B. O. Mysen, Phys. Rev. Lett. **57**, 747 (1986).

[184] R. Cappelletti, M. Cobb and D. A. Drabold, Phys. Rev. B **52**, 9133 (1995).

[185] S. Sugai, Phys. Rev. B **35**, 1345 (1987).

[186] Z. V. Popovic, M. Holtz, R. Reimann and K. Syassen, Phys. Status Solidi **198**, 337 (1996).

[187] S. T. Weir, Y. K. Vohra, C. A. Vanderborg, and A. L. Ruoff, Phys. Rev. B **39**, 1280 (1989).

[188] S. B. Zhang, and M. L. Cohen, Phys. Rev. B **39**, 1450 (1989).

[189] M. I. McMahon, and R. J. Nelmes, Phys. Status Solidi (b) **198**, 389 (1996).

[190] R. J. Nelmes, M. I. McMahon, N. G. Wright, and D. R. Allan, Phys. Rev. Lett. **73**, 1805 (1994).

[191] R. J. Nelmes, and M. I. McMahon, Phys. Rev. Lett. **74**, 106 (1995).

[192] A. Mujica, and R. J. Needs, J. Phys. Condens. Matter **8**, L237 (1996).

[193] J. M. Besson, J. P. Itié, A. Polian, G. Weill, J. L. Mansot, and J. Gonzalez, Phys. Rev. B **44**, 4214 (1991).

[194] M. I. McMahon, and R. J. Nelmes, Phys. Rev. Lett. **78** 3697 (1997).

[195] A. A. Kelsey, G. J. Ackland, and S. J. Clark, Phys. Rev. B **57**, R2029 (1998).

[196] A. Mujica, A. Muñoz, and R. J. Needs, Phys. Rev. B **57**, 1344 (1998).

[197] A. A. Demkov, O. F. Sankey, J. Gryko, and P. F. McMillan Phys. Rev. B **55**, 6904 (1997).

[198] S. R. Phillpot, J. F. Lutsko, D. Wolf, and S. Yip, Phys. Rev. B, **40**, 2831 (1989); J. F. Lutsko, D. Wolf, S. R. Phillpot, and S. Yip, *ibid.* **40**, 2841 (1989); S. R. Phillpot, S. Yip, and D. Wolf, Comput. Phys. **3**, 20 (1989).

[199] H. J. McSkirmin, A. Jayaraman, and P. Andreatch, Jr., J. Appl. Phys. **38**, 2362 (1967).

[200] *Elastic, Piezoelectric, Piezooptic, and Electrooptic Constant of Crystals,* edited by O. Madelung, Landolt- Börnstein, New Series, Group III, Vol.1 (Springer-Verlag, Berlin, 1966).

Appendix: Publication list

1. M. Durandurdu, D. A. Drabold and N. Mousseau, Approximate ab initio calculations of electronic structure of amorphous Si, Phys. Rev. B **62** 15307 (2000) [chapter 3].

2. M. Durandurdu and D. A. Drabold, Ab initio simulations of first order amorphous to amorphous phase transition of Silicon, Phys. Rev. B **64** 014101 (2001) [chapter 4].

3. D. Farkas, M. Durandurdu, W. A. Curtin and C. Ribbens, Multiple-dislocation emission from the crack tip in the ductile fracture of Al, Philosophical Magazine A **81** 1241 (2001).

4. M. Durandurdu and D. A. Drabold, Simulation of pressure-induced polyamorphism in a chalcogenide glass $GeSe_2$, Phys. Rev. B **65** 104208 (2002) [chapter 9].

5. M. Durandurdu and D. A. Drabold, Ab initio simulation of high pressure phases of GaAs, Phys. Rev. B **66** 045209 (2002) [chapter 10].

6. M. Durandurdu and D. A. Drabold, First order pressure-induced polyamorphism in germanium, Phys. Rev. B, **66** 041201 (2002) [chapter 8].

7. M. Durandurdu and D. A. Drabold, Ab initio simulation of pressure-induced low-energy excitations in amorphous silicon, Phys. Rev. B (Accepted) [chapter 6].

8. M. Durandurdu and D. A. Drabold, A theoretical investigation of amorphization and crystallization in silicon phases, J. Non. Cryst. Sol. submitted [chapter 5].

9. M. Durandurdu and D. A. Drabold, Pressure-induced structural phase transition in paracrystalline silicon, Phys. Rev. B (Accepted) [chapter 7].